

Acquisitions and Bibliographic Services Branch

395 Wellington Street Ottawa, Ontario K1A 0N4 Bibliothèque nationale du Canada

Direction des acquisitions et des services bibliographiques

395, rue Wellington Oltawa (Ontario) K1A 0N4

Your life Votre référence

Our Ma. Notre référence

NOTICE

The quality of this microform is heavily dependent upon the quality of the original thesis submitted for microfilming. Every effort has been made to ensure the highest quality of reproduction possible.

La qualité de cette microforme dépend grandement de la qualité de la thèse soumise au microfilmage. Nous avons tout fait pour assurer une qualité supérieure de reproduction.

AVIS

If pages are missing, contact the university which granted the degree.

S'il manque des pages, veuillez communiquer avec l'université qui a conféré le grade.

Some pages may have indistinct print especially if the original pages were typed with a poor typewriter ribbon or if the university sent us an inferior photocopy. La qualité d'impression de certaines pages peut laisser à désirer, surtout si les pages originales ont été dactylographiées à l'aide d'un ruban usé ou si l'université nous a fait parvenir une photocopie de qualité inférieure.

Reproduction in full or in part of this microform is governed by the Canadian Copyright Act, R.S.C. 1970, c. C-30, and subsequent amendments.

La reproduction, même partielle, de cette microforme est soumise à la Loi canadienne sur le droit d'auteur, SRC 1970, c. C-30, et ses amendements subséquents.



Enhancement of Volume Coverage and Temporal Resolution for Functional Magnetic Resonance Brain Imaging

by

Richard D. Hoge, B.Sc.

Medical Physics Unit

McGill University

Montreal, Quebec, Canada

A thesis submitted to the Faculty of Graduate

Studies and Research in partial fulfilment of the
requirements of the degree of

Master of Science in Medical Physics.

© Richard D. Hoge, November, 1995



Acquisitions and Bibliographic Services Branch

395 Wellington Street Ottawa, Ontario K1A 0N4 Bibliothèque nationale du Canada

Direction des acquisitions et des services bibliographiques

395, rue Wellington Ottawa (Ontario) K1A 0N4

Your file Votre référence

Our file Notre référence

The author has granted an irrevocable non-exclusive licence allowing the National Library of Canada to reproduce, loan, distribute or sell copies of his/her thesis by any means and in any form or format, making this thesis available to interested persons.

L'auteur a accordé une licence irrévocable et non exclusive permettant à la **Bibliothèque** nationale du Canada reproduire, prêter, distribuer ou vendre des copies de sa thèse de quelque manière et sous quelque forme que ce soit pour mettre des exemplaires de cette thèse à disposition des la personnes intéressées.

The author retains ownership of the copyright in his/her thesis. Neither the thesis nor substantial extracts from it may be printed or otherwise reproduced without his/her permission. L'auteur conserve la propriété du droit d'auteur qui protège sa thèse. Ni la thèse ni des extraits substantiels de celle-ci ne doivent être imprimés ou autrement reproduits sans son autorisation.

ISBN 0-612-12204-2



Abstract

This thesis presents two techniques for enhancing the volume coverage and temporal resolution of functional magnetic resonance brain imaging on conventional clinical scanners, namely, echo-shifting and retrospective temporal resolution selection (RTRS). The techniques are compared with conventional 2D gradient echo imaging on the bases of speed and sensitivity to functional changes, and the necessary theory is reviewed to develop physical models explaining the different properties observed.

Acquisition, reconstruction, and analysis software packages for functional brain mapping are presented and demonstrated with visual stimulation. The echo-shifted sequence permitted acquisition of 3D maps of brain activity which could be better correlated with local anatomy than 2D maps, and the RTRS method provided physiological response curves with greatly increased temporal resolution.

Résumé

Cette thèse décrit deux méthodes rapide d'imagerie fonctionnelle du cerveau par résonance magnétique dans deux et trois dimensions avec une systeme conventionnelle, soit, le déplacement d'écho, et la sélection rétrospective de la résolution temporelle. Les techniques sont comparées avec une séquence conventionelle à écho de gradient du point de vue de la sensibilité aux changements fonctionnels et à la rapidité d'acquisition, et une révision de la théorie nécessaire pour développer des modèls physiques pour expliquer les différences de performance entre les méthodes est presentée.

Des logiciels pour l'acquisition, la reconstruction, et l'analyse des donnés sont aussi presentés et demonstrés avec des donnés acquises durante la stimulation visuelle. Les techniques d'imagerie à haute vitesse ont permis l'acquisition d'image en 3D de l'activité cérébrale qui était impossibles à réaliser avec des méthodes conventionnels. Des enregistrements de la réponse physiologique avec une résolution temporelle élevée ont aussi été faits.

Acknowledgments

I would like to thank my supervisor, Dr. G.B. Pike, whose unfailing guidance and encouragement have made this project an enjoyable and stimulating pursuit.

My gratitude is also extended to my fellow students at the MNI and elsewhere who have helped me throughout the course of this work. I would especially like to thank Joel Ginsburg, Sean Marrett, Patrice Munger, Sridar Narayanan, Dr. Atsushi Takahashi, and Mark Wolforth for their shared knowledge and inspiration. I would also like to thank Dr. Alan Evans for his input and for providing an open and stimulating environment in the McConnell Brain Imaging Centre.

The interest of the following members of the local neuroscience community has helped this work along greatly: Dr. Curtis Baker, Dr. Robert Hess, Dr. Tomas Paus, Dr. Odile Plaisante, Dr. Chawki Benkelfat, and Dr. Jacques Bradweyn.

The individuals who kindly volunteered to be experimental subjects also deserve to be thanked. In particular, Dr. Colin Holmes, Roch Comeau, and Laura Pisani should be recognized for their patience and generosity in this regard.

For their help in administrative and logistical matters, I thank Kate Hanratty, Louise Sabaz, and Margery Knewstubb. I am also grateful to Leo Mollevanger and André D'aoust of Philips Medical Systems for their technical support. Vasco Kollokian and Jean-Francois Malouin deserve to be thanked for keeping our heavily loaded computers and disks running smoothly. Finally, I must thank Dr. Tanya Kanigan for her patience and support throughout this project.

Financial support provided by the Medical Research Council of Canada and the U.S. National Institute of Mental Health is gratefully acknowledged.

Contents

1	intro	oauctioi	n	ı
2	Hist	ory		5
3	fMR	I Conti	rast Mechanisms	11
	3.1	Introdu	action	11
	3.2	Physio	ology	12
		3.2.1	Cerebral Circulation and Metabolism	12
		3.2.2	Activation, LCBF, and Blood Oxygenation	14
	3.3	Physic	s	16
		3.3.1	The NMR Signal	16
		3.3.2	Relaxation Behaviour	21
		3.3.3	Steady State Signal Behaviour	27
	3.4	Relaxa	ation in Perfused Tissues	28
	3.5	Discus	ssion	36
4	Fun	ctional	MR Imaging	37
	4.1	Introd	uction	37

	4.2	Data Acquisition	8
		4.2.1 Selective Excitation	l
		4.2.2 Fourier Encoding	12
		4.2.3 fMRI Sequence Parameters	18
		4.2.4 Visual Activation Studies	3
		4.2.5 Noise Sources	5.5
	4.3	Postprocessing of Functional Images 6	6
		4.3.1 Image Subtraction	8
		4.3.2 Student's <i>t</i> -test	8
		4.3.3 Linear Correlation	59
		4.3.4 Rank Correlation	0
		4.3.5 Kolmogorov-Smirnov Test	70
		4.3.6 Summary of Data Analysis Issues	7 [
		4.3.7 Analysis Software	75
	4.4	Discussion	79
5	Eche	o Shifted 3D fMRI 8	31
	5.1	Introduction	31
		5.1.1 Review of Multi-Slice MRI Methods 8	32
	5.2	Methods	37
	5.3	Results)4
	5.4	Discussion)3
6	Retr	rospective Temporal Resolution Selection 10)5
	6.1	Introduction)5

	6.2	Methods	07
		6.2.1 CINE Mode Acquisition	07
		6.2.2 Retrospective Temporal Resolution Selection	08
	6.3	Results	14
	6.4	Discussion	19
7	Com	olucions and Suggestions for Eutura Desparch	22

List of Figures

3.1	Rat capillary and neuron	13
3.2	Red blood cells in capillary	14
3.3	PET blood flow/oxygen uptake study	15
3.4	Alignment of protons in a magnetic field	18
3.5	Macroscopic magnetization from spins in a magnetic field	18
3.6	Effect of a 90° RF pulse in the rotating frame	20
3.7	Dephasing in a group of nuclear dipoles	22
3.8	Relaxation rate dependence on blood oxygenation at 4.3 T	31
3.9	Capillary matrix in rat cortex	32
4.1	Components of an MRI system	39
4.2	Examples of MR images	40
4.3	Vector magnetization and image contrast	44
4.4	Spin-warp pulse sequence	47
4.5	Slice orientations for visual studies	54
4.6	Intensity fluctuation in spin-warp images	57
4.7	Spatial distribution of noise in spin-warp images	58
4.8	Macrovessel response in fMRI studies	67

4.9	Various test statistic maps	72
4.10	Interpretation of fMRI statistical test results	74
4.11	Spatial filtering on SPM	76
5.1	Echo-shifted pulse sequence	90
5.2	Modified echo-shifted sequence	92
5.3	3D ES T2* weighted images	95
5.4	Time intensity curves from 3D ES T2* weighted images	97
5.5	3D standard deviation images	98
5.6	Percentage standard deviation of 3D ES images	99
5.7	3D t -maps for visual study	101
5.8	SPMs for 3D ES visual study on anatomical images	102
5.9	Medial wall of the occipital lobe	104
6.1	CINE mode acquisition	110
6.2	Phase encode schedule for RTRS (1)	111
6.2	Phase encode schedule for RTRS (2)	112
6.4	Image from high time resolution series and t -map	115
6.5	Time-intensity plots from high time resolution image series	116
6.6	Standard deviation image from high time resolution series	117
6.7	Image intensity cupping	118
6.8	High and low resolution time intensity curves	119

Chapter 1

Introduction

Magnetic resonance imaging (MRI) is able to depict many aspects of brain structure with remarkable clarity. Based on the phenomenon of nuclear magnetic resonance (NMR), MRI provides a means of actively probing the physical state of tissues *in vivo* in a completely non-invasive fashion. The ability of NMR techniques not only to observe but to actually control magnetization in tissues provides a dimension that is absent in most other medical imaging modalities, in which the passive interactions between tissues and various forms of radiation are observed.

The flexibility of MRI has led to many new applications including the focus of this thesis, functional magnetic resonance imaging (fMRI) of the brain. fMRI is used to delineate regions of brain tissue involved in the mediation of specific tasks and the response to different stimuli, a capability which promises to be of great use in clinical diagnosis and in basic physiological research.

In practically all fMRI studies, images of the brain are acquired in rapid succession while some stimulus or activation condition is varied. Areas of the brain which exhibit signal changes that are correlated in time with the applied stimulus are then identified through statistical postprocessing. The most common approach is based on the observation that the magnetic susceptibility of blood is a function of oxygen saturation, which in turn depends on local metabolic and blood flow rates.

The influence of blood oxygenation on the NMR behaviour of perfused brain tissue permits modulation of the MR image intensity in neuronal populations that selectively respond to an experimental stimulation paradigm. This approach is completely non-invasive, so experiments can be performed repeatedly on the same subject. The statistical power of intra-subject averaging and the intrinsic spatial resolution of MRI represent significant advances in functional brain mapping.

fMRI is still in its infancy, however, and requires significant methodological development and validation. Much of this work is being carried out on systems installed at hospitals for routine clinical scanning. A significant limitation of the current (1990–1995) generation of clinical systems for fMRI is the relatively low speed at which images are acquired. The addition of echo planar imaging (EPI) capable hardware to a conventional system greatly increases its speed, but the cost of the modification is considerable. At present most MR scanners available to neuroscience research groups are not EPI capable.

The goal of this thesis is to investigate two fast MRI techniques which are suitable for functional imaging without requiring EPI capability. This work was motivated by the desire to add functional MRI to the array of brain mapping modalities available at the Montreal Neurological Institute (MNI). The MRI system currently available at this site is not EPI capable, and alternative fast imaging techniques were required to permit volumetric functional imaging and increase the time resolution with which the physiological response could be probed. Two such methods

were examined: the echo-shifting (ES) sequence introduced by Moonen *et al.*[56] and a new technique, introduced here, termed retrospective temporal resolution selection (RTRS).

The thesis consists of three main sections. The first section, Chapter 2, presents an historical review of functional brain mapping techniques. This begins with the discovery of electrical activity in the nervous system and the use of electroencephalography (EEG) to monitor brain function. The development of techniques for the spatial localization of brain activity, such as autoradiography and positron emission tomography (PET) is then described. Finally, the emergence of nuclear magnetic resonance (NMR) imaging techniques and their application in functional brain mapping are discussed.

The second section of this thesis (Chapters 3 and 4) provides a detailed description of the physiological, chemical, and physical principles underlying functional MRI techniques. A physical model of the relationship between neuronal activation and the NMR signal from brain tissues is presented in Chapter 3, followed by a discussion of the MR imaging process and noise sources in Chapter 4. A conventional 2D gradient echo sequence for performing functional imaging is described, and results obtained during visual stimulation of a healthy volunteer are presented. A brief overview of the statistical post-processing techniques used in fMRI is also given, including a description of the analysis software developed for this study.

In the final section (Chapters 5 and 6), the two fast imaging techniques are examined. An implementation of the echo-shifted sequence for acquiring 3D functional maps and the retrospective temporal resolution selection technique are presented in Chapters 5 and 6, respectively. In each chapter experimental results from visual stimulation studies performed with the technique under investigation are

compared with those obtained using the conventional 2D gradient echo (GE) sequence in the same volunteer.

The thesis concludes with an overview of the imaging and analysis tools developed, and the results of the comparison with conventional methods. The capabilities and limitations of a typical 1995 EPI system are also described and compared with those of the techniques presented here.

Original contributions made in this thesis are: 1) the implementation of an 11 second duration 3D echo-shifted fMRI acquisition and analysis of the spatial distribution of noise; 2) the proposal and implementation of a pulse sequence permitting the enhancement and retrospective selection of temporal resolution; and 3) reconstruction and statistical analysis software for data acquired using these sequences. These contributions are presented in Chapters 4 to 6.

Chapter 2

History

In the 1770's the Italian anatomist Luigi Galvani discovered the role of electricity in the nervous system when he observed that a disembodied frog's leg would twitch when suspended by copper hooks over an iron railing[39]—a response whose cause he attributed to the electrical current produced at the junction of the dissimilar metals. His reports of the phenomenon were initially met with skepticism, but his discovery laid the foundation for the study of electrical activity in the nervous system.

The earliest observations of electrical activity in the brain were made in animals, with electrodes placed directly on the brain's surface. In 1925 the concept was extended to measurements in humans by Hans Berger, a German psychiatrist. Berger was able to record brain waves using electrodes placed next to the scalp, rather than the brain. The introduction of multiple electrode arrays led to the ability to perform crude localization of the sources of the observed electrical activity. The electroencephalograph, or EEG, thus represented the first completely non-invasive method for localizing brain function. Spatial resolution, however, was extremely

poor.

In the late 1950's the first autoradiographic studies of brain function were performed[46]. These techniques permitted extremely high resolution imaging of metabolic activity in the brains of experimental animals. In such studies, rats were injected with a radioactive tracer and sacrificed. Sections of brain tissue were then placed on photographic film and, after several days, beta radiation from the tracer would expose regions of the emulsion. Photographic images depicting local cerebre¹ blood flow (LCBF) were thus obtained. This technique formed the basis for less invasive methods of radioisotope imaging in humans, such as single photon emission computed tomography (SPECT) and positron emission tomography (PET).

The development of SPECT and PET techniques was stimulated by the introduction of x-ray computed tomography (CT) by Hounsfield in the early 1970's[37]. CT permitted high resolution tomographic images of internal tissues to be generated using an external x-ray beam projected through the body at various angles. Researchers who routinely employed autoradiographic techniques realized that the principles of CT could be applied to acquire images using internal radiation sources[68]. Over the next ten years, PET techniques were developed for the measurement of a wide variety of processes, including glucose metabolism, oxygen extraction, and blood flow.

In PET a positron emitting tracer, such as ¹⁵O labeled water, is injected into an artery which carries the tracer to the brain. The distribution of radioactivity in the brain, which reflects LCBF, can then be recorded using tomographic imaging techniques. Performing this measurement prior to and then during the execution of a task permits the identification of regions that undergo blood flow changes during the activity. Since previous autoradiographic work has suggested that blood flow is

a reliable indicator of tissue metabolic rates, regions of increased flow are assumed to be activated.

This approach has been used to map a number of mental functions to specific brain regions in humans. Although the resolution is significantly better than that of EEG mapping, activation foci separated by less than a few millimeters can still not be resolved using current PET techniques. The contrast-to-noise ratio attained is limited by permissible radiation dose levels, so multiple trials of an experiment in different subjects are often necessary to achieve reliable results. This introduces additional uncertainty, as brain structure and possibly functional organization can vary considerably across individuals. Nonetheless, PET has been a powerful tool for neuroscience research.

In the early 1970's, a new imaging modality emerged which produced superb images of the body's internal structure without the use of ionizing radiation. Magnetic resonance imaging was pioneered by Paul Lauterbur at the University of Illinois[45]. The phenomenon of nuclear magnetic resonance (NMR) had been studied since the 1950's, and was already an important tool for the study of molecular structure in chemistry and physics. The clinical use of MRI for the diagnosis of structural abnormalities in tissues had assumed a role of similar importance in medicine by the late 1980's.

In recent years NMR techniques for the observation of biological function have appeared. *In vivo* spectroscopy of animals and humans has been performed, producing images of the distribution of various metabolites in brain tissues with a resolution on the order of a centimeter[3]. While spectroscopic techniques have contributed to our understanding of cerebral metabolism, the use of these methods for functional mapping is limited by their low spatial resolution and long acquisition

times. The use of MR imaging methods for the measurement of LCBF has had greater success, however.

The first experiments in which MRI techniques were used to map activation-induced changes in LCBF in humans were performed in 1991 by Belliveau *et al.* at the Massachusetts General Hospital (MGH)[10]. A bolus of the MRI contrast agent gadolinium diethylenetriaminepentaacetic acid (Gd(DTPA)) was injected into the subject and images were acquired of its subsequent uptake in the brain under baseline conditions. The process was then repeated during presentation of a visual stimulus. Regions activated during stimulation were detected due to the increased signal changes caused by the higher concentration of the blood borne contrast medium, permitting the specific identification of the subjects' primary visual cortex. Like PET, these studies required the injection of a foreign substance to generate contrast, and only a limited number of tests could be repeated on the same individual.

Just as autoradiography had led to less invasive PET techniques, a series of PET studies formed the basis for a less invasive form of fMRI when, in 1985, Peter Fox and Marcus Raichle discovered that brain activation can induce changes in blood oxygenation levels[23, 24]. In 1990, S. Ogawa *et al.* published observations of blood oxygenation level dependent (BOLD) MRI contrast in animals[59]. Within two years, Ogawa's group and the MGH group both reported the use of BOLD MRI contrast in humans[61, 43].

Both groups observed activation-induced changes in MR signal intensity using the subject's blood, rather than an exogenous compound, as the source of contrast. Changes were observed in the visual cortex during photic stimulation with flashing goggles, and also in the primary motor cortex during a hand-squeezing task.

The completely non-invasive nature of BOLD techniques led to their almost universal adoption for functional MRI. These studies could be performed many times in the same individual, increasing statistical power without the problems associated with inter-subject variability. fMRI also offered potentially higher temporal and spatial resolution than PET.

The initial excitement surrounding BOLD fMRI was tempered by uncertainty about the physiological mechanisms leading to the observed signal changes. In 1993 and 1994, many groups reported that these changes occurred primarily in large (> 0.5 mm) blood vessels rather than in cortical tissues[21, 25, 33, 42, 44]. Since a response in such blood vessels may reflect conditions at distant tissue sites, the ability of fMRI to localize cortical activation was called into question. Other studies suggested that subject motion was largely responsible for the observed signal modulations[35].

A variety of techniques for minimizing the vascular response and the effects of subject motion emerged. Higher speed echo-planar imaging (EPI) and the use of more stringent subject immobilization, such as a bite bar, were recognized as effective means of controlling motion problems. High field (2.0 – 4.0 T) systems and new pulse sequences (e.g. asymmetric spin-echo[53]) were introduced to enhance sensitivity to cortical as opposed to vascular changes. Results obtained with these specialized systems have largely laid to rest earlier concerns about the relevance of fMRI activation maps. In 1995 at the MGH, the borders of the human visual areas were precisely determined using a 1.5 T system equipped to perform EPI with asymmetric spin-echoes[70]. The correspondence between these results and the known visual organization in non-human primates, determined using more direct and invasive methods, leaves little doubt as to the potential of EPI based fMRI

techniques.

In spite of the increasing acceptance of echo-planar and asymmetric spin-echo fMRI methods, there is ongoing debate on whether reliable functional maps can be obtained on standard (1.5 T, non-EPI) clinical systems. A number of fast imaging techniques have been introduced which do not require special scanner hardware, such as interleaved spiral imaging[55] and the echo-shifting technique investigated in this report[56]. While there is no question that these methods can greatly increase temporal resolution, they are not compatible with fast asymmetric spin-echo techniques and only spiral imaging comes close to the almost complete immunity to motion and pulsatility artifacts achieved in single-shot EPI[29].

It is also not clear to what extent fMRI applications can be extended beyond the simple sensorimotor paradigms that have been studied to date. Exploiting the full potential of the technique will require continued investigation into the relationship between cerebral blood flow, metabolism, and tissue NMR behaviour. Development of non-EPI functional MR techniques will permit research sites with conventional MR scanners to contribute to this effort, as well as allowing clinical centers to apply fMRI techniques in patients using existing hardware platforms.

Chapter 3

fMRI Contrast Mechanisms

3.1 Introduction

In order for functional MR brain imaging to be possible, there must be some physiological process that reflects the metabolic rates local to different neuronal populations and can alter the intensity in an MR image. This chapter will examine the basic physiology and physics underlying fMRI contrast mechanisms.

For MR imaging the process which provides the most useful indication of regional shifts in metabolic activity is thought to be the blood oxygenation level dependent (BOLD) contrast phenomenon[51]. Cerebral blood flow (CBF) rate is another physiological parameter which changes significantly with activation, but MRI is very sensitive to flow in larger vessels which may be distant from the actual neuronal population which has been excited. It is generally accepted that acquisition techniques for fMRI should maximize BOLD contrast, while minimizing the effects of flow[8, 52, 51].

3.2 Physiology

3.2.1 Cerebral Circulation and Metabolism

In order to describe BOLD MRI contrast it is necessary to consider the role of blood in meeting the brain's metabolic demands. The brain depends on blood flow to continually replenish metabolite stores, which are very small compared to the rate at which they are consumed. This is illustrated by the fact that complete interruption of cerebral blood flow results in loss of consciousness within ten seconds in humans. The only potential metabolite which crosses the blood-brain barrier under normal conditions is the carbohydrate glucose, which may be metabolized aerobically to meet the brain's large energy demands (estimated at 20 W by Sokoloff[71]). Anaerobic metabolism of glucose is too inefficient to meet the brain's basic energy needs, so oxygen is also consumed at a high rate. In fact the brain accounts for roughly 20% of the body's basal oxygen consumption[71].

The various metabolites are transferred to brain tissues via the capillaries, which are the smallest blood vessels. The diameter of these is on the order of microns, as illustrated in the electron micrograph in Figure 3.1.

Oxygen is transported by the red blood cells. These cells consist mainly of a thin, flexible cell membrane that acts as an envelope to contain hemoglobin and other chemicals. Molecules of hemoglobin, the substance which gives arterial blood its red color, have two components: the protein globin; and heme, an iron compound. In the lungs, oxygen molecules bind loosely to the iron of the hemoglobin, forming oxyhemoglobin.

The red blood cells containing oxyhemoglobin travel through the larger blood

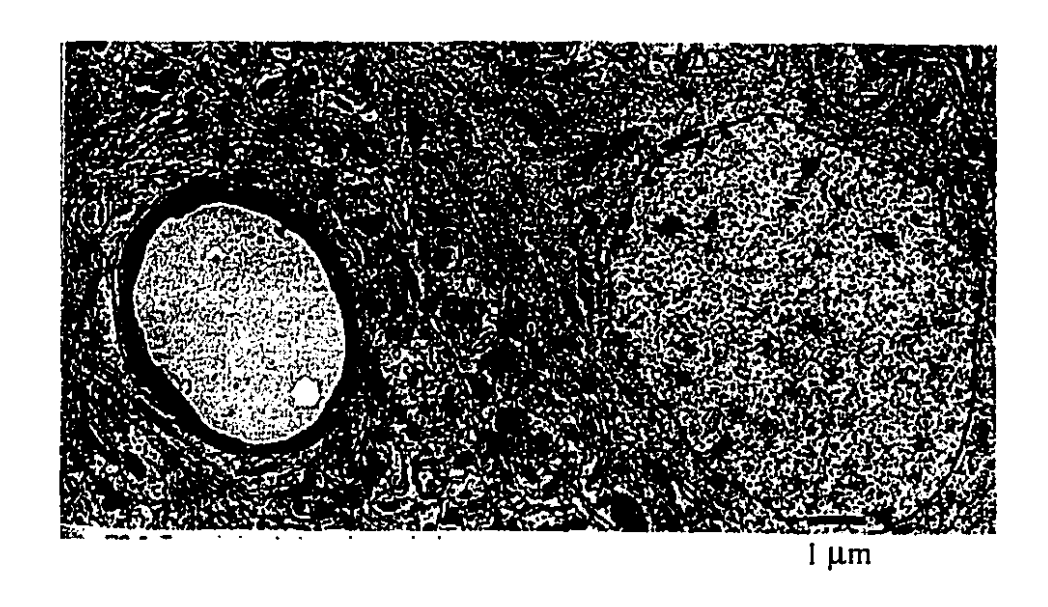


Figure 3.1: Cross section of rat capillary (left) and neuron (right) (From [79]).

vessels to reach the capillaries in the brain tissues. The oxygen then passes through the red blood cell wall, through the capillary wall, and into the tissues. Hemoglobin that has given up its oxygen is called deoxyhemoglobin. Carbon dioxide, a waste product generated by the oxidative metabolism of glucose, passes from the tissues into the red blood cells, where it combines with the globin of the hemoglobin. Figure 3.2 shows several red blood cells flowing through a typical human capillary. The diameter of a red blood cell is about 7 microns, so they pass single file through the capillary.



Figure 3.2: Human red blood cells flowing through capillary (From [76]).

3.2.2 Activation, LCBF, and Blood Oxygenation

It is widely accepted that cerebral blood flow is closely coupled to local tissue metabolic rates in the brain[71]. Regional modulations in neuronal electrical activity are thought to cause similar modulations in the metabolic rate which in turn result in changes in local blood flow. This idea has formed the basis for PET brain activation studies, and close correlation between cerebral blood flow, and oxygen and glucose uptake has been demonstrated in the 'resting' brain. Coupling between local blood flow and metabolic rate also formed the basis for the earliest fMRI techniques, in which a bolus of contrast agent injected into the subject was imaged as it entered the brain. These techniques were similar to PET activation studies in that they sought to measure blood flow based on signal changes caused by the uptake of a bolus of tracer.

In 1985 Peter Fox and Marcus Raichle investigated the coupling between cerebral blood flow and cerebral oxygen uptake during brain activation[23]. They discovered that the increase in cerebral blood flow could greatly exceed the local in-

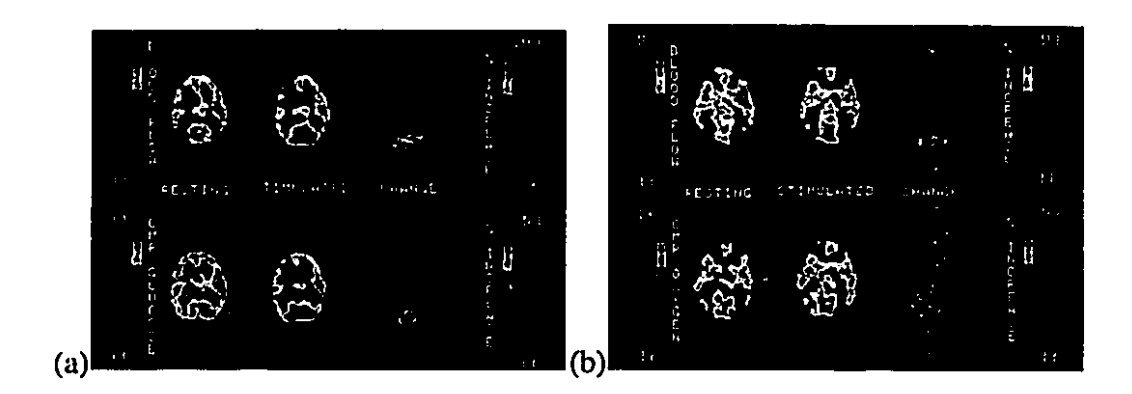


Figure 3.3: (a) A significant change in blood flow is apparent in the visual cortex during activation, coupled with a readily observable change in glucose uptake; (b) in a different subject, a similar change in blood flow is accompanied by very little change in oxygen uptake (From [24]).

crease in oxygen uptake. For vibrotactile stimulation of the finger pads they found a mean increase in local blood flow of 29% in primary sensory cortex with only a 5% increase in oxygen uptake.

They went on to investigate coupling between blood flow, glucose uptake, and oxygen consumption in the primary visual cortex during visual stimulation[24]. They found that, while local blood flow and glucose uptake increased by approximately 50% during such stimulation, oxygen consumption increased by only 5% on average. This corresponds to a significant drop in the fraction of available oxygen that is extracted from the flowing blood, implying an increase in blood oxygenation during such activation. Figure 3.3 shows two images which illustrate their results.

Fox and Raichle compared their results to observations made at the MNI by the neurosurgeon Wilder Penfield, who reported instances during focal brain seizures in which the veins near the foci underwent a change in color from the normal veinous blue towards the red of arterial blood. Such a change in color indicates a change in oxygen saturation[63]. Comparisons were also drawn with the results of Cooper et al., who were cited for their demonstration of increased blood oxygenation in response to visual stimulation and motor tasks, using intracerebral electrodes, in humans[18].

These findings suggest that local activation of brain tissues may in general be accompanied by local increases in blood oxygenation. In the next section we will look at the effect this has on the nuclear magnetic resonance signal of blood and perfused tissues¹.

3.3 Physics

3.3.1 The NMR Signal

In the previous section the relationship between local metabolic rates in brain tissues and blood oxygenation level was established. Now we will link the blood oxygenation level in tissues to the behaviour of the magnetic resonance signal they emit. In this section, the discussion of NMR principles will be restricted to macroscopically heterogeneous tissue samples, with no attention paid to imaging considerations. These will be dealt with in Chapter 4.

The signal used in MRI comes from hydrogen nuclei, most of which are found

¹An increase in the blood flow rate without a corresponding acceleration in oxidative metabolism should also result in a decrease in the concentration of veinous CO₂; however, no studies of the influence of CO₂ concentration on the blood NMR signal could be found.

in the water molecules of tissues. The hydrogen nucleus consists of a single proton and can be thought of as a distributed positive charge possessing spin angular momentum I. This is equivalent to a ring of current with an associated magnetic dipole moment μ . These quantities are related by the expression

$$\mu = \gamma h \mathbf{I}/(2\pi) \tag{3.1}$$

where γ is the *gyromagnetic ratio* of the nucleus and h is Planck's constant. For hydrogen, γ is 267.512 x $10^6 \text{rad}\text{T}^{-1}\text{s}^{-1}$. In NMR literature, the relevant nuclei are often referred to as *spins*.

In a magnetic field, a dipole experiences a force aligning it with the field. The strong field in an MR imager (typically 1.5 T) exerts this effect on the spins in tissue samples, but rules governing the selection of quantum states prohibit complete alignment of individual proton magnetic moment vectors with this field. In the case of the hydrogen nucleus, the projection of μ along the applied field B_0 may assume one of two discrete values which are equal in magnitude but opposite in sign, as shown in Figure 3.4.

Each moment vector then has a longitudinal component aligned either with or against the main field, and a transverse component perpendicular to it. Alignment of the longitudinal component against the field is less favorable from an energy standpoint, but the energy difference between the two states is so small that at room temperature there is only a slight difference in their populations. Nonetheless, the small excess of spins in the lower energy parallel alignment leads to a net bulk magnetization vector M (the mean magnetic moment per unit volume) that can be observed using NMR techniques. This is shown in Figure 3.5.

The incomplete alignment of the individual spins causes them to precess about

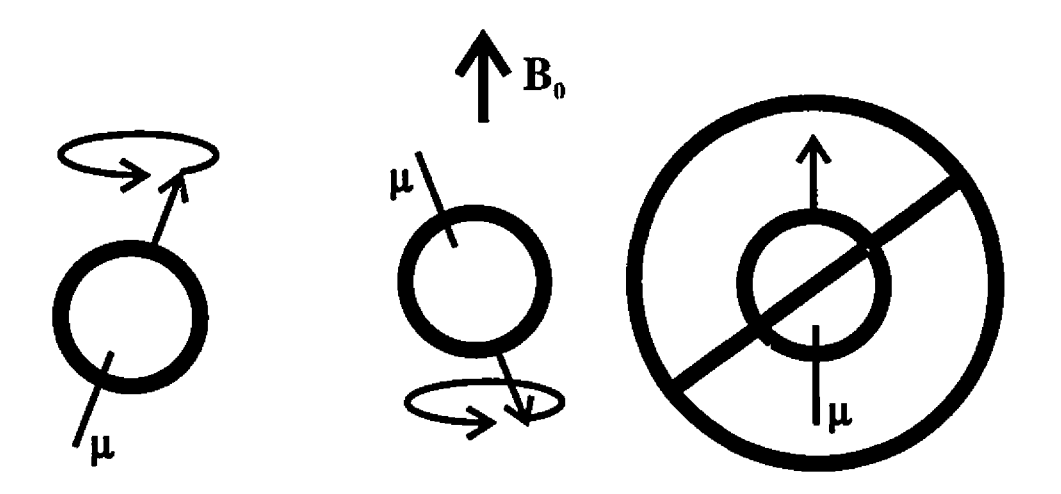


Figure 3.4: Permitted alignments of proton dipole moments (μ) in a magnetic field $\mathbf{B_0}$.

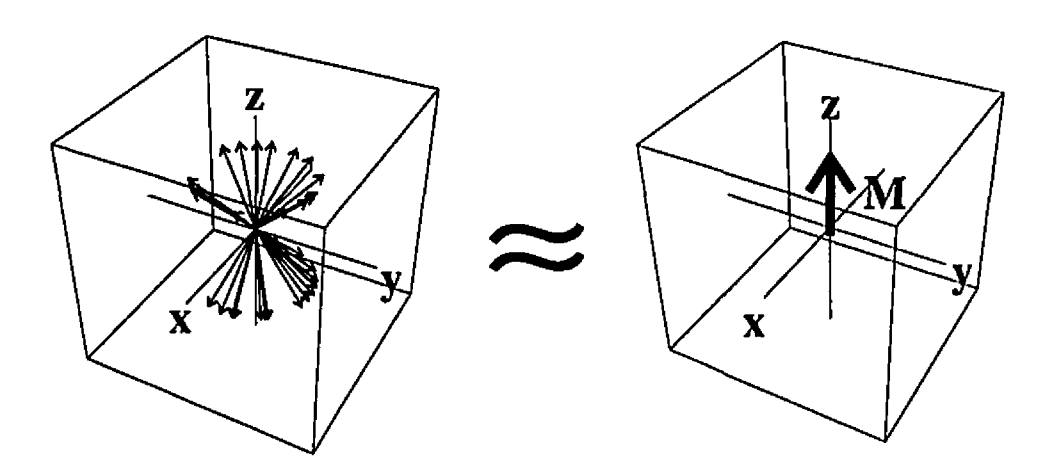


Figure 3.5: Macroscopic magnetization from spins in a magnetic field along the z axis. A slight imbalance in the numbers of protons in the parallel and anti-parallel states leads to macroscopic magnetization M in the z direction.

the main field axis at the Larmor frequency ω_0 , which is determined by the gyromagnetic ratio γ of the proton and the magnitude of the main field (B_0) at the location of each proton:

$$\omega_0 = \gamma B_0. \tag{3.2}$$

Equation 3.2 is known as the Larmor relationship and the precession frequency ω_0 is also referred to as the resonant frequency. The hydrogen nuclei of water molecules in a 1.5 T field precess at 63.9 MHz.

At equilibrium the transverse components of the nuclear dipoles are randomly oriented, leading to a net transverse component of zero for the macroscopic magnetization vector. A non-zero transverse component would precess at the Larmor frequency in accordance with the laws of rotational dynamics, leading to a time-varying magnetic field flux in the region of the sample and generating a radio frequency (RF) signal.

In NMR techniques, the macroscopic magnetization vector \mathbf{M} is rotated away from the longitudinal axis by applying RF energy at ω_0 that is polarized perpendicular to the main static field. The energy of photons at this frequency is equal to the energy difference between the two proton alignment states, so energy level transitions are stimulated, leading to a shift away from thermal equilibrium.

The process can be described more naturally using the language of classical dynamics. If the population of nuclear dipoles is considered in a reference frame that is rotating about the z axis at the Larmor frequency, then the magnetic vector of the applied RF radiation, B_1 , will appear stationary and the B_0 term will be zero. Since B_1 is perpendicular to M, M will precess about B_1 away from the z axis. Transverse magnetization is thereby generated, while the longitudinal mag-

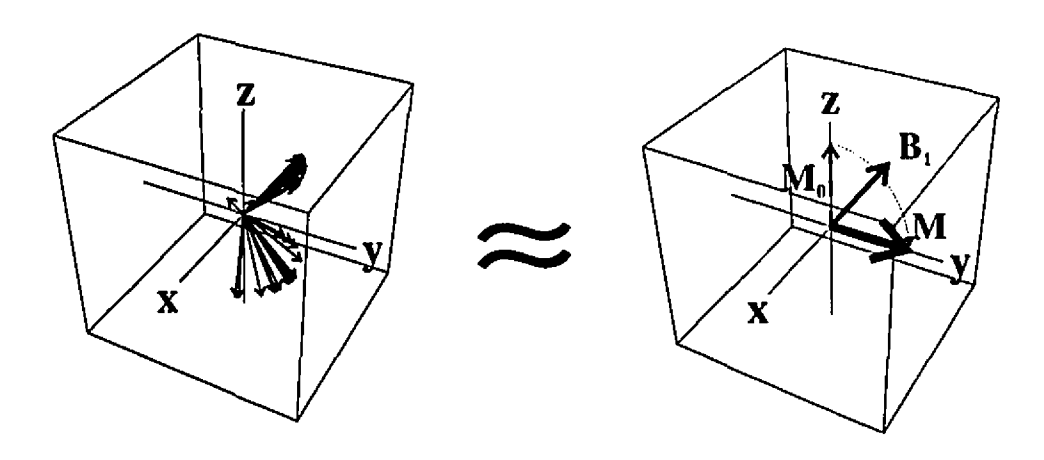


Figure 3.6: Effect of a 90° RF pulse in the rotating frame: Immediately following the pulse there are equal numbers of protons in the high and low energy states, and the distribution of transverse components is skewed toward the positive y-axis. The z component of the magnetization then cancels to zero, and there is a net component in the y direction. (For this illustration the coherence of the nuclear dipole vectors along the y axis has been exaggerated.)

netization decreases. The precession of the transverse component of M at ω_0 in the laboratory frame can be conveniently ignored in the rotating frame. The RF energy is usually applied as a shaped *excitation* pulse, which is characterized by the (flip) angle θ through which it rotates M. The effect of a 90° RF pulse along the negative x-axis is illustrated in the rotating frame diagram in Figure 3.6.

The transverse components thus created can induce a signal in an RF receiver coil as they precess about the main field axis. This signal decays with time, so it is commonly referred to as the *free induction decay* or FID. The time from excitation to measurement of the NMR signal is termed the echo time, or TE.

3.3.2 Relaxation Behaviour

Transverse Relaxation

The NMR signal decays with time following the excitation pulse because the macroscopic magnetization vector \mathbf{M} in a volume element dV is the superposition of a large number of nuclear dipole moment vectors, associated with protons which may be exposed to slightly varying field strengths. The corresponding distribution of proton precession frequencies leads to a decrease in the induced RF signal with time as coherence is lost. This loss of phase coherence is known as transverse relaxation.

The rotating reference frame used to describe the effect of an excitation pulse is also useful in understanding transverse relaxation. Figure 3.7 shows, in the rotating frame, a group of dipole moment vectors which start out tightly grouped together and end up dispersed at different angles around the z-axis. The variations in local field strength experienced by different protons are due to a combination of inhomogeneities in the applied field (B₀) and magnetic field contributions from the molecular environment. Proton transitions between the high and low energy alignment states also reduce phase coherence, but this mechanism does not play a significant role in functional MRI and further mention is deferred to the section on longitudinal relaxation. Transverse relaxation due to spatial variations in field strength is the process which leads to BOLD contrast, so it will be examined in detail here.

The amount of angular dispersion which occurs over a given echo time depends on the range of precessional frequencies, which in turn depends on the range of local field strengths present in the volume. It is clear that the transverse relaxation

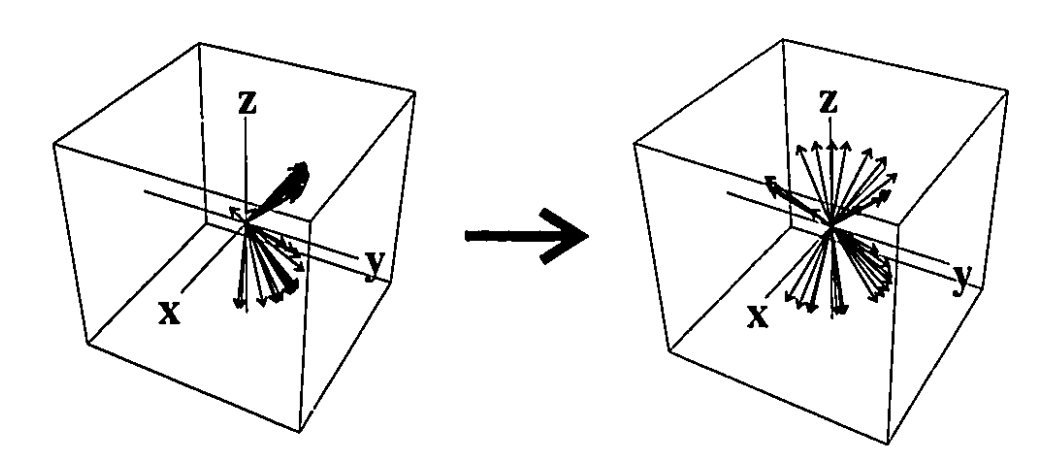


Figure 3.7: Dephasing in a group of nuclear dipoles. The net transverse magnetization M_{xy} decreases as coherence along the y-axis is lost.

rate observed depends greatly on the size of the volume element under consideration, so the process will be examined at several different scales.

If one considers a volume of tissue containing a single proton, then macroscopic quantities like magnetization are not applicable. If the volume is expanded to contain larger numbers of protons, then at some point it will become possible to apply statistical concepts such as the mean magnetic moment per unit volume. In a region that is only just large enough for such macroscopic quantities to be well defined, the NMR signal produced would be very small. The range of applied field intensities seen within such a volume would also be small, however, so the transverse relaxation rate would be low. Dephasing would occur nonetheless, primarily due to dipolar interactions between the spins in individual water molecules.

Dipolar interactions in water molecules occur because each of the two hydrogen atoms exerts a magnetic field contribution in the direction of the applied field at the position of its counterpart on the molecule. The magnitude of this contribution depends on the orientation of the molecule, which undergoes rotational and translational Brownian motion. Because the orientation of the water molecules is random, there is a small spread in the distribution of local field strengths experienced by spins in the sample. The Brownian tumbling of the water molecules leads to some averaging of the field perturbations over time, which reduces the spread somewhat. Environments which restrict the motion of water molecules reduce this averaging effect, leading to faster transverse relaxation. The distribution of field intensities experienced by the proton population is roughly Lorentzian in nature, leading to approximately monoexponential signal decay with a time constant designated T2.

Bloembergen[12] has presented a rigorous mathematical description of this process, in which the following expression was used to relate T2 to the other physical properties of a sample:

$$\frac{1}{\text{T2}} = \frac{3}{20} \frac{\gamma^4 (h/2\pi)^2}{r^6} \tau_c \left(3 + \frac{5}{1 + (\omega_0 \tau_c)^2} + \frac{2}{1 + (2\omega_0 \tau_c)^2} \right)$$
(3.3)

where r is the distance between the hydrogen atoms of a water molecule, and τ_c is the correlation time of the exponentially decaying correlation function used to model the field perturbations due to Brownian motion. The correlation time τ_c for water undergoing Brownian motion depends approximately on its viscosity η , molecular radius a, and the temperature T according to the following formula:

$$\tau_c = \frac{4\pi\eta a^3}{3kT}. (3.4)$$

Equations 3.3 and 3.4 show that the time constant T2 depends only on the molecular environment of a sample. If one considers a much larger volume, then macro-

scopic inhomogeneity of the applied field becomes the predominant source of dephasing.

The magnets typically employed for whole body imaging provide a field that is homogeneous to within several parts per million over a 50 cm diameter spherical volume. The residual inhomogeneity contributes significantly to the transverse relaxation rate, and the signal decay that is actually observed in MRI systems is considerably faster than would be expected due to microscopic T2 effects alone. The introduction of a sample or patient into the magnet also perturbs the magnetic field intensity, and sizeable gradients in the applied field strength can exist near tissue-air interfaces. Typical T2 values for tissues are on the order of hundreds of milliseconds but in regions near tissue-air interfaces, such as the nasal sinus, the FID signal can decay completely in several milliseconds. The decay observed due to transverse relaxation from these sources is only approximately exponential, but it is commonly characterized using the time constant $T2' \approx \gamma \Delta B_0/2$ where ΔB_0 represents the range of field shifts present in the sample. The net relaxation rate, generally denoted $1/T2^* = 1/T2 + 1/T2'$, is usually dominated by 1/T2'.

The T2 and T2' effects just described represent extremes in terms of the reversibility of the processes. T2' dephasing due to macroscopic field gradients, in which field changes occur over a distance scale of millimeters or more is reversible because the field perturbation experienced by an individual spin is static over time. Such static inhomogeneity and the resulting dephasing can be reversed or refocused via spin-echo techniques. These methods employ a 180° RF pulse at time TE/2 which inverts the phase accrued by the protons in a sample. Continuation of the phase evolution of the spins in the presence of static inhomogeneities leads to a re-establishment of coherence at time TE, producing the spin echo[34]. Imaging

techniques in which the FID is utilized instead of the spin echo are called gradient echo (GE) techniques and are more sensitive to static inhomogeneities.

On the other hand, T2 dephasing due to dipolar interactions is *irreversible* because the field perturbation seen by an individual hydrogen nucleus changes rapidly as its host water molecule undergoes Brownian motion.

The mechanism for BOLD contrast appears to be a partially reversible process which lies between these two extremes: the diffusion of spins through static microscopic gradients. Microscopic structures (such as deoxygenated red blood cells) whose magnetic susceptibility differs from that of the surrounding medium can introduce shifts in the field strength seen at locations several microns apart. Water molecules in biological tissues undergo diffusion at rates sufficient for many of them to travel such a distance during a typical NMR acquisition sequence. The degree to which such dephasing is reversible depends on the time scale at which the process is considered.

One millisecond after excitation, the field change experienced by a particular spin due to diffusion through a microscopic gradient will typically be very small, so although it may have undergone dephasing with respect to its neighbours, the dephasing can be refocused (using spin-echo techniques) because on this time scale the field shift is fairly static.

If the system is considered 50 ms after excitation, then the same spin will have acquired an amount of phase with respect to its neighbours that is determined by the random path it has taken through any microscopic field gradients around it. Because this path is not reproducible, it is no longer possible to reverse the dephasing. As we will see in the following section, gradient echo sequences with long TE and no refocusing RF pulse are therefore highly sensitive to changes in blood oxygena-

tion.

Longitudinal Relaxation

The longitudinal magnetization component of a sample also relaxes exponentially toward thermal equilibrium following excitation, with time constant T1. This occurs as protons undergo quantum transitions between the high and low-energy alignment states. More transitions to the low energy state occur, and eventually the equilibrium distribution is restored. The transitions occur via a stimulated emission process, so the rate of relaxation depends on the amount of Brownian-motion-induced field fluctuation at the Larmor frequency. As these transitions themselves add to the low frequency field fluctuations experienced by the protons, they contribute to the transverse relaxation rate as mentioned in the previous section. For this reason, the transverse relaxation rate of a sample is always higher than its longitudinal rate. Bloembergen[12] has derived the following expression for T1:

$$\frac{1}{\text{T1}} = \frac{3}{10} \frac{\gamma^4 (h/2\pi)^2}{r^6} \tau_c \left(\frac{1}{1 + (\omega_0 \tau_c)^2} + \frac{4}{1 + (2\omega_0 \tau_c)^2} \right)$$
(3.5)

where the quantities are as defined for equation 3.3 and again there is dependence only on molecular characteristics.

Longitudinal relaxation is not as important to fMRI contrast as transverse relaxation, but it is still an important consideration in pulse sequence design and optimization. Repetition of excitation pulses at intervals much shorter than T1 leads to a steady state in which the longitudinal magnetization of a sample is considerably suppressed, or *saturated*, especially if large flip angle pulses are applied. This determines the initial amplitude of the FID, which depends on the amount of longitudinal magnetization present prior to excitation and the flip angle θ used. The

steady state signal level in static tissue is usually a well defined function of the T1 of a sample and the pulse repetition rate. Blood flow through a region of tissue can introduce fresh, unsaturated spins, leading to a more complicated dependence of the signal level on the blood flow rate.

3.3.3 Steady State Signal Behaviour

The behaviour of the macroscopic magnetization M under the influence of the net magnetic field B along the z axis and including longitudinal and transverse relaxation is described by the empirical Bloch equation[11]:

$$\frac{d\mathbf{M}(t)}{dt} = \mathbf{M}(t) \times \gamma \mathbf{B}(t) - \frac{(M_x(t)\mathbf{i} + M_y(t)\mathbf{j})}{\mathrm{T}2} - \frac{(M_z(t) - M_0)\mathbf{k}}{\mathrm{T}1}$$
(3.6)

where M_x , M_y , and M_z are the components of the vector \mathbf{M} , M_0 is the equilibrium longitudinal magnetization, and \mathbf{i} , \mathbf{j} , and \mathbf{k} are unit vectors in the \mathbf{x} , \mathbf{y} , and \mathbf{z} directions, respectively.

Equation 3.6 can be solved to describe the steady state transverse magnetization M_{xy} observed in a sample with equilibrium magnetization M_0 at echo time TE following repeated excitation at repetition intervals TR with RF pulses of flip angle θ [28]:

$$M_{xy} = M_0 e^{-\text{TE/T2}^*} \sin(\theta) \frac{1 - e^{-\text{TR/T1}}}{1 - \cos(\theta) e^{-\text{TR/T1}}}$$
(3.7)

where the first exponential term reflects T2* decay following excitation, the $\sin(\theta)$ term accounts for the amount of transverse magnetization generated for the flip angle θ , and the final fractional term represents the suppression of the longitudinal magnetization from the equilibrium value of M_0 to some lower steady state value. Equation 3.7 is only valid if the transverse magnetization is zero immediately prior

to each excitation pulse. Unless the sequence TR is considerably longer than T2*, the transverse magnetization must be set to zero or *spoiled* by varying the phase of successive RF pulses or applying large field gradients to the sample[80].

3.4 Relaxation in Perfused Tissues

Human blood consists of red blood cells (erythrocytes), white blood cells (leukocytes), and platelets, suspended in the plasma. The size of the formed (non-liquid) elements ranges from 2 microns for platelets to about 7 microns for red and white blood cells. A cubic millimeter of blood contains approximately 4 million to 6 million red blood cells, 4,000 to 10,000 white blood cells, and 150,000 to 400,000 platelets[32]. The primary constituents on a gross structural scale are thus red blood cells and plasma, as can be seen in Figure 3.2.

The NMR relaxation properties of blood are determined by a number of parameters, including temperature and the erythrocyte volume concentration (hematocrit). These two parameters are fairly constant under normal physiological conditions, with values of 37° C and 45% being typical for temperature and hematocrit, respectively[32]. These physical variables determine T1 and T2 through the restriction of Brownian motion in water molecules, which influences the dipolar interactions leading to longitudinal and transverse relaxation as described in Section 3.3.2. Variations in the transverse relaxation rate of blood observed *in vivo* are due primarily to changes in the oxygenation state of crythrocytes, which lead to changes in the electronic structure and magnetic susceptibility of their resident hemoglobin molecules.

Electrons possess magnetic dipole moments similar to those of nuclei described

in Section 3.3.1. Since the electronic charge magnitude is equal to that of the proton, while electrons are considerably smaller and more mobile, the electronic dipole moment is 658 times that of the hydrogen nucleus[31]. In most compounds present in tissues in any appreciable concentration, however, electrons are paired in such a way that the net electronic magnetic moment is zero. Such materials are termed diamagnetic, and their only interaction with an applied magnetic field is a weak opposition due to a duced electronic currents.

Compounds which possess one or more unpaired electron spins are said to be *paramagnetic*. These compounds can exert considerable contributions to an applied field as the unpaired electron magnetic moments will align with the applied field and add to it. The fundamental quantum of angular momentum of an electron is assigned the value of $\frac{1}{2}$, and the variable S is used to denote the total angular momentum of an atomic or molecular system. As is the case for nuclei, the electronic magnetic moment is proportional to the total angular momentum.

When a molecule of oxyhemoglobin releases its oxygen load, the iron of the heme component changes spin state from diamagnetic low-spin (S=0) Fe II to paramagnetic high-spin (S=2) Fe II. This leads to an observable change in the relaxation rate of blood. There are other compounds in brain tissues that contain iron, such as mitochondrial cytochromes involved in the production of ATP, but only hemoglobin is known to exhibit such variable paramagnetism under normal physiological conditions.

Figure 3.8 shows the results of work done by Thulborn *et al.* at Oxford in 1981[73]. They measured the T1 and T2 of water protons in rat blood at varying levels of oxygenation and found that the transverse relaxation rate 1/T2 decreased quadratically with increasing blood oxygenation, while T1 exhibited little

change. The T2 variation with oxygenation became more pronounced at higher field strengths.

A Carr-Purcell-Meiboom-Gill (CPMG) spin-echo pulse sequence was used for the T2 measurements. This sequence is designed to determine T2 in situations where diffusion through static field gradients occurs[50]. Their measurements indicated that the change in T2 was due to the diffusion of spins through magnetic field gradients surrounding deoxygenated red blood cells.

The change in resonant frequency at 6.4 T of protons in whole blood over the physiologically observed range of blood oxygenation levels was also determined. They found a frequency shift of 89 Hz from 270 MHz (for fully oxygenated blood), which corresponded to a change in bulk susceptibility of 0.2×10^{-6} for the red blood cells. While these experiments were performed on high field NMR spectroscopy systems, similar results have been achieved more recently using MR imaging systems at 1.5 T[78].

These findings, together with those of Fox and Raichle described in Section 3.2.2, suggest a means of using NMR to detect focal activation in brain tissues. To understand the implications of Thulborn's results to the NMR signal of brain tissue, it is necessary to examine the microvascular structure of such tissues.

At the microscopic level, brain tissues consist of the functional cells (neurons and connective or *glial* cells) interlaced with a matrix of capillary vessels. In Figure 3.1 the relative sizes of a neuron and capillary were shown, and Figure 3.9 illustrates the density of the capillary matrix. From these images it is clear that a sample of brain tissue contains a heterogeneous mixture of capillaries, functional cells, and glial cells.

PET measurements[47] have shown that the total volume fraction of brain tis-

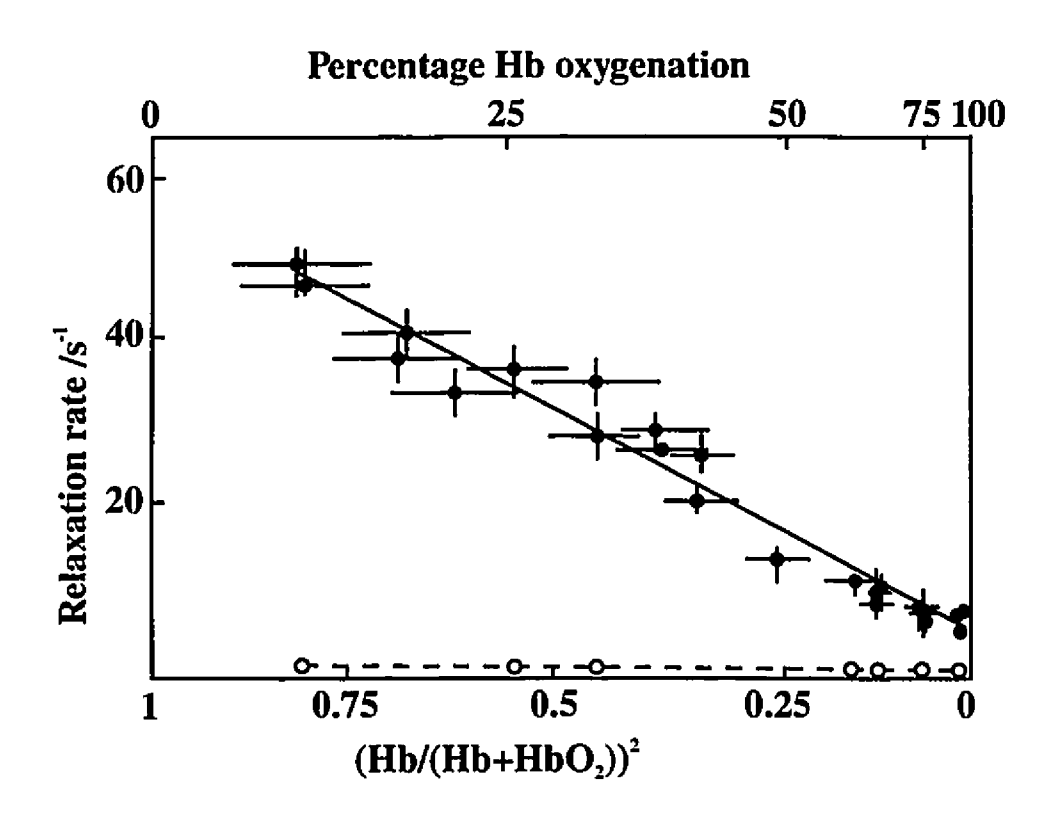


Figure 3.8: Relaxation rate dependence on blood oxygenation at 4.3 T. Transverse relaxation rate (solid line) decreases quadratically with increasing blood oxygenation. The longitudinal relaxation rate (dashed line) exhibits little change with oxygenation (from [73]).

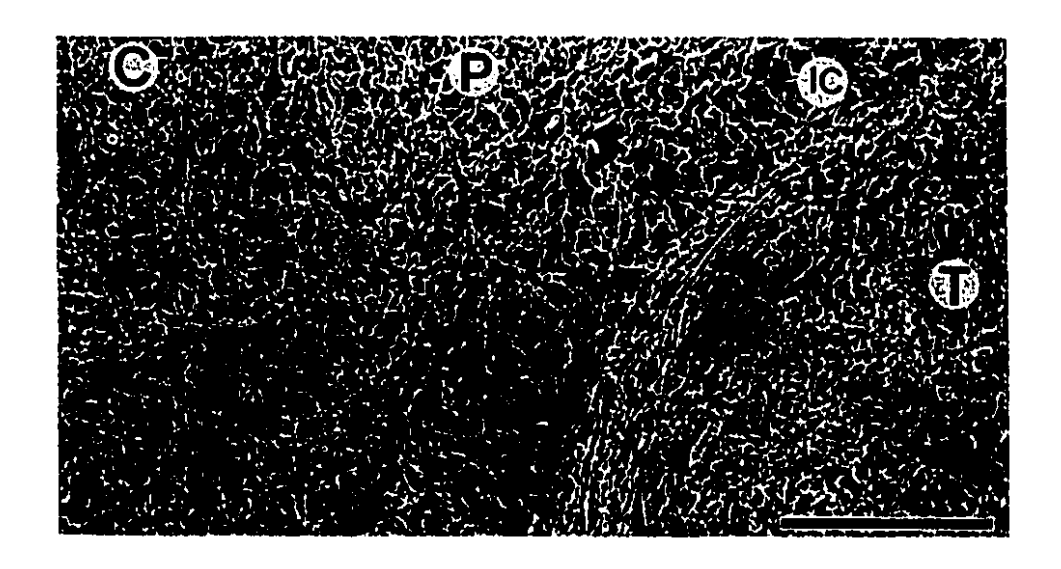


Figure 3.9: (C) Capillary matrix in rat cerebral cortex, (IC) internal capsule, and (P) putamen. Functional tissues have been removed to show capillaries only. Scale bar is 1 mm. (From [79]).

sue occupied by blood is about 4% in humans, and it has long been recognized that changes in the susceptibility of erythrocytes could influence bulk tissue relaxation rates. The results of the Oxford group's experiments showed a definite change in the relaxation rate of the blood itself, and Ogawa's initial description of the BOLD phenomenon suggested that the susceptibility difference in erythrocytes would result in field gradients felt by water molecules in the surrounding tissues as well[59].

The relative significance of the intra and extra-vascular compartments at various field strengths has been the subject of debate since the earliest observations of BOLD signal changes, and a number of models for transverse relaxation in the extravascular space due to erythrocyte susceptibility shifts were initially proposed[60, 13, 41]. These have been used in Monte Carlo simulations to make quantitative predictions of activation-induced signal changes in brain tissues. These predictions have been systematically lower than those observed experimentally, however, while models including an *intravascular* spin contribution have yielded estimates which are closer but still somewhat low[15].

Moreover, a number of experimental studies designed to assess the importance of intravascular water in activation-induced signal changes at 1.5 T have suggested that it is the dominant source. Several groups have performed diffusion weighted functional imaging in which the signal from spins diffusing at selected rates was selectively attenuated [14, 15, 53, 75]. When spins diffusing at rates at or above those associated with flow in capillaries were suppressed, the functional signal changes were reduced by up to two thirds.

Monte Carlo simulation results published by Boxerman *et al.* for a 40 ms echo time at 1.5 T indicate that a 50% rise in blood oxygenation can lead to a signal increase of one percent in extravascular spins, and up to 100% in intravascular

spins[15]. In spite of the small cerebral blood volume (CBV) fraction, the large intravascular changes comprised about two thirds of the approximately 4% total signal change predicted by this model for typical activation at 1.5 T.

Although experimentally observed activation-induced signal changes are often near the predicted 4% level, increases of up to 100% have been reported[33, 44]. There are two factors which are thought to contribute significantly to this discrepancy. The first is the influence of blood flow, described in Section 3.3.2. Changes in local flow rates can lead to large shifts in the intensity level, and there has been concern that neuronal activation can affect blood flow in vessels a considerable distance from the actual activation site[21, 25, 33, 42, 44]. Large vessels have frequently been identified as sources of such large signal changes, but the significance of this is poorly understood. Direct optical flow measurements on the exposed cortex of monkeys have indicated that at the capillary level, highly localized changes in blood volume and oxygenation occur in conjunction with neuronal activity[27]. These studies only examined small patches of the cortical surface, however, and it was not possible to observe blood vessels more than one or two centimeters from the exposed site.

A second reason for the difference between experimentally reported values of activation-related MR signal changes and those predicted by Monte Carlo simulation may be due to the assumption that the cerebral blood volume is 4%. The spatial resolution of MRI is such that the relevant sample volume is several cubic millimeters, and the CBV in such a small volume can be as high as 100% if it occupies a blood vessel. The assumed 4% value probably represents a lower limit corresponding to the density of the capillary bed. Post-mortem studies of human vasculature[19] suggest that the true CBV values in a 20 mm³ volume (derived

from the $1.7 \times 1.7 \times 7$ mm dimensions of a typical fMRI voxel) can range anywhere from 4% to 100%. As the spatial resolution of the study decreases, the CBV will converge to the gross mean value.

The regional variability of CBV was also demonstrated in a 34 subject PET study conducted by Leenders *et al.* Mean cortical CBV values ranging from 3.5% in parietal cortex to 8.6% in occipital cortex were measured [47], with white matter CBV significantly lower at 2.7%. The spatial resolution of this study was 16 mm and large visible blood vessels were excluded from the regions of interest (ROIs), so the measurements do not reflect the true range of CBV values.

If the NMR signal due to intravascular spins can indeed double as suggested by Boxerman's Monte Carlo results, then MRI voxels which are completely occupied by (venous) blood vessels could exhibit equally large changes. As the size of blood vessel increases, however, so does the number of smaller vessels which feed it. If only some of these smaller vessels drain activated regions, then the highly oxygenated blood from the activated regions will be diluted with less oxygenated blood from dormant regions.

Large blood vessels of 0.5 mm diameter and above can be localized using magnetic resonance angiography (MRA) techniques, and MRI techniques for determination of CBV with high spatial resolution using contrast agents have been proposed [4, 69, 9]. The relationship between the size of activation-induced signal changes and the competing factors of blood vessel size and dilution by smaller feeding vessels has not been extensively studied, however, so the distance that a blood vessel of a given size may be removed from an activated neuronal population and still exhibit significant signal changes is not known. Further modeling and experimentation are required to explain the physiological significance of BOLD

signal changes in large blood vessels and establish the attainable spatial resolution of fMRI techniques.

3.5 Discussion

In spite of the various uncertainties, it is clear that focal brain activation can increase tissue NMR signal in spoiled gradient echo sequences via two mechanisms: Increases in LCBF can lead to signal enhancement due to the flow of unsaturated spins into the sample region, and increases in blood oxygenation lead to signal increases from the lengthened T2* of the more highly oxygenated blood. The inflow effect is increased at high field strength (due to longer T1 values), large flip angles, and short sequence repetition times (TRs) while the BOLD effect is independent of flip angle but increases with echo time and field strength.

Chapter 4

Functional MR Imaging

4.1 Introduction

The previous chapter dealt with the NMR relaxation behaviour of tissues. This chapter will focus on how these physical processes can be manipulated to generate images depicting regional differences in relaxation rates. Since different soft tissue types exhibit a wide range of NMR characteristics, such images provide excellent delineation of anatomical structures. We have seen how functional changes can lead to dynamic changes in relaxation rates, and will now examine ways that this can be exploited to locate regions of changing metabolic activity.

In the first section the basic MR image formation process is reviewed, and a simple 2D gradient echo sequence for functional imaging is described. The various noise sources relevant to fMRI are then discussed and illustrated with dynamic images of a healthy volunteer acquired using this sequence. Next, the problem of statistical analysis of fMRI data is briefly examined. Several analysis techniques

are applied to the same raw data and the results are compared.

4.2 Data Acquisition

A magnetic resonance imaging system consists of a large main magnet, a set of resistive gradient magnet coils, radio frequency (RF) transmit and receive coils, amplifiers to drive the resistive magnets and RF transmit coil, and an RF receiver and digitizer to record the NMR signal from tissues. The system is controlled by one or more computers. Typical main field strengths for clinical imaging systems range from 0.1 to 1.5 T and either resistive or superconducting magnets are used. Research and spectroscopy systems with main field strengths of over 7 T also exist, but with considerably smaller bore sizes than those used for human imaging. The gradient coils produce fields in the same direction as the main field, but they are designed in such a way as to produce linear variations (gradients) in the field strength independently in the x, y, and z directions. Figure 4.1 shows a block diagram of the components of a typical MRI system.

The MRI system used for this work was a Philips Gyroscan ACS-2 with a main field strength of 1.5 T. All pulse sequence programming was done using Philips' Gyroscan Object-Oriented Acquisition Language (GOAL-C Rel. 3.2), an object-oriented extension of C. Compiled code was run on a Digital Equipment Corporation (DEC) Alpha workstation which was the host computer for the MRI system as well as on a 68010 dedicated controller for the spectrometer subsystem.

To acquire an MR image, the body is placed in the strong field of the main magnet and repeatedly exposed to pulsed RF radiation. Following each excitation pulse, the transverse magnetization in the tissues is manipulated using the resis-

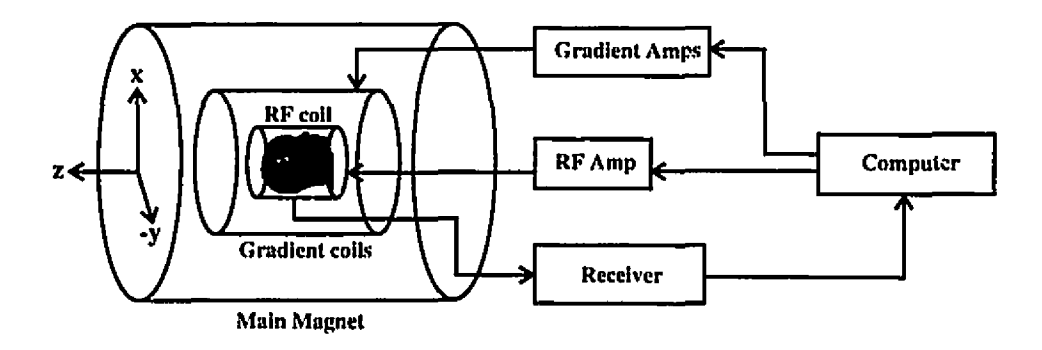


Figure 4.1: Schematic diagram showing the components of an MRI system. The xyz coordinate system used in this chapter is illustrated in this diagram. For brain studies, the subject's head is placed in the RF receive coil (Adapted from [[58]])

tive magnet coils to produce field gradients over the volume of interest. The FID signal, thus modulated, is received, digitized, and stored on the system computer. For a conventional image, over 100 such sequence repetitions are typically performed. Once these are acquired, the computer processes the data to produce an image, which is a cross sectional representation of the tissue structure within the field of view. Figure 4.2 shows typical MR images of a human head.

For the sake of consistency with PET activation studies performed at our lab, nuclear medicine conventions for the display of axial and coronal images have been followed (i.e. axial slices are presented as though viewed from above the subject and coronal slices are shown as rear views). Note that this differs from conventions employed in diagnostic radiology and in much of the MRI literature.

In this section, the physical and mathematical basis of the image formation process will be examined in sufficient detail to permit analysis of functional imaging techniques. 2D gradient echo methods, which are important for functional imag-

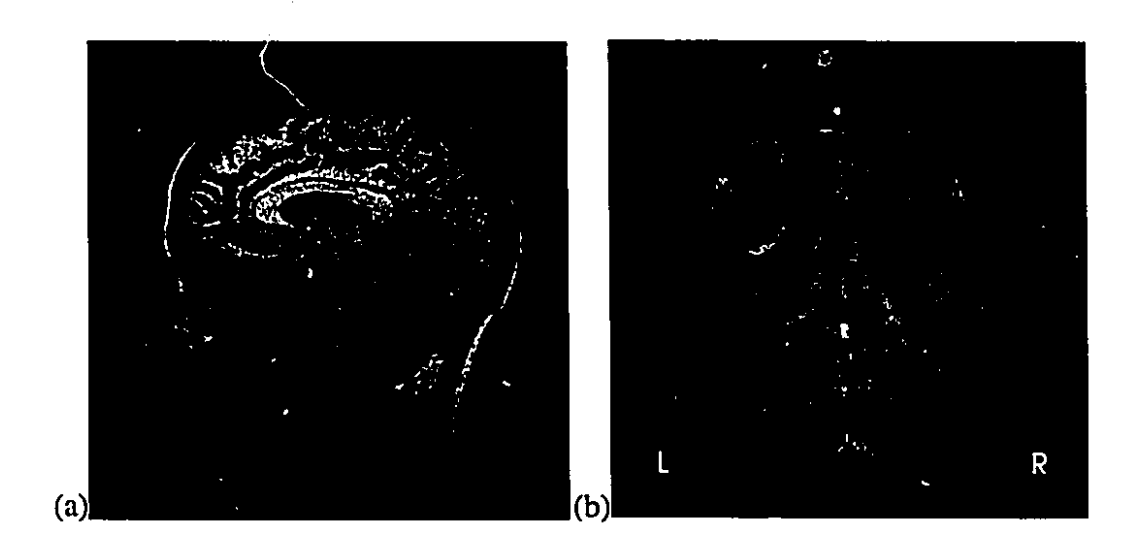


Figure 4.2: Examples of MR images, demonstrating different contrast properties and slice orientations possible: (a) shows a T1 weighted MR image of the head, comprised of a 256 x 256 grey-scale matrix whose elements reflect the magnitude of the magnetization vector over the sagittal image plane through the subject's head. (b) shows a T2* weighted image of an oblique axial cross section.

ing on standard clinical MR systems, will be emphasized and a simple 2D sequence optimized for functional imaging will be described. This sequence will serve as a reference point from which to evaluate the more advanced techniques introduced in the following chapters.

4.2.1 Selective Excitation

The transmitter coil used to generate RF excitation pulses usually encompasses the entire body part that is to be imaged. Emissions from this coil will therefore irradiate all tissues in a fairly large volume so, in order to image thin cross sectional views of the body, *selective excitation* must be used to restrict excitation to the desired image 'slice.'

Selective excitation is achieved by using the resistive coils to create a linear slice selection gradient in the applied field perpendicular to the target slice. Because the proton resonant frequency is then a linear function of position along a line normal to the slice, RF radiation of a given frequency will only excite spins in a particular plane perpendicular to the applied gradient. The bandwidth associated with a shaped RF pulse determines the frequency range, and hence the thickness, of the excited slice.

The FID signal observed following selective excitation will originate entirely from spins within the desired slice plane, providing the first dimension of spatial localization. The next section will describe how the remaining two dimensions of 'in-plane' spatial information are obtained.

4.2.2 Fourier Encoding

In Chapter 3 the concept of transverse magnetization was introduced. Following excitation of a tissue sample, the magnetization vector M possesses a transverse component \mathbf{M}_{xy} , which is conveniently expressed as a complex quantity with magnitude M_{xy} and phase ϕ in the rotating frame:

$$\mathbf{M}_{xy} = M_{xy}e^{-i\phi}. (4.1)$$

The transverse magnetization is time dependent, due to the relaxation of M_{xy} with time constant T2* and drift in ϕ if the sample is off resonance; however, M_{xy} will not be explicitly written as a function of time as it varies extremely slowly with respect to the rate of precession in the laboratory frame.

An RF receiver coil placed near the sample and oriented perpendicular to the transverse plane will enclose some magnetic flux Φ associated with the coherent group of nuclear dipoles. As \mathbf{M}_{xy} precesses, Φ will change as the dipolar field changes direction. A coil thus positioned will experience an induced electromotive force ϵ in accordance with Faraday's law:

$$\epsilon = A \frac{\partial \Phi}{\partial t}.\tag{4.2}$$

This is the NMR signal, or FID. The quantity A is a proportionality constant which will be retained for the remainder of this exposition to reflect the (complex) scaling properties of the RF reception system.

The flux $\Phi(t)$ at a given instant is proportional to the component of \mathbf{M}_{xy} along the central axis of the coil, a relationship which can be expressed as follows:

$$\Phi(t) = A \cdot \text{Re}(\mathbf{M}_{xy}e^{-i\omega_0 t}) \tag{4.3}$$

where \mathbf{M}_{xy} is in the rotating frame and the complex factor $e^{-i\omega_0 t}$ represents precession at the Larmor angular velocity ω_0 . Taking the time derivative of this expression as per Equation 4.2 and ignoring constant factors and the relatively small time dependence of \mathbf{M}_{xy} , the following expression for the NMR signal is obtained:

$$\epsilon(t) = A \cdot \text{Re}(\mathbf{M}_{xy}e^{-i\omega_0 t}). \tag{4.4}$$

Equation 4.4 shows that demodulation of the carrier frequency ω_0 from the FID signal with quadrature phase-sensitive detection (QPSD) yields \mathbf{M}_{xy} . For the remainder of the report it will be assumed that QPSD is used and the Re() operator will be omitted.

In a heterogeneous structure such as the human body, the NMR signal behaviour can vary considerably with position. Following excitation, the transverse magnetization of a small volume element in the body depends on the density of spins and the relaxation rates associated with the type of tissue at that location. The desired MR image is essentially a map of $\mathbf{M}_{xy}(\mathbf{r})$ where the vector \mathbf{r} is used to denote position in the image. Figure 4.3 illustrates how regional differences in T1 and T2 can be exploited to generate contrast in MR images.

Body tissues are largely transparent to RF radiation at typical MRI frequencies, and the RF receive coils used are sensitive to signals originating at different locations within the effective range of the coil. The NMR signal observed following excitation of a heterogeneous region of the body is therefore a superposition of signals originating from throughout the excited volume V. Equation 4.4 can then be re-written as

$$\epsilon(t) = A \cdot e^{-i\omega_0 t} \int_V \mathbf{M}_{xy}(\mathbf{r}) d\mathbf{r}$$
 (4.5)

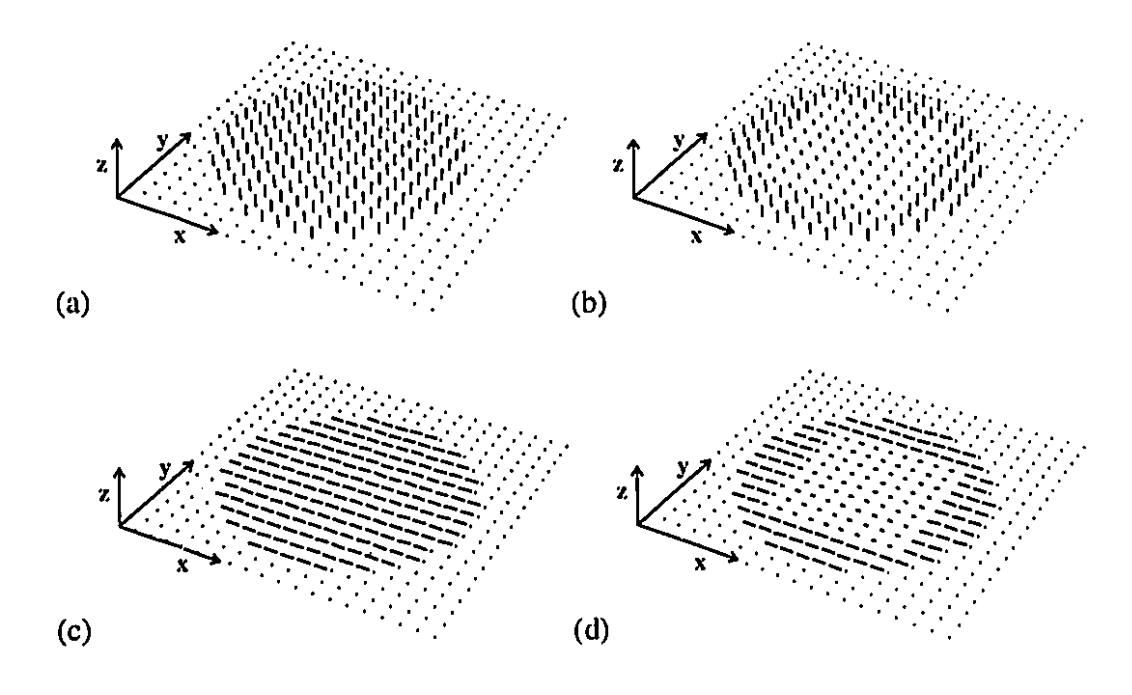


Figure 4.3: Vector magnetization, relaxation, and image contrast; the four vector plots above depict: (a) uniform longitudinal magnetization prior to excitation. Such a distribution may be due to uniformity of T1 values in the object or a long sequence TR, combined with uniform spin density; (b) heterogeneous longitudinal magnetization prior to excitation, providing image contrast to demonstrate the square within the circle. Such heterogeneity may reflect a slower longitudinal relaxation rate R1 (= 1/T1) combined with a short sequence TR, and/or lower spin density in the square; (c) uniform transverse magnetization immediately following 90° pulse applied to distribution in (a); (d) heterogeneous transverse magnetization immediately following excitation of distribution in (a) or after evolution of distribution in (c) over a long TE. Resultant image contrast reveals the square region within the circle.

where it is assumed that the receive coil sensitivity is uniform over the sample or object.

It is not possible to extract $\mathbf{M}_{xy}(\mathbf{r})$ from the FID signal using Equation 4.5. For spatial encoding the gradient coils must be used to manipulate the sample so that $\epsilon(t)$ is related to the Fourier transform of $\mathbf{M}_{xy}(\mathbf{r})$. As discussed in Section 4.2.1, application of a linear field gradient causes the proton resonant frequency to vary linearly with position. A spin at position \mathbf{r} in the presence of a linear gradient \mathbf{G} will therefore experience a shift $\Delta\omega$ in resonant frequency given by

$$\Delta\omega(\mathbf{r}) = \gamma(\mathbf{r} \cdot \mathbf{G}). \tag{4.6}$$

For the purposes of this discussion, both \mathbf{r} and \mathbf{G} can be considered to be twodimensional vectors in the image plane whose origin is at its center. The shift in resonant frequency due to \mathbf{G} at $\mathbf{r} = (0,0)$ is then zero.

The gradient G leads to a phase shift $\Delta \phi(\mathbf{r}, t)$ applied to $\mathbf{M}_{xy}(\mathbf{r})$ in the rotating frame, equal to the integral over time of $\Delta \omega(\mathbf{r}, t)$:

$$\Delta\phi(\mathbf{r},t) = \int_0^t \Delta\omega(\mathbf{r},\tau)d\tau$$
$$= \gamma \left(\mathbf{r} \cdot \int_0^t \mathbf{G}(\tau)d\tau\right). \tag{4.7}$$

Application of the phase shift $\Delta \phi(\mathbf{r}, t)$ to $\mathbf{M}_{xy}(\mathbf{r})$ is equivalent to multiplication by the complex exponential function $e^{-i\Delta \psi(\mathbf{r},t)}$. The signal equation can then be written

$$\epsilon(t) = A \cdot e^{-i\omega_0 t} \int_V \mathbf{M}_{xy}(\mathbf{r}) e^{-i\Delta\phi(\mathbf{r},t)} d\mathbf{r}$$

$$= A \cdot e^{-i\omega_0 t} \int_V \mathbf{M}_{xy}(\mathbf{r}) e^{-i\gamma \left(\mathbf{r} \cdot \int_0^t \mathbf{G}(\tau) d\tau\right)} d\mathbf{r}. \tag{4.8}$$

Demodulating at ω_0 and substituting

$$\mathbf{k}(t) = \frac{\gamma}{2\pi} \int_0^t \mathbf{G}(\tau) d\tau \tag{4.9}$$

into Equation 4.8 allows the signal equation to be written in the following form:

$$\epsilon(t) = A \int_{V} \mathbf{M}_{xy}(\mathbf{r}) e^{-i2\pi(\mathbf{r} \cdot \mathbf{k}(t))} d\mathbf{r}.$$
 (4.10)

This expression is clearly recognizable as the Fourier transform of the complex function $\mathbf{M}_{xy}(\mathbf{r})$. Following demodulation and QPSD the instantaneous value of the function $\epsilon(t)$ represents the Fourier coefficient of $\mathbf{M}_{xy}(\mathbf{r})$ at spatial frequency $\mathbf{k}(t)$. In MR imaging, the spatial frequency domain is often referred to as k-space.

Equation 4.9, which relates the k-space coordinate vector $\mathbf{k}(t)$ to the time integral of the applied gradients, shows that it is possible to sample the 2D Fourier transform of the image slice using appropriate gradient waveforms. Usually the 2D discrete Fourier transform (2D DFT) matrix of the object is filled, with the digitized complex samples from each gradient-modulated FID (or *gradient echo*) providing one row of the matrix. The most common gradient waveforms required to accomplish this are shown in Figure 4.4. Once the 2D DFT matrix is acquired, the complex image can be reconstructed using Fourier inversion. Usually the modulus of the image is then calculated for use in display and analysis. This approach, where samples of the 2D Fourier transform of the object are acquired row by row on a Cartesian grid, is known as *spin-warp* imaging. In single-shot echo-planar imaging, or EPI, the entire 2D DFT matrix is filled using rapidly switched, high amplitude gradient pulses following a single RF excitation.

The number of Fourier-encoded dimensions is not restricted to two. The threedimensional Fourier transform of the excited volume may also be obtained using

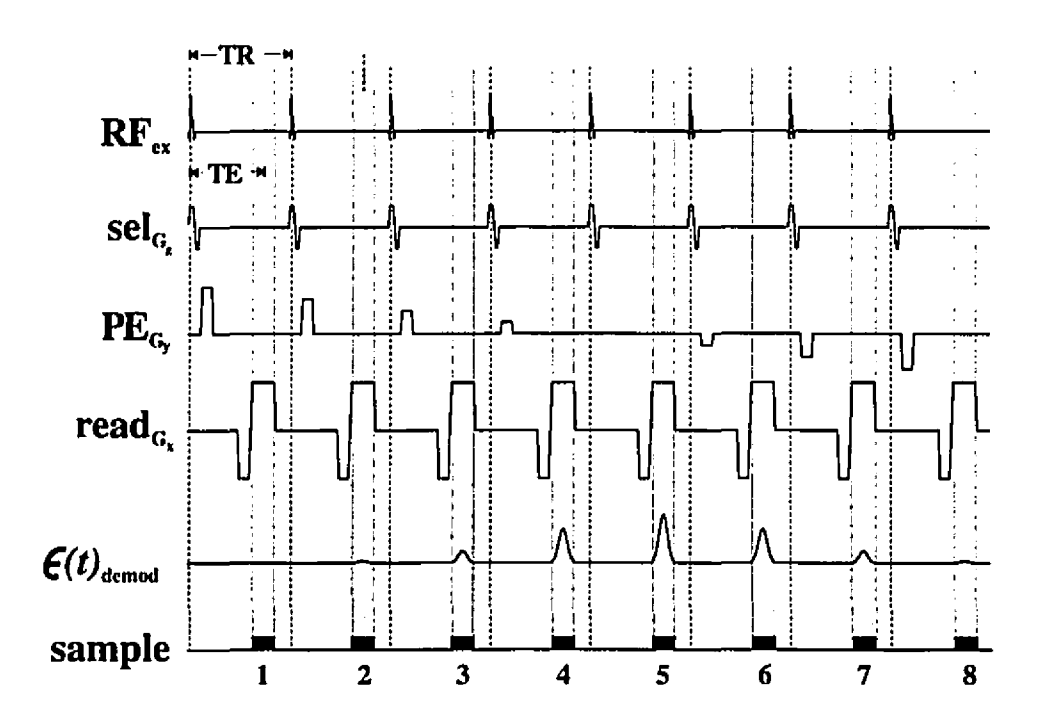


Figure 4.4: Schematic diagram of spin-warp pulse sequence showing RF and gradient waveforms. In this example, eight sequence TRs are shown, during which eight rows of the 2D DFT matrix are acquired. The shaded regions indicate the period in each TR during which the RF receiver is turned on and the demodulated NMR signal $\epsilon(t)$ sampled. The following waveforms are shown: $\mathbf{RF}_{\mathrm{ex}}$: the envelope of the RF excitation pulses; sel_G: the slice selection gradient applied during each excitation pulse. The subscript ' G_z ' is used to indicate that the selection gradient is applied in the z direction in this example; $\mathbf{PE}_{\mathbf{G}_{\mathbf{v}}}$: the phase encode gradient, applied in the y direction in this example. The area under each trapezoidal lobe determines the k_y coordinate associated with the echo observed in the subsequent shaded region; read_{Gx}: the readout gradient applied in the x direction during reception and sampling of the NMR signal. The k_x coordinate of the echo signal is proportional to the time integral of this waveform in each TR. The negative 'pre-phasing' lobe prior to the sampling period initializes the k_x value, which is then scanned through the desired range by the positive lobe while the signal $\epsilon(t)$ is recorded. The set of samples forms one row of the the 2D DFT matrix, whose row index is determined by the area of the preceding PE_{gy} lobe.

an additional phase encoding gradient in the slice direction. Selective excitation is usually still employed to restrict the imaged volume in one direction and thereby eliminate aliasing.

4.2.3 fMRI Sequence Parameters

Using Equations 4.9 and 4.10 it was possible to select sequence parameters suitable for BOLD functional imaging. This section describes a 2D gradient echo sequence that was used as a standard for assessment of the sequences examined in Chapters 5 and 6. Data acquisition was restricted to a single slice in order to keep the acquisition time per image as short as possible. Short scan times were sought as the duration of activation-induced signal changes may be limited. Figure 4.2(b) shows an example of an oblique axial image of a human brain acquired using this sequence.

The minimum scan time achievable was determined by geometric considerations such as field of view and resolution, and contrast requirements which put constraints on the sequence TR that could be used. In order to image an axial cross section of a human head, a field of view (FOV) of about 220 x165 mm was required. Based on the assumption that a spatial resolution of one to two millimeters was sufficient to depict activated structures, a 128 x 96 image matrix was used, yielding 1.7 mm spacing between adjacent pixel centers with the prescribed FOV. In the 2D visual studies performed in this work, a 10 cm diameter receive-only surface coil, placed over the occipital lobe of the subject, was used to increase signal-to-noise ratio. The sensitivity of this coil was not uniform over the nominal field of view, and a fall-off in intensity can be seen towards the front of the head in the images

acquired with this coil (a quadrature head coil, encompassing the entire head, was used to acquire both images shown in Figure 4.2).

Since the 128 x 96 image had to be reconstructed by inverse Fourier transformation of the raw data, a raw data matrix of the same size was required. It was therefore necessary to sample 96 gradient echos, at 128 points each, to produce each image. The time required to perform each gradient echo was then determined according to image contrast requirements.

In order to detect activation-induced changes in blood oxygenation, $T2^*$ weighting was required. For maximum sensitivity to small changes in $T2^*$, the echo time (TE) over which $M_{xy}(\mathbf{r})$ is permitted to evolve following excitation and prior to signal recording should equal the $T2^*$ value of the tissue compartment of interest. This statement is based on the fact that the magnitude of the first derivative of Equation 3.7 with respect to changes in $T2^*$ has a global maximum at $TE = T2^*$.

Application of the above principle of TE selection to our experiments turned out to be impractical, however. The functional signal is assumed to be due to small changes in the T2* of blood and cerebral cortex, and the approximate values of this parameter for blood and grey matter are 100 to 150 ms and 50 to 70 ms, respectively, at 1.5 T[66]. When TE's in this range were used, the non-uniformity of the main magnetic field contributed significantly to spatial variability in the T2* weighted image intensity. The longest usable TE, approximately 45 ms, was used for all studies. Linear B₀ inhomogeneities were eliminated using an automated shimming routine. This increased the signal-to-noise ratio in some studies, but values of TE above 50 ms remained unusable.

In our discussion thus far, the concept of the TE as the point in time at which the FID is sampled has frequently arisen. In Figure 4.4 it is apparent that the gradient

echo must be sampled over a finite time interval to obtain a row of the 2D DFT matrix. The echo time is therefore defined as the time at which $k_x = 0$ during readout, which usually corresponds to the middle of the echo measurement period.

The length of time over which the 128 samples of the gradient echo are measured depends on the amplitude of the measurement gradient and the desired resolution. Since the intended spatial sampling period of our fMRI image is 1.7 mm, spatial frequencies of up to $1/(2\cdot1.7)$ mm = 0.294 mm⁻¹ must be acquired to meet the Nyquist sampling criterion. Equation 4.9 can be used to determine the amplitude and duration of measurement gradient required to achieve this. In the fMRI acquisition described here a relatively long measurement duration of 28 ms was used, allowing a low receiver bandwidth setting of 5 kHz and thereby maximizing the signal-to-noise ratio (SNR). The total sequence repetition time was therefore 63 ms; the sum of the 45 ms echo time, 14 ms for the post-TE half of the FID measurement, and 4 ms to include hardware switching delays and the finite duration of the excitation pulse. Since 96 phase encodes were required, the acquisition time per image was approximately six seconds.

The sequence repetition time in turn influenced the choice of RF flip angle. The interpretation of fMRI data is simplified if the steady state suppression of longitudinal magnetization is minimal and there is little sensitivity to changes in blood flow. The so-called *Ernst angle*, θ_e , above which an increase in flip angle causes a decrease in the signal level, is 22° for a TR of 63 ms for a grey matter T1 of approximately 800 ms. For stationary blood, assuming a T1 of 1200 ms, θ_e is 18°. An RF flip angle of 15° was therefore used to reduce inflow sensitivity. RF spoiling, in which the phase of the RF excitation pulse is systematically varied from TR to TR, was used to suppress the signal from components with long T2, such as

cerebrospinal fluid (CSF)[80]. This was intended to reduce artifacts due to CSF flow.

It should be noted that in spite of the relatively low flip angle and long sequence TR, the sequence parameters described here can be expected to produce considerable saturation of blood and CSF. Equation 3.7 can be used to calculate the percentage suppression of M_0 in the steady state for tissues of a given T1 subject to excitation at a specific flip angle and repetition rate. Assuming a T1 for blood of 1200 ms[66], the longitudinal magnetization of a stationary blood pool would be saturated to 61% of its equilibrium value by 15° pulses applied every 63 ms. Cerebrospinal fluid, with a T1 of approximately 4500 ms[66], would be suppressed to 29% of its equilibrium longitudinal magnetization in such a steady state. Flowing blood and CSF will be saturated to smaller degrees, due to inflow enhancement, and it is likely that there will be some sensitivity to changes in blood flow in the sequence described here. As CSF in a uniformly saturated volumetric image appears dark with the same sequence parameters, the relatively high intensity of the ventricles seen in Figure 4.2(b) can be attributed to inflow enhancement.

The basic sequence described here and employed in this work was similar to that shown in Figure 4.4, with 96 phase encoding steps. The simplified representation in this figure omits two features of the real pulse sequence, however. The first difference is that the integral of the phase encoding gradient is reset to zero at the end of each TR by adding a gradient lobe equal in area but opposite in sign to that performed prior to signal recording. This keeps the net gradient area over, the entire TR constant for each phase encoding step, ensuring stable steady state behaviour in the presence of unwanted echos[74].

The other difference is that in addition to arranging for the zeroth moment of

the readout gradient to be zero at the center of the sampling window, the gradient waveforms were designed so that the first moment was also zero at that point. This practice is referred to as *gradient moment nulling*¹ and it is employed to reduce motion-induced phase dispersion and hence image intensity loss in spins flowing across the applied gradient fields[62].

The first order gradient moment nulling described here can not completely eliminate flow-induced phase dispersion, so some intensity loss will inevitably occur in flowing blood. As the degree of intensity loss will depend on the flow characteristics in a given vessel, it must be recognized that this constitutes an additional form of flow sensitivity that is independent of inflow enhancement and which exerts an attenuating rather than intensifying effect on the MR signal from flowing spins. In practice, stimulus-correlated signal changes are almost always found to be positive. Thus it would appear that flow-induced dephasing is rarely the dominant source of activation-induced MR signal modulation.

Flow-induced dephasing may be more significant than inflow enhancement in vessels whose paths lie within the image plane, since the flowing blood would travel across the imaging gradients and its excitation history would be more similar to that of the surrounding static tissue. In vessels oriented perpendicular to the image plane, the blood is replaced faster and the direction of flow is perpendicular to the readout and phase encoding gradients.

Some investigators have suggested that such flow compensation is undesirable in fMRI sequences as the increased vascular signal levels will lead to greater sensitivity to vascular effects[38]. Both inflow enhancement and flow-induced dephas-

¹also as flow compensation

ing are commonly observed to cause significant, albeit opposite, changes in the MR signal intensity of flowing blood, particularly fast flowing blood in large vessels. The decision to incorporate flow compensation into the 2D sequence used here was based on the fact that such larger vessels are easily identified using MR angiography and on the increasing evidence that intravascular spins are the dominant source of the functional BOLD signal (Section 3.4).

4.2.4 Visual Activation Studies

In order to set basic performance standards of sensitivity, specificity, and image quality, functional studies were performed on healthy volunteers by acquiring T2* sensitive images as described above in rapid succession while the subject was at rest and then during stimulation or performance of a task. Generally, several cycles of rest and activation were included in each dynamic image series. In most experiments stimulation was provided by a pair of goggles with a matrix of red light emitting diodes (LEDs) in each eyepiece (Grass Instruments, USA) which could be made to flash at 8 Hz. Some visual studies were performed using an LCD projector (NEC Electronics) driven by an IBM PC compatible computer to display various patterns to the subject via a mirror mounted in the scanner. Both the goggles and the projector output were synchronized with image acquisition by a PC interfaced to the MR scanner. All MR images were acquired through the calcarine fissure in either a coronal or oblique axial orientation, as shown in Figure 4.5.

Both periodic and pseudo-random activation patterns were used in the various studies performed. For most of the periodic presentations, the task or stimulus state was toggled between the 'off' and 'on' states after every fourth image was ac-

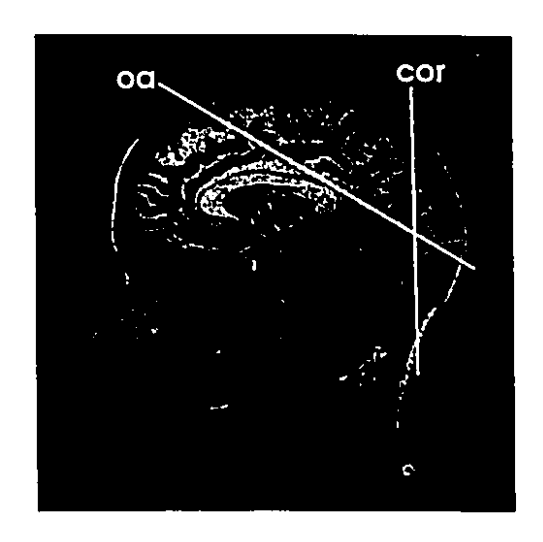


Figure 4.5: Slice orientations used for visual stimulation studies: oa: oblique axial geometry; cor: coronal plane.

quired. This resulted in an eight image cycle which was (typically) repeated eight times for a total of 64 images, or *frames*, per study. The total acquisition time was then 6 minutes, 24 seconds, plus 24 seconds at the start for four 'dummy' scans to reach a steady state of tissue magnetization and gradient eddy current distortion. In the pseudo-random presentation patterns, an aperiodic schedule was used subject to a limit of 30 seconds on the maximum duration of a block of stimulation.

In addition to the T2* weighted image series, T1 weighted volumetric images of the whole brain were acquired in all studies. These images provide a clear structural view of the brain, with high contrast between grey matter, white matter, and cerebrospinal fluid. 3D Fourier encoding was used to produce a whole brain 'volume' with 1 x 1 x 1 mm voxels. The sequence parameters used were TR = 18 ms, TE = 8 ms, and θ = 30° with RF spoiling. Figure 4.2(a) shows a single slice from

such a volume. The spatial coordinates of each voxel are known, so images from different acquisitions can be accurately superimposed or *registered*. This permits the anatomical context of an activation map to be determined.

In some of the studies performed for this thesis, 3D MR angiograms were acquired in order to determine whether activation foci coincided with MR visible blood vessels. The sequence parameters were as follows: TR: 40-47 ms, TE: 6.67 ms, flip angle: 15°. The resolution used varied from 0.8 x 0.8 x 1 mm³ (256 readout samples, 256 phase encodes, 35 3D slices, 2 signal averages, head coil) to 0.33 x 0.33 x 0.6 mm³ (512 readout samples, 1024 phase encodes, 50 3D slices, 1 signal average, surface coil). An off-resonance magnetization transfer prepulse was employed to provide static tissue suppression, reducing dependence on inflow enhancement and improving visualization of small vessels with slow flow velocities[65]. At the highest spatial resolution, it was necessary to use a surface coil to retain acceptable SNR.

4.2.5 Noise Sources

Ideally, regions where the intensity in the T2* weighted frame series changes during stimulus presentation or task execution should correspond to sites of increased metabolic activity. There are other mechanisms which cause intensity variations, however, thereby confounding the identification of truly activated areas. These processes are outlined in this section.

Figure 4.6 shows an example of a coronal T2* weighted image from a 64 image dynamic series acquired during periodic visual stimulation using the Grass goggles and the parameters described above. Time-intensity plots from several voxels

in the image are also shown, demonstrating typical noise and signal levels. Figure 4.7(a) shows an image in which the value at each pixel represents the standard deviation of the intensity in the corresponding voxel over the dynamic series shown in Figure 4.6.

In the absence of any extraneous signal fluctuations, deviation due to activation-induced changes in the tissues would be visible in a standard deviation image as a region of signal fluctuation against a uniform background of zero deviation. Unfortunately, such ideal behaviour is never observed in practice. None of the high intensity regions seen in Figure 4.7(a) are associated with metabolic changes in tissue. Rather, they are due to background physiological fluctuations that bear no useful relationship to the experimental stimulus.

We describe here the most important sources of intensity variation in fMRI acquisitions. These variations constitute background noise against which microvascular BOLD effects must be identified.

Thermal Noise

The uniform background intensity level in Figure 4.7(a) is due to thermal noise picked up by the RF receiving electronics, the most fundamental and inescapable source of intensity variation in MR images. These fluctuations are due to a combination of black body radiation emitted by the subject and Johnson noise generated in the receiver chain. The level of such noise observed in an MR image is proportional to the square root of the RF receiver bandwidth setting, which in turn depends on the desired spatial resolution, field of view, and the amount of time available during the sequence to receive and digitize the RF signal. In conven-

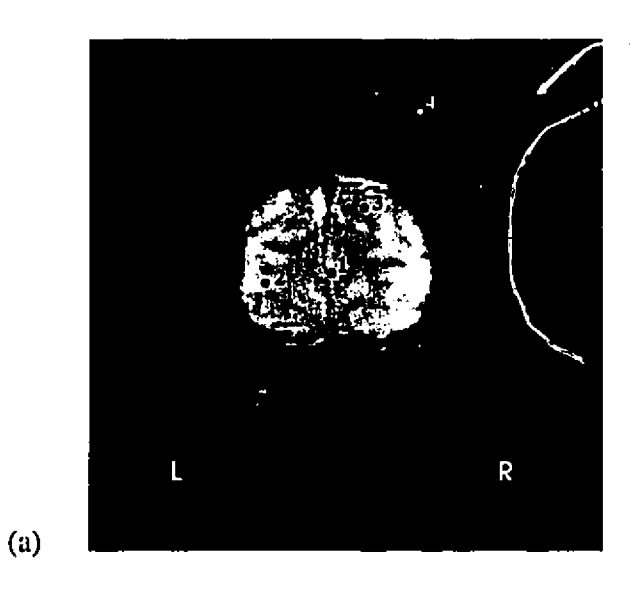
in the image are also shown, demonstrating typical noise and signal levels. Figure 4.7(a) shows an image in which the value at each pixel represents the standard deviation of the intensity in the corresponding voxel over the dynamic series shown in Figure 4.6.

In the absence of any extraneous signal fluctuations, deviation due to activation-induced changes in the tissues would be visible in a standard deviation image as a region of signal fluctuation against a uniform background of zero deviation. Unfortunately, such ideal behaviour is never observed in practice. None of the high intensity regions seen in Figure 4.7(a) are associated with metabolic changes in tissue. Rather, they are due to background physiological fluctuations that bear no useful relationship to the experimental stimulus.

We describe here the most important sources of intensity variation in fMRI acquisitions. These variations constitute background noise against which microvascular BOLD effects must be identified.

Thermal Noise

The uniform background intensity level in Figure 4.7(a) is due to thermal noise picked up by the RF receiving electronics, the most fundamental and inescapable source of intensity variation in MR images. These fluctuations are due to a combination of black body radiation emitted by the subject and Johnson noise generated in the receiver chain. The level of such noise observed in an MR image is proportional to the square root of the RF receiver bandwidth setting, which in turn depends on the desired spatial resolution, field of view, and the amount of time available during the sequence to receive and digitize the RF signal. In conven-



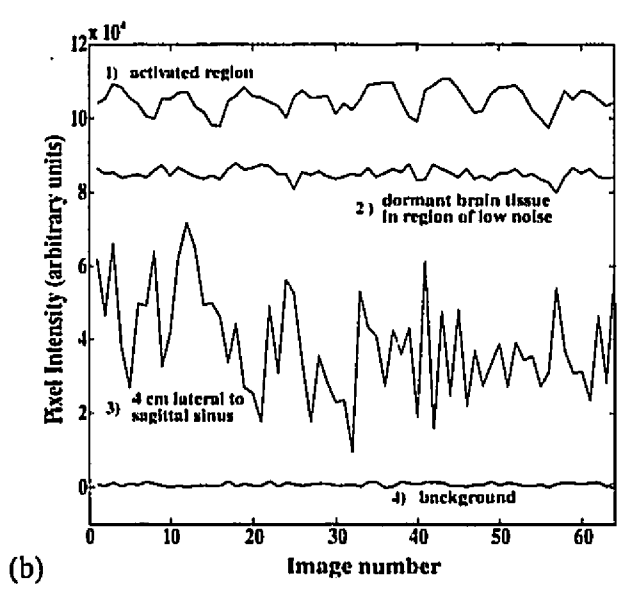


Figure 4.6: Intensity fluctuation in spin-warp images: (a) a single T2* weighted coronal image from a 64 frame dynamic series; (b) time-intensity curves from four pixels in (a), representative of the different noise and activation conditions observed.

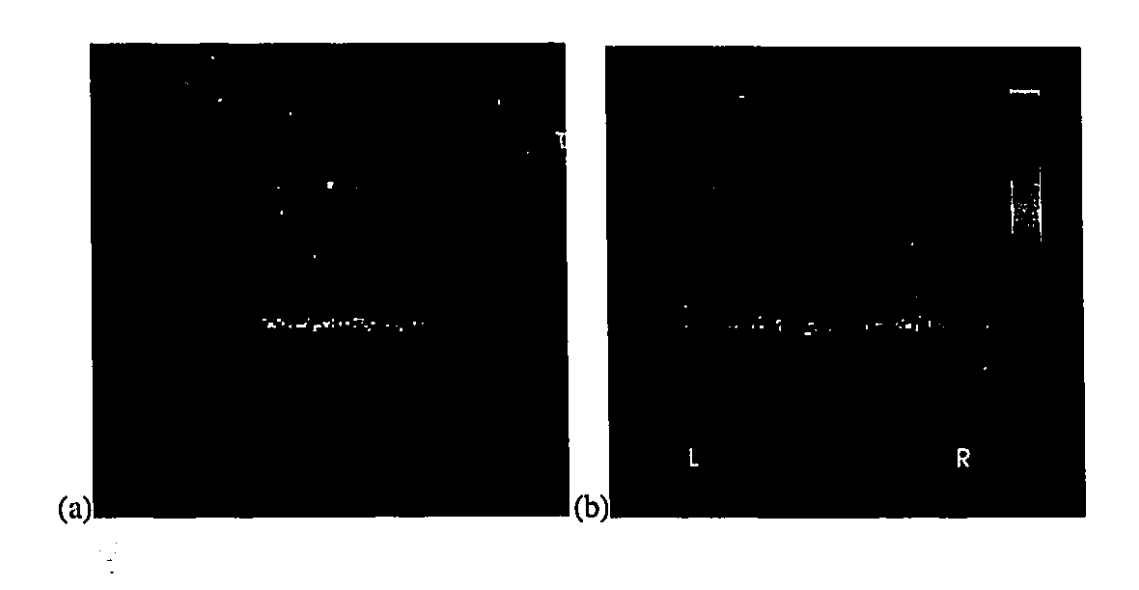


Figure 4.7: Spatial distribution of noise in spin-warp images: (a) standard deviation of the time-intensity series at each pixel of T2* weighted coronal image in Figure 4.6; the high intensity (yellow to red) structures that are replicated from left to right at the top of the head and 'smeared' left to right at the bottom are due to pulsatile flow through the sagittal sinus. The blue rim around the edge of the brain may be due to a combination of subject motion, CSF flow, and brain pulsation. The lower intensity (purple) noise that is smeared outside the head to the left to right but not above or below it may be due to pulsatile flow in the CSF and smaller vessels, and subject motion. The lowest intensity (darker purple) region above and below the head reflects intensity fluctuations due to thermal noise. (b) The standard deviation of each pixel time series expressed as a percentage of its mean value; the intensity in regions to the left or right of the lower sagittal sinus fluctuates by up to 50%. Regions inside the brain generally fluctuate by less than 5%, while at the outside edges this increases to 10%.

tional functional acquisitions, the long echo time used and the limited spatial resolution required permit the use of a low bandwidth (5.0 kHz), and thermal noise is not the dominant source of intensity variations. In single-shot EPI, however, the RF receiver bandwidth and thus the noise level are very high.

The ratio of NMR signal to thermal noise can be increased by enlarging the voxel volume, adjusting the sequence TR and flip angle, and using an RF receive coil which is placed directly against the subject (surface coil). In single-shot EPI the RF signal-to-thermal-noise ratio is better than might be expected because rapidly repeated RF pulses are not required, resulting in less suppression of the steady state longitudinal magnetization. Large (90°) flip angles can be used, resulting in a large amplitude NMR signal.

Thermal noise leads to an approximately Gaussian distribution of the intensity values observed in voxels at all regions of the (modulus) image that have non-zero intensity[58].

Subject Motion

In order to maximize the statistical power of functional studies, data is usually acquired for as long as the subject can comfortably remain very still while paying attention to the experimental stimulus. Experiment durations of five to ten minutes are common, and it is generally accepted that straps and foam padding can be used to restrain a subject's head position to within a few millimeters over such periods. These immobilizing measures were employed for all scans performed in this work.

Despite these measures, motions of distances on the order of a millimeter are

commonly observed in fMRI studies. This can lead to spurious changes in the intensity levels observed in an image voxel over time due to misregistration of images in the dynamic series. The bright fringes at the edge of the brain in Figure 4.7(a) may be due to such motion. These misregistration artifacts can either mimic or mask true activation-induced signal changes in the cortex. Hajnal *et al.* have measured subject motion during visual stimulation studies and found that signal changes due to motion can resemble intrinsic signal changes in the occipital cortex[35].

The motion-induced misregistration artifacts described above are due to motion between different scans. Motion during a single scan can also lead to significant intensity variations in the image. Large, abrupt head movements can cause severe artifacts caused by corruption of the rows of the 2D DFT matrix acquired during the motion. This problem rarely occurs during imaging of the brain, but may occur in functional studies if the experimental stimulus or task is particularly disruptive. The resultant artifacts are easily recognized and the corrupted images may be excluded from the study or the entire experiment can be repeated. Smaller movements can lead to subtle artifacts of the same form which, while not clearly visible on the image, are similar in magnitude to the small activation-induced signal changes that we wish to measure. single-shot EPI is much less susceptible to such artifacts as the data acquisition period is very short compared with the typical duration of such movements.

The effects of gradual shifts in subject position and the resulting image misregistration can be reduced or eliminated by stringent measures to restrict motion. A 'bite bar' mounted on the scanner can be used to hold the subject's jaw and thus their skull in position, and image registration software may be applied retrospectively to correct for subject motion. Navigator echo schemes, in which a portion of the FID is recorded prior to application of any imaging gradients, have been used to correct motion-induced phase shifts in the MRI data. These measures may not always be necessary, depending on the location and strength of the activation-induced signal changes.

In this work, no motion correction post-processing was performed. All dynamic image sets were examined for motion and those in which significant movement could be detected were discarded. The subjective tests for motion applied were 1) displaying the set of dynamic frames in rapid succession as a 'movie'; 2) examination of the standard deviation image; and 3) examination of a modified dynamic series created by subtracting the average of all frames from every frame.

The distribution of intensity values produced at a voxel by such motion is in general not Gaussian, and may be highly variable with position in the image.

Pulsatile Flow

Without question the most prominent features in the standard deviation image shown in Figure 4.7(a) are the bright structures that are replicated or smeared from left to right at the superior and inferior extremities of the brain, and the noisiest curve in Figure 4.6 is recorded from one of these regions. These features are due to pulsatile flow in the sagittal sinus, and illustrate that image voxels containing a significant fraction of flowing blood or cerebrospinal fluid can produce some of the most severe intensity variations seen in spin-warp images.

Each image in the series used to generate Figure 4.7(c) took six seconds to acquire, while the average human heart rate is 60 to 70 beats per minute. The data

used to compute the intensity at any given voxel were therefore gathered during a period spanning about six heart beats. The periodic motion of blood or CSF through the excited volume results in replicated 'ghost' images of the fluid compartment distributed along the phase encoding direction, due to periodic impulsive modulation of the k-space data for those spins². Pulsatile events which occur during acquisition of a low order phase encode (one near the k-space origin) can also lead to the appearance of strong low frequency banding in the phase encoding direction of the image[29].

It is likely that the intensity of any voxel contains some contribution from distant regions of pulsatile flow. The exact location of the replications in an image depends on the phase relationship between the image acquisition sequence and the cardiac cycle, which changes from image to image. The contribution to a voxel's intensity from replication of distant flowing structures will therefore vary over a series of images. This can lead to large fluctuations in the signal level observed in a particular voxel over time. The more diffuse regions of high intensity smeared from left to right outside the brain in Figure 4.7(a) are probably due to a combination of subject motion, CSF flow, and pulsatile flow in small vessels.

Such fluctuations may exhibit temporal structure which can be incidentally correlated with the stimulus presentation pattern of a functional experiment. For example, if it happens that a prominent ghost of the sagittal sinus falls on a certain image voxel more often during stimulation than the baseline condition, the intensity level at that location will appear to be correlated with the experimental stimulus regardless of the physiological status of the tissue in the voxel. This can seriously

²Modulation of a structure's Fourier transform by an impulse train corresponds to convolution with one in the image domain.

confound the results of such studies. Ghosting artifacts from the ventricles, large blood vessels, and densely vascularized regions may cover large clusters of contiguous voxels which, in the case of incidental correlation with stimulation, may lead to large regions of apparent 'activation'. Conversely, a region of true activation may be rendered undetectable if its signal is corrupted by uncorrelated fluctuations of large amplitude from neighboring regions.

The contribution of signal from replicated flowing structures increases with increasing sequence repetition time because more heart beats occur while the 2D DFT matrix is filled. The probability of a pulsatile event occurring during a low order phase encode is increased, and the decreased period of the cardiac modulation in k-space leads to an increased distance between replicated copies of a structure in the reconstructed image. The number of structures which can affect a given voxel is therefore increased[29].

Elimination of intensity fluctuation due to pulsatile flow in the brain is very difficult in spin-warp imaging. The intensity of the artifacts with respect to that of the underlying tissue is generally increased with larger flip angles, so avoidance of these is one way that noise from this source can be limited. In many studies, judicious selection of the slice geometry and direction of the phase encoding gradient allows the ghosting artifacts to be shifted away from the region of interest or even outside of the head. This is demonstrated in Figure 4.7(a) in which the coronal orientation and left-to-right phase encoding direction serve to shift the ghosting artifact away from the anatomy of interest (the calcarine fissure in this visual study) in the center of the brain. An axial slice passing through the same area with anterior-posterior phase encoding would direct the sagittal sinus artifact into the brain over the very region in which we hope to detect the small activation-induced

changes.

Cardiac gating has been explored as a means of ensuring that the arrangement of replicated structures in the image is constant by starting each dynamic image at the same point in the cardiac cycle[17]. This would in principle eliminate changes in intensity over time due to shifting of the replicated structures. Variations in the cardiac cycle limit severely the effectiveness of such schemes, however, and the time resolution achieved is greatly reduced. Image series acquired by interleaved spiral scanning have been found to exhibit considerably greater stability than spinwarp images in the presence of pulsatile motion and flow, in part due to the repeated sampling of the central region of k-space and in part due to the fact that there is no single phase encoding direction in which pulsatility artifact from a given source is concentrated[29]. EPI techniques are almost completely immune to this source of intensity fluctuation, and this is one of their main advantages over spin-warp imaging.

Contradictory observations on the impact of the respiratory cycle on the stability of T2* weighted spin-warp dynamic series have been described. For example Glover *et al.* reported that the respiratory cycle appeared to be much less significant than the cardiac cycle in modulating the phase of the MRI signal[29], while Hu *et al.* found the opposite to be true[38].

As is the case with motion, the distribution of intensity values produced in a voxel by pulsatile flow is in general not Gaussian, and varies greatly at different locations in the image.

Inflow and BOLD Enhancement in Large Vessels

Changes in blood flow rates can cause shifts in the steady state longitudinal magnetization of a voxel, as blood flowing into the image slice from neighboring regions exhibits less saturation, and the amount of flow-induced dephasing may vary depending on the flow rate in a vessel. Flow related phase errors can also lead to an apparent displacement in the position of a vessel in the image. Since the distance that a vessel is shifted depends on the flow velocity, its edge will move as the velocity changes and the image intensity can be modulated in this way. Neuronal activation is known to increase LCBF rates, but blood flow at velocities sufficient for inflow enhancement and flow-induced dephasing or shift occurs primarily in large diameter vessels and not in capillaries. Finally, as mentioned in Section 3.4, Monte Carlo simulations have suggested that activation-induced BOLD signal changes in large vessels are much larger than those expected in microvessels[15].

The neuronal population served by such a large blood vessel lies in a region of unknown, possibly large, size so activation-induced inflow enhancement is difficult to interpret. For this reason flow sensitivity is avoided in fMRI acquisitions by limiting the RF flip angle, using long sequence TR's, and possibly by gradient moment nulling. Centric phase encode ordering (varying the phase encode indices as $0, \pm 1, \pm 2, \ldots$) following inter-scan recovery periods has been used in attempts to reduce inflow sensitivity by obtaining low order phase encodes from magnetization that is close to the equilibrium value[51]. Selective rejection of BOLD signal changes in large vessels has been attempted using diffusion weighted[14] and asymmetric spin echo (ASE)[72] EPI methods.

MR angiography (MRA) techniques exist which permit vasculature to be im-

aged, and their inclusion in functional protocols can help determine whether activation foci coincide with vessels. The spatial resolution of MRA is limited, however, and unresolvable vessels may still contribute to large signal changes.

Figure 4.8 shows an oblique axial fMRI activation map in which the dominant response occurs in blood vessels that are visible in a high resolution MRA (shown here as a maximum intensity projection, or MIP, for clarity). The map shown in this figure corresponds exactly to the T2* weighted image shown in Figure 4.2(b). The anterior end of the vessel on the right side of the central fissure can be discerned in Figure 4.2(b) as a dark line at a 45° angle to the midline, about two centimeters long. It should be noted that the resolution in this MRA is exceptionally high, requiring over 20 minutes of scanning time and the use of a sensitive surface coil to achieve. Angiograms in the same subject with 0.8 mm in-plane resolution failed to resolve the activated vessels visible in Figure 4.8(b).

4.3 Postprocessing of Functional Images

After a series of images is acquired during the various experimental conditions, it is necessary to identify those regions where significant intensity changes have occurred during stimulation. As stated in Section 3.3, the expected signal changes are small, on the order of several percent, and in general will not be visibly discernible.

Another difficulty in statistical analysis of the fMRI signal is that the noise in the time series data for voxels in *in vivo* images is in general not normally distributed. The distribution is generally more complex, changing with time and position, and may not be well characterized by conventional statistical parameters

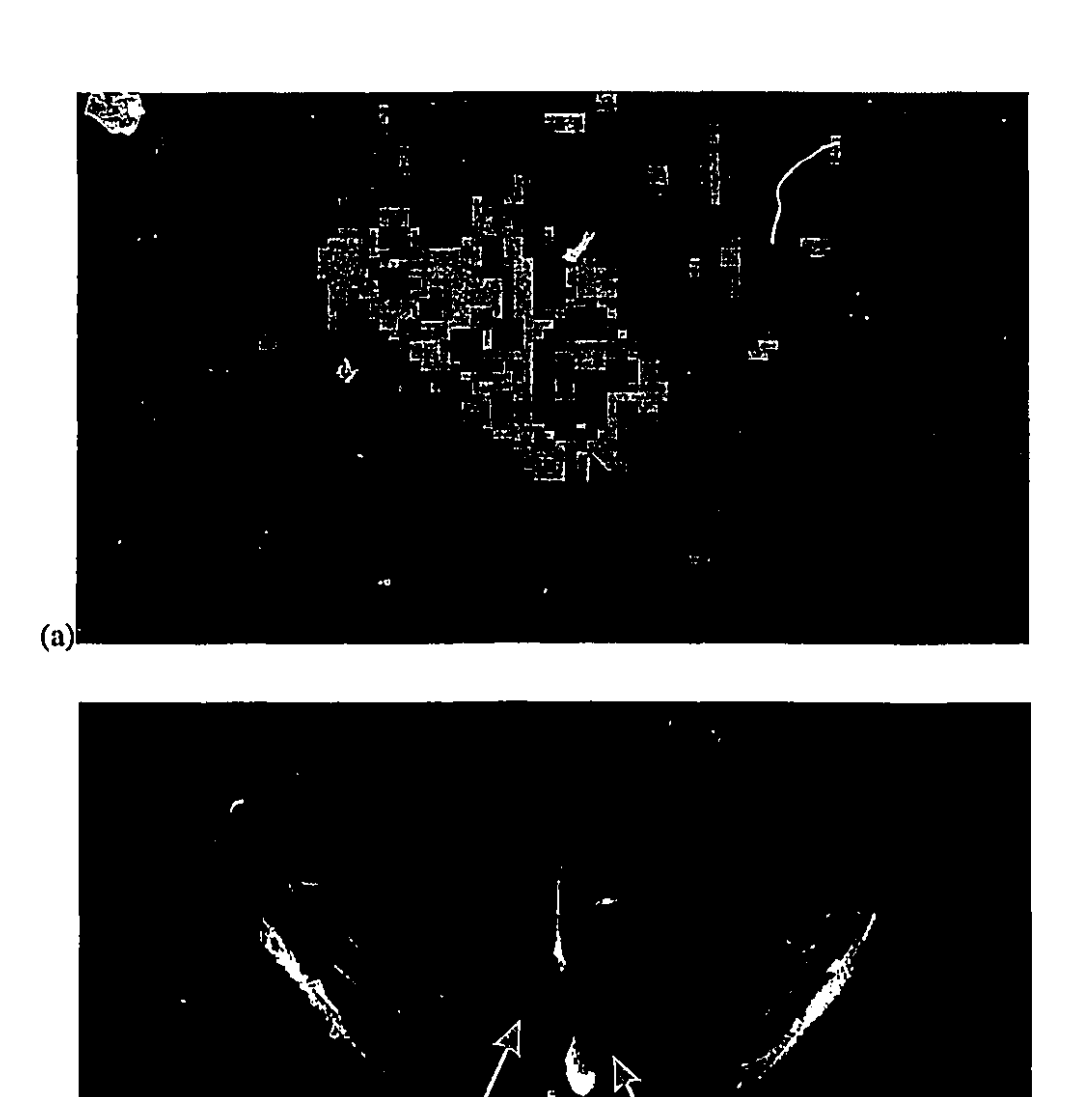


Figure 4.8: Macrovessel response in fMRI studies: (a) unthresholded oblique axial t-map showing activation foci (black arrows) for visual stimulation; (b) oblique axial maximum intensity projection of 3D angiogram showing vessels in same location as activation foci (yellow arrows).

such as mean and standard deviation. This makes it difficult to assign levels of statistical significance to signal changes which occur across different functional states.

A number of techniques have been employed to detect these small activation-induced signal changes, with different advantages and limitations. The goal in each case is the generation of a statistical parametric map, or SPM, which reflects the probability of the observed signal changes occurring in dormant tissue by chance in the presence of noise. The most commonly used methods are outlined here.

4.3.1 Image Subtraction

Simple subtraction of averaged baseline and 'active' images is often performed to provide a direct measure of activation-induced signal changes. In calculating the average images for the dormant and active states, dynamic image frames that were acquired less than ten seconds after initiation or cessation of the stimulation phase should be excluded, due to the finite time apparently required for the BOLD signal to reach a new steady state. While the magnitude of the observed response is an important physiological parameter, this approach is limited in that it does not permit assessment of the statistical significance of the changes.

4.3.2 Student's t-test

Student's t-test for statistical significance can be performed if the distribution of image intensity values has the same shape during the baseline and activated phases, and if that distribution shape is suited to characterization by the mean and standard deviation parameters [67]. However, in spin-warp imaging, the intensity distribu-

tions may not meet these requirements[5]. As with image subtraction, it is probably appropriate to discard intensity measurements acquired within 10 seconds of stimulus onset or cessation.

4.3.3 Linear Correlation

The coefficient of linear correlation, r, between pixel intensity and the applied stimulus level was first described by Peter Bandettini $et\ al$. as a useful means of locating regions of stimulus-correlated signal change in fMRI[7]. The principle is similar to the t-test in that a measure of the difference in average intensity across states is normalized to a measure of signal variance, but intensity values measured during transitional periods can be appropriately weighted when calculating the averages. The advantage of this technique is that it allows identification of regions where the temporal response matches an arbitrarily specified waveform shape. This attribute is also somewhat of a drawback, however, as the response waveform may vary considerably for different experimental paradigms and is, in general, not precisely known.

A further limitation is that the linear correlation coefficient is not a robust measure of statistical significance. If the pixel intensity values and the stimulus level values jointly form a binormal distribution around their mean values, then r may be transformed into a form that is distributed approximately as Student's t statistic, permitting assessment of statistical significance[67]. It is not usually possible to modulate experimental stimuli in such a way that this requirement is met, however, and the use of linear correlation is thus limited.

4.3.4 Rank Correlation

If rank correlation measures such as the Spearman rank-order correlation (SROC) coefficient r_s are used, the transformed statistic

$$t = r_s \sqrt{\frac{N-2}{1-r_s^2}} \tag{4.11}$$

is distributed approximately as Student's distribution with N-2 degrees of freedom, where N is the number of points in the time-series data[67]. This is true regardless of the distributions of pixel intensity and stimulus level values—an important advantage over linear correlation. A response waveform shape must still be specified, but the exact shape is less crucial, as only the ranks of the waveform sample values will be used in the analysis.

4.3.5 Kolmogorov-Smirnov Test

The Kolmogorov-Smirnov (KS) D statistic is another measure which is appropriate when the distributions of pixel intensity values in the baseline and activated states are variable or unknown. It also has the advantage that no assumptions need to be made regarding the shape of the response waveform. The D statistic is the maximum value of the absolute difference between two cumulative distribution functions, in this case the distributions of pixel intensity values in the baseline and activated states[67]. The distribution of the D statistic for identical distributions is well characterized, so the significance of any non-zero value of D is readily calculated.

4.3.6 Summary of Data Analysis Issues

Determination of the 'best' statistical test for fMRI data is outside the scope of this thesis. The descriptions given in the previous sections were included in order to illustrate the difficulties presented by the complicated noise sources encountered in fMRI. Furthermore, the techniques described above all produce *qualitatively* similar SPM's. This is illustrated in Figure 4.9, which shows oblique axial maps generated using different techniques applied to the same visual stimulation data. The *l*-test and subtraction maps show less contrast in the activated region, possibly due to the inclusion of images acquired immediately following the beginning and end of stimulation periods. These SPM's are included only to show the similar ratios of contrast to background noise achieved with the same linear spectral color code; consequently, color legends are not shown³. The spectral color code was chosen for the display of standard deviation images and SPM's in this thesis because of its superior depiction of low contrast structures and for consistency with PET activation studies performed at the MNI.

The primary difficulty in applying the statistical tests described above lies in determining levels of statistical significance in the presence of non-normal measurement errors. Monte-Carlo simulations using large numbers of null data sets (image sets acquired with no stimulus modulation) can be used to characterize the distributions of the different statistics used to detect change, but this is computationally intensive and results for a given subject and image geometry may not apply

³The rank ordering of intensity values implied by the spectral color scale is the same in all images shown in this thesis, so color legends are only included when it is desired to communicate the numerical value of image intensity levels.

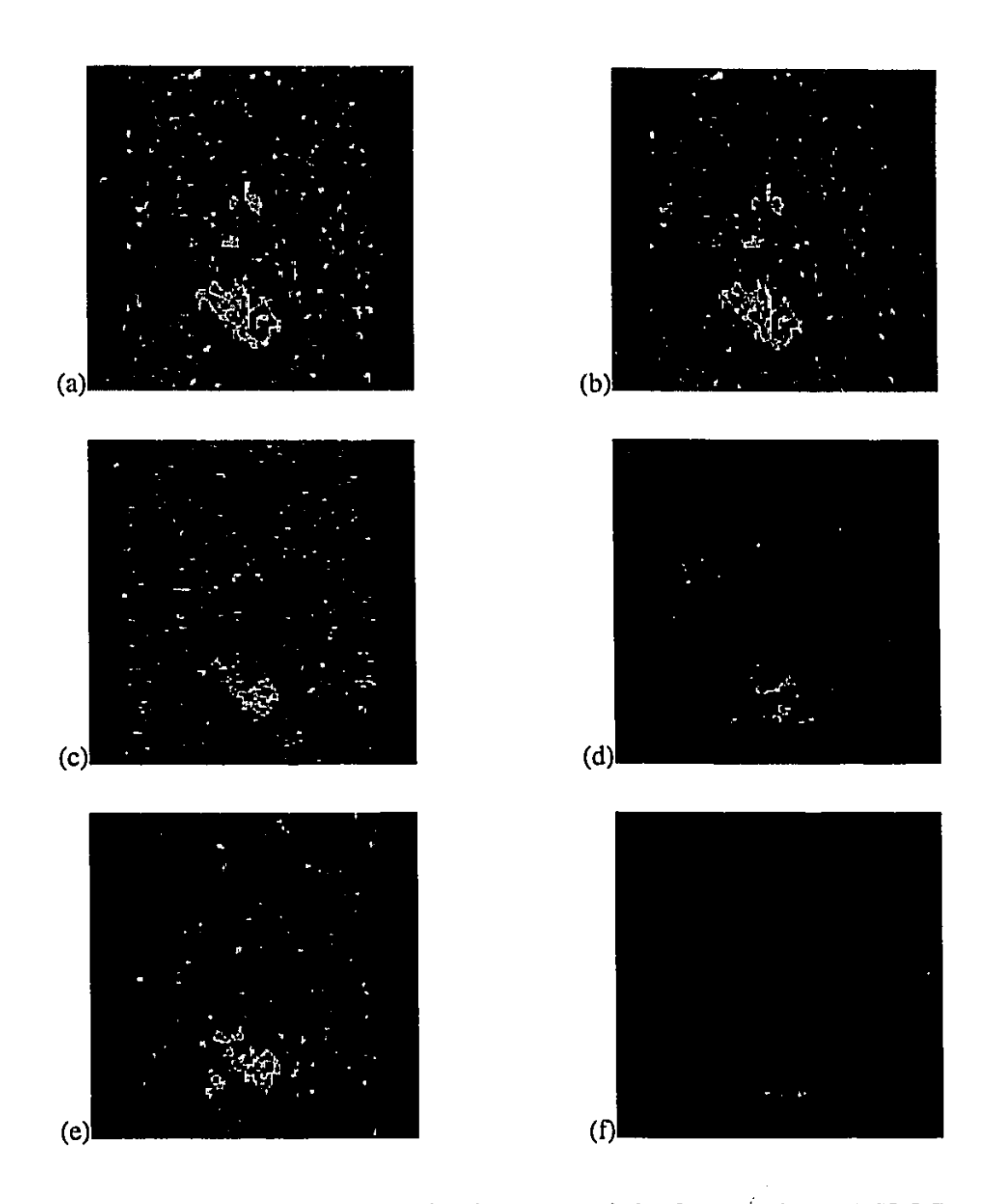


Figure 4.9: Oblique axial maps of various test statistics for same data: (a) SROC derived t-map; (b) linear correlation coefficient r; (c) conventional t-test; (d) subtraction image; (e) Kolmogorov-Smirnov D map; (f) standard deviation image.

to other studies.

An additional problem in the statistical analysis of fMRI data is that of setting significance criteria for activated regions as opposed to individual voxels, in the presence of intrinsic spatial autocorrelations⁴. Worsley $et\ al$. have addressed this problem in the context of PET activation studies[77], and their approach has been adapted for functional MR imaging by Friston[26]. The thresholded SPM's presented in this work were not corrected for multiple non-independent comparisons, and will therefore be referred to as 'descriptive' SPM's. A one-tailed threshold of P=0.001 is usually recommended for such uncorrected maps[26], and was therefore incorporated into the analysis performed here.

A further difficulty in the interpretation of fMRI SPM's becomes apparent upon inspection of the spatial variation in noise level visible in Figure 4.7(a). Practically all statistical tests measure significance by comparing a change in some quantity to the magnitude of its measurement errors or noise level. The large spatial variation in noise level in spin-warp fMRI image series leads to highly spatially variant sensitivity to functional changes. An activation-induced change in image intensity of five percent may give rise to a test statistic well above the significance threshold in an area of low noise, but in a region where the background fluctuations are 20% of the mean signal level, the same five percent change will appear totally insignificant. It is therefore important to plan every study by acquiring null data sets and examining the standard deviation images to ensure that the anatomical site of interest is in a region of uniformly low noise level. Figure 4.10 shows a flowchart summarizing the interpretation of fMRI statistical test results.

⁴This is often referred to as 'the problem of multiple non-independent comparisons'.

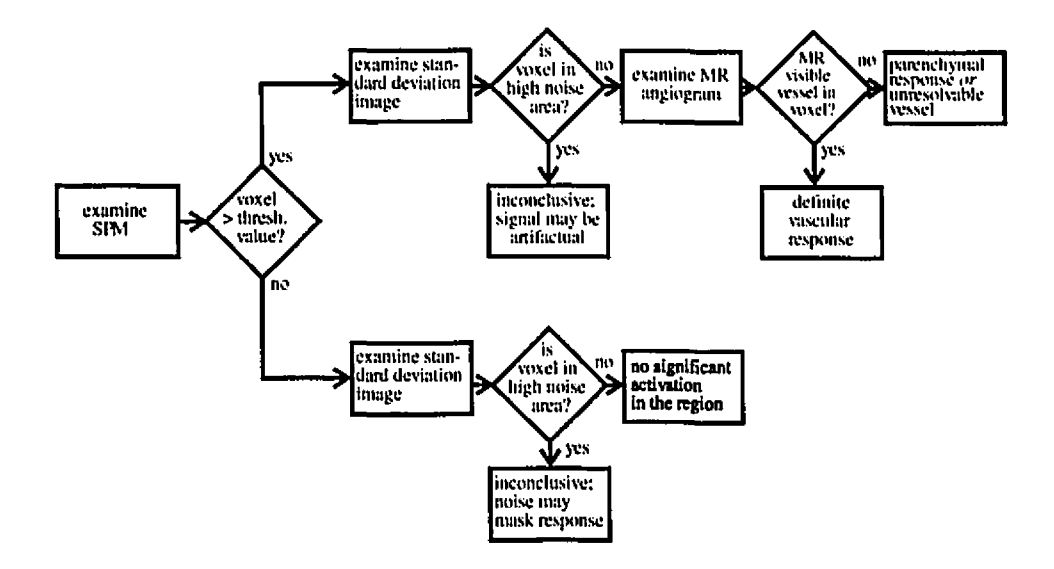


Figure 4.10: Flowchart summarizing interpretation of fMRI statistical test results.

For consistency, all SPM's (other than those in Figure 4.9) shown in this thesis are t-maps based on transformation of the Spearman rank-order correlation statistic, r_s as described above. The reference waveform used consisted of zeros during baseline images and ones for images acquired during the activated state, with the exception of those acquired during transition periods (i.e. immediately following stimulus onset or cessation), which were assigned a value of 0.5.

Unless otherwise stated, the 2D SPM's displayed in this thesis have been filtered with a Gaussian kernel with a full width at half maximum (FWHM) of 2 pixels (normalized to unit volume), to suppress high spatial frequency noise. This resulted in a slight broadening of activation foci and a concomitant reduction in peak amplitude. The imposition of this additional degree of autocorrelation between voxel t values further complicates the statistical interpretation of the results.

It must therefore be emphasized that the thresholded SPM's generated under these conditions must be considered to be qualitative.

Thresholds for the filtered maps were chosen in the following way: unfiltered t-maps were subjected to a threshold t_{min_1} corresponding to the recommended P value of 0.001 for N-2 degrees of freedom, where N was the number of images in each dynamic series. Next, the filtered maps were displayed and a new threshold t_{min_2} was chosen so that the same regions would pass in the filtered image. For the studies performed here, a threshold of $t \geq 3.0$ was found to be appropriate for the filtered maps.

To show the effect of this spatial filtering, Figure 4.11 shows the SROC derived t-map previously used as an example in Figure 4.8 with and without spatial filtering. The suppression of peak values in the blurred map is clearly demonstrated in this figure, which uses the same color scale to depict the voxel t values in both images. In Figure 4.8, the two foci seen in these images were shown to correspond to two very small diameter blood vessels visible in an MR angiogram. The shapes of the foci in the unfiltered map are more consistent with their small vascular origin, whereas in the blurred map the width of the structures matches the width of the cortex more closely. This effect must be kept in mind when examining such processed SPM's.

4.3.7 Analysis Software

A number of software tools for the analysis of fMRI data sets were developed in the course of this thesis. These were implemented in Matlab (The MathWorks, Inc.) and run on an SGI Indy workstation.

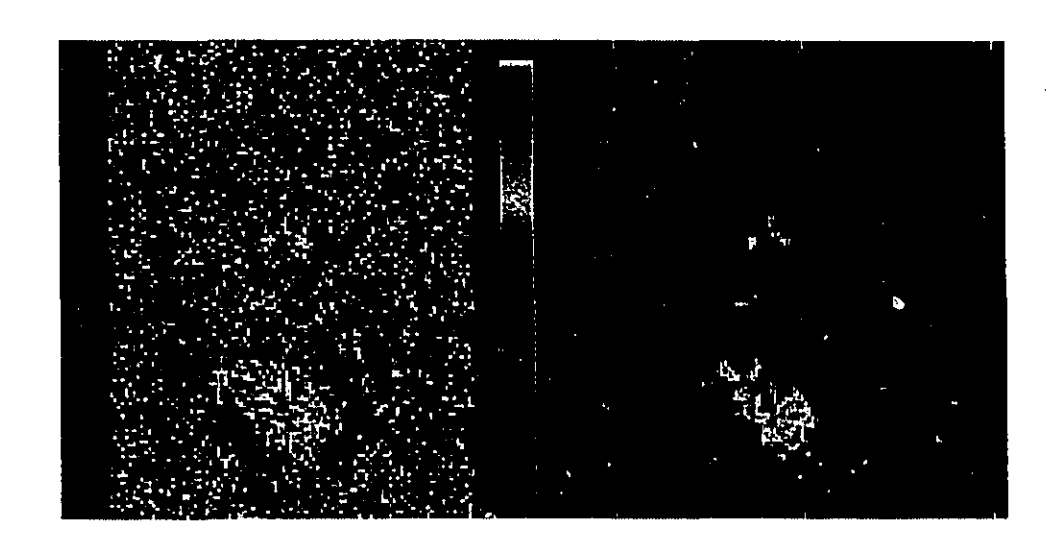


Figure 4.11: Effects of spatial filtering on SPM. Left: Unfiltered oblique axial t-map from visual stimulation study; Right: Same map after low pass spatial filtering with 2 pixel FWHM Gaussian filter normalized to unit volume (same color scale). In the filtered map the background noise is smoothed but the peak amplitude of the test statistic is reduced at the activation foci and they are broadened.

Images acquired on the Philips Gyroscan ACS-2 MR scanner were transferred via an ethernet connection to a local network of SGI's on which analysis was performed. During data transfer, the MR images were converted from Philips' native format to the MINC⁵ file format, the local standard recognized by most image analysis software in use at the MNI[57]. The EMMA package, a locally developed Matlab function library for manipulation of image data in the MINC format, was used to read and write image data files from within Matlab.

All analysis tools were implemented as functions that could be invoked from the Matlab command line, passing input/output file names and other parameters as input arguments and returning results as function values and, if requested, MINC output files. Comprehensive online help text was written for all functions. The following is an abbreviated list of analysis tools implemented as Matlab functions:

Statistical Tests:

- linear_corr(): Reads in user-specified reference waveform, dynamic image series, and calculates the linear correlation statistic r at each voxel.
 Outputs r-map.
- spearman (): Reads in user-specified reference waveform, dynamic image series, and calculates the SROC statistic r_s at each voxel. Outputs t-map based on transformation of r_s statistic.
- subtract(): Reads in dynamic image series, and calculates averaged subtraction image based on user-input flags indicating stimulated, baseline,

⁵Medical Image Network Common Data Form

and transition periods. Outputs difference image.

- t_test(): Reads in dynamic image series, and calculates t values for each voxel based on user-input flags indicating stimulated, baseline, and transition periods. Outputs t-map.
- ks_test(): Reads in dynamic image series and calculates Kolmogorov-Smirnov D statistic for each voxel based on user-input flags indicating stimulated and baseline periods. Outputs D map, and map of corresponding P values.

Each function can output its associated SPM, both with and without low-pass filtering, as described above. Either 2D or 3D image sets can be input, and the output can be directed to a MINC image file.

Other Tools:

- gen_tic(): Interactive tool for capturing time-intensity curves from dynamic image series. Using any desired transformation of a dynamic image series (SPM, standard deviation image), points may be selected with the mouse pointer and the corresponding time-intensity curve is displayed. The user can select the number of pixels used for the ROI, and filtering parameters for the time-series data.
- stdv_image(): Reads in a dynamic image series and outputs an image in which each voxel intensity value is the standard deviation of the corresponding time series. Also output is an image in which the voxel intensity

is the standard deviation expressed as percentage of the mean signal in that voxel.

• sub_mean (): Reads in a dynamic image series, and subtracts average intensity value of each voxel from that voxel in each dynamic frame.

Other locally developed software, notably the SGI Graphics Language programs register and Display[49], were used to display superimposed functional and anatomic images and perform cortical surface extractions.

4.4 Discussion

Stimulus-correlated changes in T2* weighted MRI signals have been observed using the 2D gradient echo sequence described in Section 4.2.3. Despite the difficulties in performing rigorous statistical analysis of these data, the contrast-to-noise ratio of the calculated statistical maps, as illustrated in Figure 4.9, appears sufficient for the qualitative localization of activation foci.

The primary goal in this research was the development of rapid imaging techniques with the highest ratio of T2* to inflow sensitivity achievable given existing hardware constraints. A detailed analysis of the physiological significance of the activation foci observed is outside of the scope of the thesis; however, the observation that activated regions appear to coincide with small blood vessels visible in high resolution MR angiograms bears brief mention.

A more complete three-dimensional view of the relationship between the activated region and the surrounding vasculature might help answer several interesting questions:

- Is the vessel morphology consistent with that of a vein or with that of an artery?
- What is the level of activation in the vessel at various points along its length?
 Why does it vary?
- What cortical regions appear to be served by the vessel?
- Are there other nearby vessels and do they exhibit stimulus-correlated signal changes?
- Where does the vessel branch—do all of the ramifications appear to be activated or only some?

In the next chapter a 3D fMRI acquisition is examined and its ability to help answer some of the above questions is demonstrated.

Chapter 5

Echo Shifted 3D fMRI

5.1 Introduction

In Chapter 4 it was demonstrated that the response to visual stimulation with LED matrix goggles could be detected using a conventional 2D gradient echo sequence. Ideally, one would like to obtain 3D maps of the whole brain at high isotropic resolution. Given the current uncertainty as to the exact physiological significance of fMRI activation foci, the ability to study the correlation of these regions with vascular and cortical anatomy in three dimensions would be a major advantage.

Three-dimensional fMRI has proven difficult for a number of reasons, however. In the first part of this chapter various approaches to volumetric MRI are reviewed and their suitability for functional imaging assessed. Next, a 3D fMRI acquisition based on Moonen's echo shifting technique[48, 56] is described and demonstrated in a visual stimulation study. Finally, methods for the display of 3D fMRI activation maps are discussed.

5.1.1 Review of Multi-Slice MRI Methods

A variety of approaches for acquiring multiple slice MR images is available, and in principle any of these could be used to acquire dynamic series for functional imaging. The spatial and temporal characteristics of image series produced by the different methods can vary considerably, however, and the choice of technique must be made with care. The different alternatives are listed below, along with descriptions of the properties relevant for functional imaging.

Repeated 2D Studies (R2D)

The simplest way to examine multiple slices of the brain is to perform repeated 2D acquisitions, incrementing the position of the slice each time, to generate a dynamic series for each location. The main drawback of this approach to functional imaging is that the total exam time becomes long, and the data in different slices represent the response at widely separated points in time. It is therefore necessary to ensure that the physiological response pattern does not vary significantly over the total study duration and for some experimental paradigms, such as memory or learning tasks, this may not be the case. If the 2D acquisition and 64 frame protocol used in this work were repeated to study multiple slices, the total exam time would be a multiple of the 6 minute 24 second period needed to acquire a dynamic series for a single slice, plus any rest periods in between the slices.

Two-dimensional dynamic studies can be expected to exhibit maximal sensitivity to inflow enhancement for a given TR and flip angle, as blood flowing into the slice from surrounding regions will have 100% of its equilibrium longitudinal magnetization. Another problem associated with selective excitation of a single

slice is that subject motion which includes a component in the direction of selective excitation can lead to disruption of the steady state of the longitudinal magnetization. This occurs because previously unexcited spins are displaced into the image 'slab' defined by the selection gradient and RF excitation bandwidth, thereby inducing large amplitude intensity fluctuations.

If only a few slices are needed and the pattern of the physiological response is not expected to change significantly with time, this approach offers considerable flexibility in the choice of sequence parameters, as these are completely independent of the number of slices acquired.

Interleaved Multi-Slice (IMS)

Inspection of the pulse sequence timing diagram in Figure 4.4 reveals periods of unused time during each sequence repetition block. If the TR is long enough, this time can be used to selectively excite and record the signal from additional slices. Sequence repetition times considerably longer than the 63 ms described in Chapter 4 are required, however, and this has several implications for functional imaging. Inflow sensitivity is reduced, but signal fluctuations due to pulsatile flow and motion are increased[29] and temporal resolution is lowered. For inner slices the sensitivity to inflow enhancement is further reduced because the blood flowing in from the surrounding slices has already been excitated.

When inherently 2D approaches such as IMS are used, the individual image slices are reconstructed independently of each other by Fourier inversion of their 2D DFT matrices. Any artifactual signal fluctuation which occurs is therefore confined to the slice in which it originates. In functional MRI this can lead to reduced

continuity between slices in the volumetric statistical maps, making it difficult to visualize activated regions in three dimensions.

Multiple 2D (M2D)

Rather than interleaving measurements for multiple slice image sets, the slices may be imaged in a serial fashion. In an M2D scan the various slices are imaged one after the other until the entire volume is covered, then the process is repeated for the next dynamic frame. This is the opposite of the R2D approach described above, as here the slice loop is inside the dynamic scan loop. Unlike the IMS method, M2D scans do not require an extended TR. The temporal resolution and therefore the amount of data acquired per slice in a constant exam time are reduced in proportion to the number of slices imaged, however, and the longitudinal magnetization in a given slice must re-establish a steady state for each dynamic frame. This can lead to image intensity fluctuations due to oscillation of the magnetization during reequilibration.

As in interleaved multi-slice imaging, artifacts are confined to individual slices and discontinuities in reformatted activation maps may be observed along the axis of selective excitation. The use of single-shot EPI to acquire multiple slices is analogous to M2D spin-warp imaging, with the attendant sensitivity to motion in the slice direction. The long TR's and single excitation pulse used in EPI preclude the steady state problems of M2D, however.

3D Fourier Encoding (3D)

As mentioned in Section 4.2.2, phase encoding gradient waveforms can be applied in the slice direction to provide an additional dimension of intra-slice spatial encoding. Typically the volume of interest is selectively excited, samples of the three-dimensional Fourier transform are acquired, and the image is then reconstructed by 3D Fourier inversion. This approach has several advantages over the 2D approaches described above.

One desirable property of 3D acquisition is that extending the image volume by increasing the number of Fourier-encoded slices enhances the ratio of signal to thermal noise in each individual slice. Each extra phase encode constitutes an additional signal average for all slices so, for example, obtaining 16 slices would increase the RF SNR by a factor of four¹ above that achieved for an identical single slice acquisition. The increased signal-to-noise ratio permits the use of smaller voxel volumes than those required with 2D Fourier encoding, making isotropic resolution easier to achieve without unduly large voxels. The large voxel volume (45 mm³) of the 3D acquisition described here is necessary due to time constraints, and provides considerable SNR enhancement above the 21 mm³ voxel volume of the previously described 2D protocol.

Another advantage of the 3D Fourier technique is that motion in the slice direction, while still problematic, does not lead to as severe a disruption of the steady state longitudinal magnetization as that seen in 2D methods.

Furthermore, as the image volume is increased, signal changes due to inflow

 $^{^{1}}$ RF SNR \propto (Number of Signal Averages) $^{\frac{1}{2}}$, due to the white Gaussian nature of this noise source.

enhancement become less significant because the excitation history of blood in the image volume more closely resembles that of the surrounding static tissue. Flow-induced dephasing can still occur, but gradient moment nulling reduces the effect.

The images generated by 3D Fourier inversion have a more isotropic impulse response than those obtained via 2D Fourier inversion of individual slices, without the intensity discontinuities often observed at the slice boundaries in MS and especially M2D images. Retrospective motion correction techniques, which estimate motion and resample images in a dynamic series to align them, perform better with true 3D data sets[36].

The primary drawback of 3D techniques for fMRI is the increased acquisition time usually required. In order to achieve acceptable image quality, a minimum number of phase encodes in both the in-plane and slice directions must be performed, resulting in a lower limit on scan time if a long TE is to be maintained as is necessary for BOLD contrast studies.

If motion and other physiological sources of signal fluctuation could be completely eliminated, and if it was certain that activation-induced signal changes would persist indefinitely during presentation of the experimental stimulus, then short scan times would not be essential. Under such conditions (assuming the ratio of contrast to thermal noise is sufficient) it would be possible to acquire one or more 3D images in both the baseline and stimulated states and identify activated regions by performing the appropriate comparisons. In practice this approach rarely works, due to subject motion and, in some cases, decline in the functional signal over time due to metabolic re-equilibration and/or loss of subject attention.

5.2 Methods

Based on the desireable properties of 3D Fourier encoding, it was decided that this approach would be investigated for volumetric functional imaging. Through experimentation, it was established that acceptable 3D image quality was obtained when the 2D acquisition previously used was modified to include 7 and 64 phase encodes in the slice and in-plane directions respectively, with voxel dimensions of 3 x 3 x 5 mm. The acquisition time per frame was thereby increased to approximately 22 seconds. This is less than $64 \times 7 \times 7$ TR by about 21% because only phase encodes within a cylindrical volume of k-space need to be acquired, leading to a reduction of scan time by a factor of $\pi/4$.

In order to reliably detect activation-induced signal changes, it appears that the acquisition time per image must be short compared to the time scale over which subject motion and changes in the functional signal occur. Since the BOLD signal is subject to a rise time of approximately 10 seconds[43], and in order to limit the effects of intra-scan motion, a reduction in scan time below the 22 seconds required for a conventional 3D acquisition was desired. The echo shifting (ES) technique introduced by Moonen *et al.*[48, 56] was employed to achieve this, lowering the scan time to 11 seconds while retaining a long effective echo time of 48 ms. Duyn *et al.* have reported the use of this technique to perform 16 slice 3D acquisitions in 20 seconds, with similar spatial resolution and a shorter effective echo time of 30 ms[20].

In Moonen's original implementation of the echo-shifted sequence, additional gradient lobes of alternating polarity were added following each RF excitation pulse as shown in Figure 5.1. These gradients served to dephase transverse magnetiza-

tion generated by the immediately preceding excitation pulse, so that it would not contribute to the echo observed in the subsequent TR. These extra gradients would also refocus magnetization generated and dephased in the previous block, giving rise to the magnetization actually observed during any given TR. It is also possible to modify the gradient waveforms shown in Figure 5.1 to shift the observed echo by more than one TR[48].

With such an arrangement the transverse magnetization generated by a given RF excitation is exposed to one or more later pulses before it is sampled, resulting in a small reduction in the strength of the observed signal. In a report by Liu *et al.*, coherence pathway formalism was used to describe the effect of the intervening RF pulses on previously generated magnetization in ES sequences[48]. It was determined that the transverse magnetization generated in a given TR is decreased by a factor of $\cos^{2n}(\theta/2)$ when exposed to excitation pulses of flip angle θ in n subsequent TR's. For example, a flip angle of 10° and a shift of one TR would reduce previously existing transverse magnetization by 3%, which can easily be tolerated.

If the areas of the spoiler gradients are sufficient, there will be complete dephasing of all transverse magnetization at the end of each sequence TR and the amplitude of the NMR signal in an ES sequence behaves as described by Equation 3.7 with an additional factor of $\cos^{2n}(\theta/2)$:

$$M_{xy} = M_0 e^{-(\text{TE} + n\text{TR})/\text{T2}^*} \sin(\theta) \cos^{2n}(\theta/2) \frac{1 - e^{-\text{TR}/\text{T1}}}{1 - \cos(\theta)e^{-\text{TR}/\text{T1}}}$$
(5.1)

where n is the number of TR's by which the echo is shifted and the rest of the variables are as defined for Equation 3.7. Note that in the above equation TE is taken to be the amount of time separating the centre of each excitation pulse and the immediately following readout window, as usual. In the remainder of this chapter,

the term *effective echo time* will be used to describe the true period over which transverse magnetization evolves prior to recording.

When such spoiling and refocusing are performed, the effective echo time actually exceeds the sequence repetition time. The long echo times needed for T2* contrast can thus be retained, while allowing a given number of phase encodes to be acquired in half the time, or less, required with a standard sequence. Although shifting the echo by more than one sequence repetition block permits a greater reduction in scan time for a given effective echo time, the shorter TR leads to a rise in the sensitivity to inflow enhancement and the signal-to-noise ratio is further decreased due to the saturation effects and the higher digitizer sampling rates required.

Echo shifting by one TR was therefore performed, permitting T2* weighted 3D images to be acquired in 11 seconds by reducing the sequence TR to 33 ms and recording each echo 15 ms into its second repetition block. This made the effective echo time 48 ms. The flip angle was decreased from 15° to 10° in order to reduce inflow sensitivity at the shorter repetition time and to minimize rotation of spoiled transverse magnetization prior to echo detection. Substitution of the new flip angle and sequence TR into Equation 5.1 reveals that the steady state magnetization of stationary blood would be suppressed to 63% of its equilibrium level. This represents slightly *less* saturation than the value of 61% determined for the 2D acquisition parameters. The reduction in transverse magnetization incurred from exposure to the single intervening RF pulse of 10° flip angle was 3% as explained above.

The ES sequence used for this work was programmed on our 1.5 T system using the GOAL-C language supplied by Philips Medical Systems. In this imple-

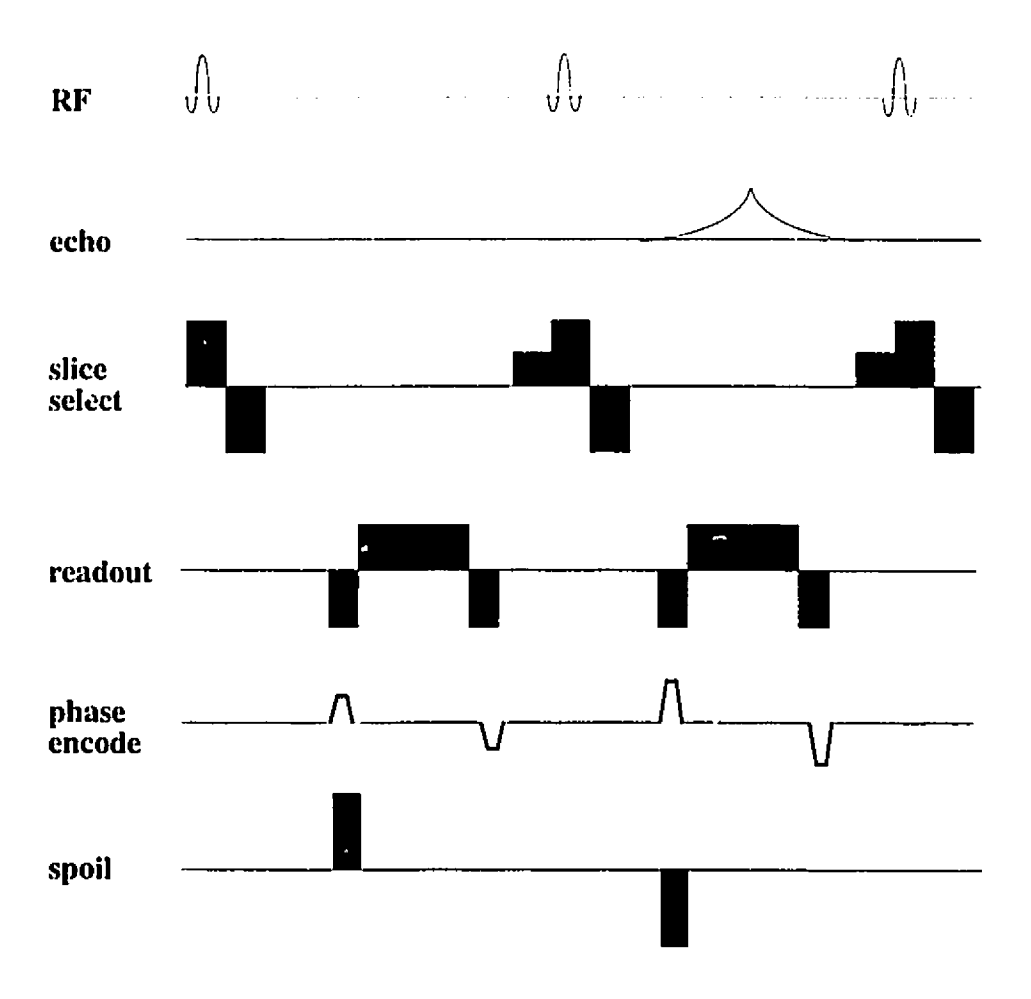


Figure 5.1: Echo-shifted pulse sequence: Both the rephasing lobes of the slice selection gradients and the alternating polarity spoiler gradients (bottom) dephase magnetization generated by the immediately preceding RF excitation pulse, and refocus that dephased in the previous TR. The area of the phase encoding and readout gradients are zero within each TR. (Redrawn from [56]).

mentation, which is slightly different from that of Moonen, the prephasing lobe of the readout gradient and the rephasing lobe of the slice selection gradient were inverted and scaled by two user defined parameters, α and β , respectively. As can be seen in Figure 5.2, these modified gradient waveforms accomplish the desired spoiling and refocusing, with minimal demands on the gradient amplitude and slew rate capabilities. One limitation of this approach is that gradient moment nulling was not easily implemented, and therefore no flow compensation was performed. RF phase cycling was not performed either.

Figure 5.2 shows how the first echo from a given RF pulse is shifted out of the immediately following readout window in the modified ES sequence and refocused again in the subsequent TR. To fully understand the spoiling mechanism, it is useful to view this as a shift of the readout window away from the origin of k-space with respect to the FID whose suppression is desired. Inspection of the areas of the various segments of the readout gradient reveals that the readout window is shifted² in k-space by $(\alpha + 1)k_{x_{max}}$ with respect to the initial FID, where $k_{x_{max}}$ is the absolute value of the maximum spatial frequency in the x direction that would normally be encoded.

Instead of being centred at $k_x=0$ and recording spatial frequencies from $-k_{x_{max}}$ to $+k_{x_{max}}$ from a gradient echo, the readout window will be centered at $(\alpha+1)k_{x_{max}}$ and spatial frequencies from $\alpha k_{x_{max}}$ to $(\alpha+2)k_{x_{max}}$ will be observed from the most recently generated FID. If the associated magnetization distribution contains significant spatial frequencies above $\alpha k_{x_{max}}$, then there will be unwanted interference. It is therefore necessary to select a value of α that is sufficiently large

²the shift in k-space is in the readout direction, which we will assume to be along the x axis in this example.

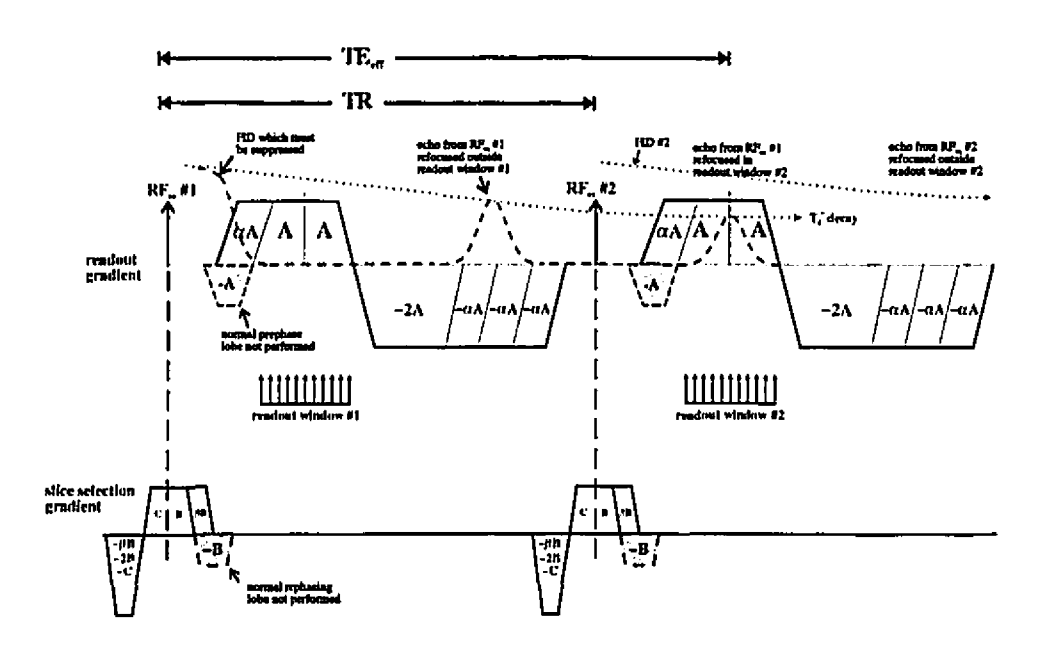


Figure 5.2: Schematic diagram of measurement and selection gradient waveforms for modified ES sequence, showing the FID and shifted gradient echos from the first excitation pulse (heavy dashed line). The readout period, represented by the 'comb', is preceded by the gradient lobe of area α A, rather than the normal prephasing lobe in the readout gradient. This serves to spoil the FID. The final, negative lobe of the readout gradient leads to a refocused echo from RF_{ex} #1 outside of readout window #1. In the following TR, an identical readout gradient waveform refocuses the echo from RF_{ex} #1 inside readout window #2 while simultaneously spoiling the new FID and shifting the echo from RF_{ex} #2 (light dotted lines) out of it. Choosing $\alpha = -1$ would be equivalent to using the normal prephasing lobe. The negative rephasing lobe of the slice selection gradient is replaced with a positive one of area β B, and a segment of area $-(\beta B - 2B - C)$ is added before the RF pulse, contributing to the dephasing of all echos in their first TR and rephasing in the second TR. Setting $\beta = -1$ would yield the normal rephasing gradient. The phase encoding gradient waveforms are not shown.

to prevent this, based on estimates of the spatial frequency content of the object.

In T2* weighted scans acquired on the MRI system used for this work, decreasing the voxel dimensions below .6 mm in-plane did not reveal any additional fine structure in the images. It was therefore assumed that the spatial frequency content typical of T2* weighted magnetization distributions in brain tissue was indistinguishable from noise above 0.8 mm^{-1} . As this was equivalent to five times the in-plane resolution of 3 mm chosen for the 3D ES acquisition, an α value of five was selected.

In order to ensure complete suppression of unwanted direct and stimulated echos, spoiling in the slice direction was also employed. The meaning of the β parameter is analogous to that of α , but the associated k-space shift is along the slice selection axis and its magnitude is equal to β times the k-space displacement produced by the slice selection gradient (which determines the range of spatial frequencies present in the nominal slice profile). In the 3D ES acquisition described here, a slab 36 mm across was targeted for selective excitation. As this was a fairly thick volume, the spatial frequency distribution was relatively narrow, and the k-space excursion produced by the slice selection gradient was only 0.167 mm⁻¹. Based on the estimated spatial frequency content of a T2* weighted brain volume specified above, β was also set to five.

Using the sequence and parameters described here, dynamic 3D image series of 48 frames each were used to image the response to aperiodic visual stimulation, with a total scan time of 8 minutes, 48 seconds. An oblique axial orientation passing through the calcarine fissure was chosen for selective excitation. The outer slice on each side of the volume was discarded due to inevitable deviation from a perfectly square excitation profile, and the inner five slices were used in subsequent

SROC analysis. For display purposes, the SROC derived *t*-maps were resampled to 1 mm resolution using tri-linear interpolation. In these studies a quadrature head coil was used for RF signal reception.

5.3 Results

Figure 5.3 shows reformatted cross sections of the first T2* weighted 3D image of a 48 frame dynamic series obtained during aperiodic stimulation with the Grass goggles. For comparison, Figure 5.3(d) shows the same region imaged using the conventional 2D acquisition described previously.

The most notable difference is the lower resolution of the 3D scan, and a reduction in the contrast between CSF, gray matter, and white matter. Partial volume dilution effects may explain the reduced contrast, as the various tissue types were better differentiated in 2D ES scans acquired at higher resolution.

Although 2D ES acquisitions were found to exhibit low SNR due to the shorter TR, smaller flip angle, and increased receiver bandwidth, the 3D ES images yielded good noise performance thanks to the larger voxel volume and the averaging effect of multiple phase encodes in the slice direction. Figure 5.4 shows time intensity curves from representative voxels in the dynamic series from which Figure 5.3 was taken. The RF background noise is comparable to that seen in Figure 4.6 for the conventional 2D acquisition, as are the intensity fluctuations seen in dormant, low noise regions of the brain as well as in regions of pulsatility artifact. Activation-induced signal changes of approximately 5 to 10% were observed, and these were easily detected in low noise regions of the brain. Figure 5.5 shows standard deviation images for the different slices and the t-maps in Figure 5.7 show the locations

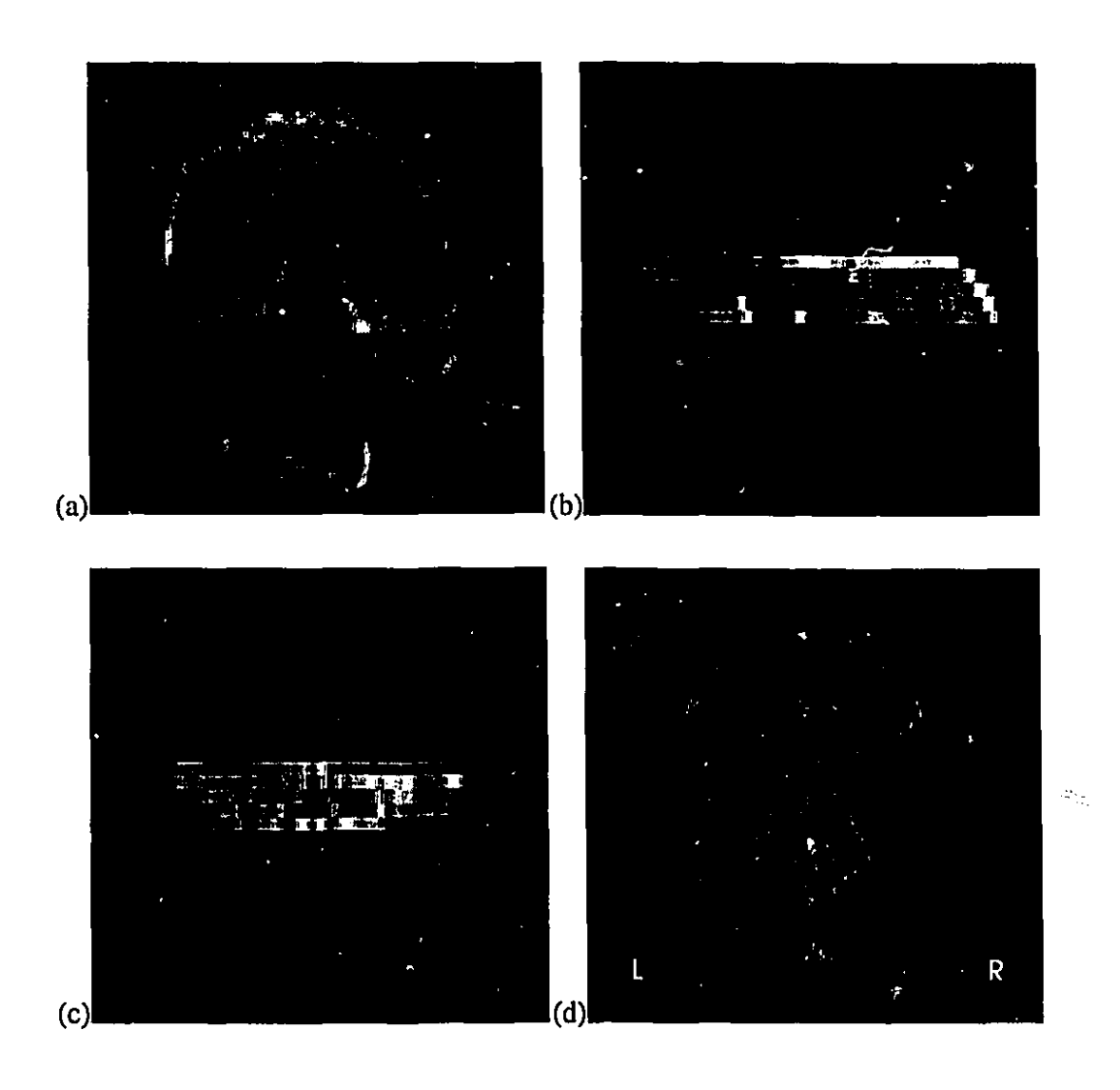


Figure 5.3: 3D ES T2* weighted images from visual study: (a) oblique axial view; (b) sagittal view from same volume; (c) coronal view; (d) conventional 2D image of the section shown in (a), for comparison.

of activated regions in the brain.

The highest noise levels are seen in the slice in Figure 5.5(a) beside the lateral ventricles, due to replication of pulsating CSF. Note the diffusely smeared noise background outside of and lateral to the head, due to the left to right in-plane phase encoding direction. These low level fluctuations originate from physiological sources and are present inside of the head as well. The thin dark bands at the top and bottom of the images represent regions which the faint motion and flow artifacts cannot reach via the phase-encoding direction, and where only RF noise is present. Figure 5.5(f) shows the standard deviation map from lowest slice thresholded and superimposed on a T1 weighted anatomic image of the region. The more anteriorly located bright spots are replicated portions of the lateral ventricles, and the more posterior ones are replications of the CSF in the superior cerebellar cistern. Interestingly, the ventricles themselves do not appear with high intensity in the standard deviation maps. Figure 5.6 shows a map of the standard deviation in the middle slice, expressed as a percentage of mean voxel intensity. In the occipital region, which is of primary interest in this study, the fluctuations are on the order of 2 to 5%. The high noise levels that were observed lateral to the sagittal sinus in the 2D standard deviation maps (Fig. 4.7) are completely absent in the 3D ES maps, possibly due to a reduction of the relative inflow enhancement in this vessel due to the volumetric acquisition.

The low noise levels enabled regions of stimulus-correlated signal change to be well localized. Figure 5.7 shows unthresholded t-maps obtained by SROC analysis for all five slices of the dynamic series examined above. Unlike the noisier 2D activation maps shown in the previous chapter, the SPM's in this section have not been subject to spatial filtering.

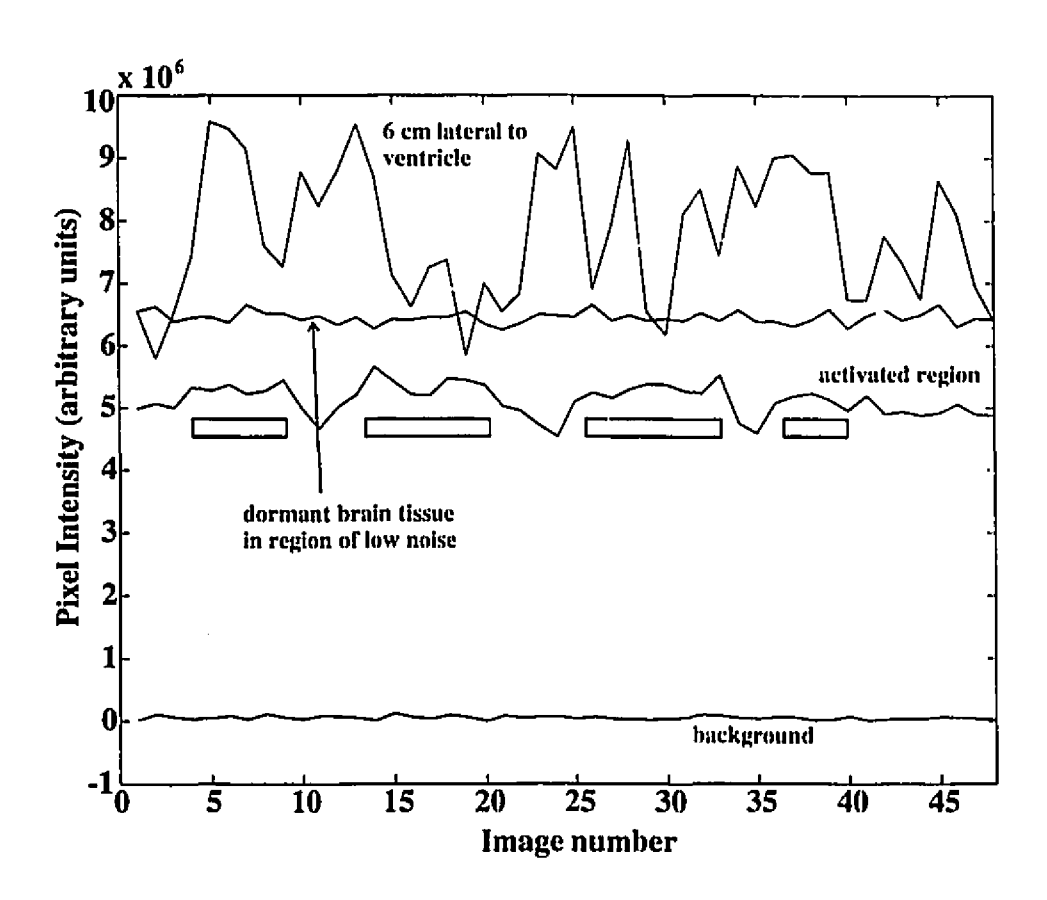


Figure 5.4: Time intensity curves from 3D ES T2* weighted image series from visual study: The grey bars denote periods during which the LED matrix goggles were flashing at 8 Hz. Activation-induced signal changes of approximately 10% are observed.

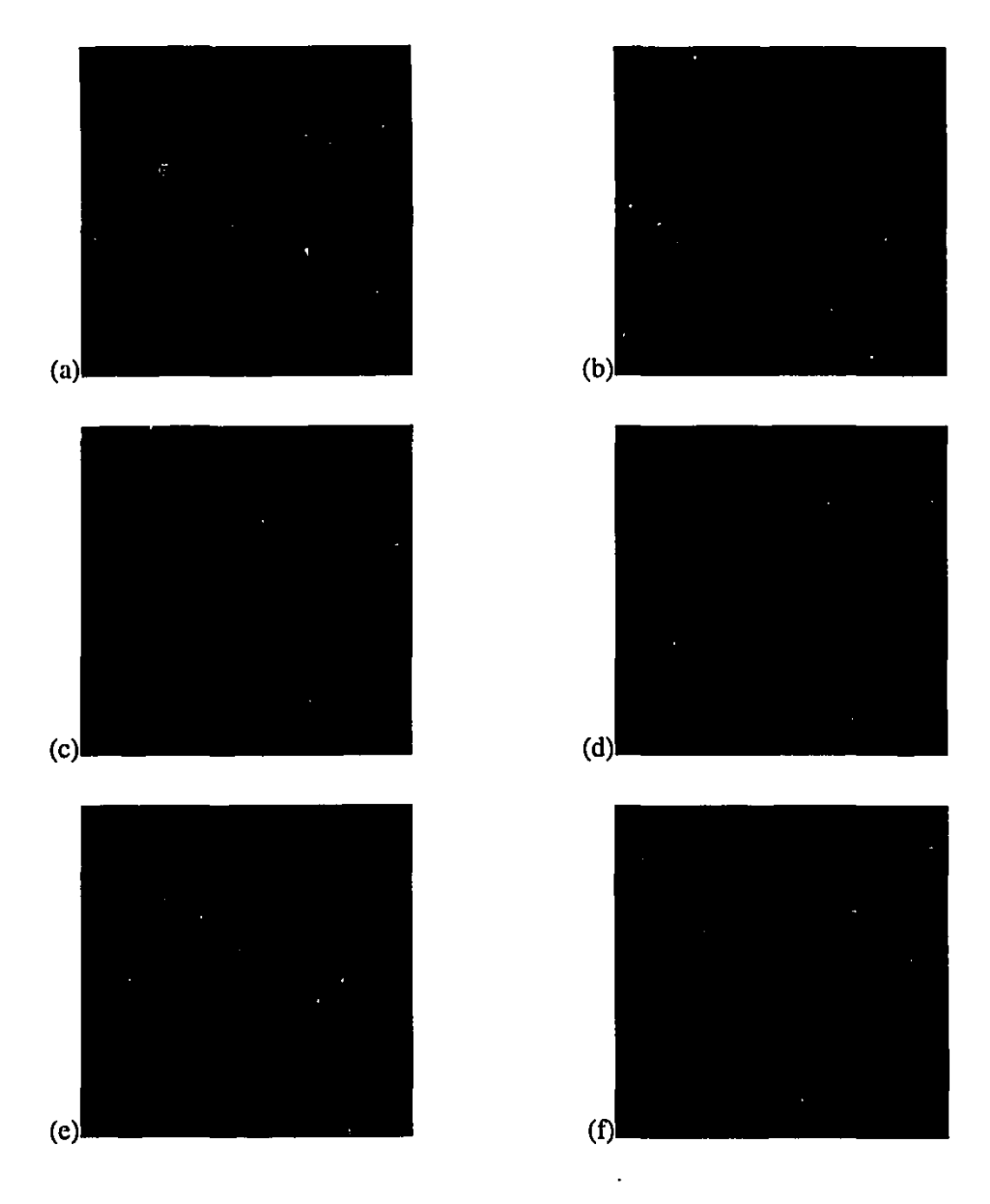


Figure 5.5: (a) to (e) Standard deviation images (oblique axial) from 3D ES visual study (inferior to superior); (f) thresholded standard deviation map from the slice in (a), superimposed on T1 weighted image.

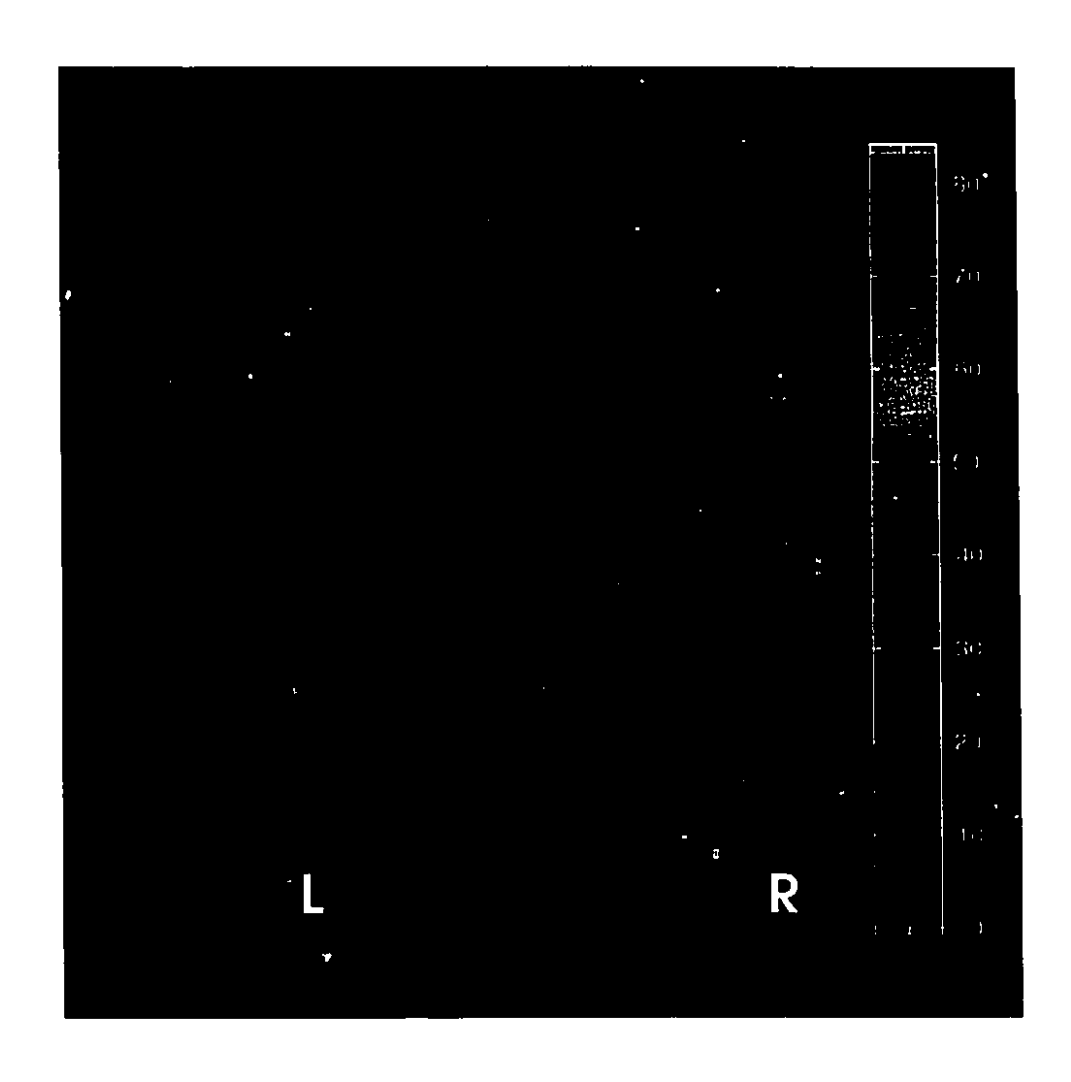


Figure 5.6: Standard deviation of 3D ES series for visual study expressed as percentage of mean voxel intensity. Over most of the image, this value is less than 5%.

The slice in Figure 5.7(c) passes through the calcarine fissure and the t-value in this region is well above the chosen threshold of t=3. Note the faint negatively correlated images of the displaced lateral ventricles visible in panel (a) of this figure (white arrows). Similar structures are visible in panel (c) left of center in the head. These are due to pulsatility artifacts that are incidentally correlated with the pattern of stimulation, although in this case, the t-values of the artifacts are below the threshold of statistical significance.

The regions of apparent activation were situated around the calcarine and central fissures, where the primary visual cortex in humans is known to reside[40]. Figure 5.8 shows thresholded (descriptive) t-maps superimposed on T1 weighted images acquired during the same session and displayed with the 'register' software. The correspondence of the activation foci with the sulcal anatomy is clearly demonstrated.

Figure 5.8(d) shows an MR angiogram of the region covered by the 3D functional study. The activated region shown in this view appears to follow a small veinous offshoot of the sagittal sinus. These images originate from the same subject as the 2D maps presented in the previous chapter, and comparison of Figure 5.7(c) with Figure 4.8(a) reveals a strong consistency in the shapes of the activation foci.

The cross sectional format used in Figure 5.8 is useful for showing the relationship between activated regions and the subcortical anatomy, but it is not the most natural way to assess the distribution of activation over the cortical surface. Figure 5.9 shows the distribution of activation over the medial wall of the occipital lobe and its relationship to the nearby vasculature in three dimensions.

The peak t values can be clearly seen to follow the small vein along the corti-

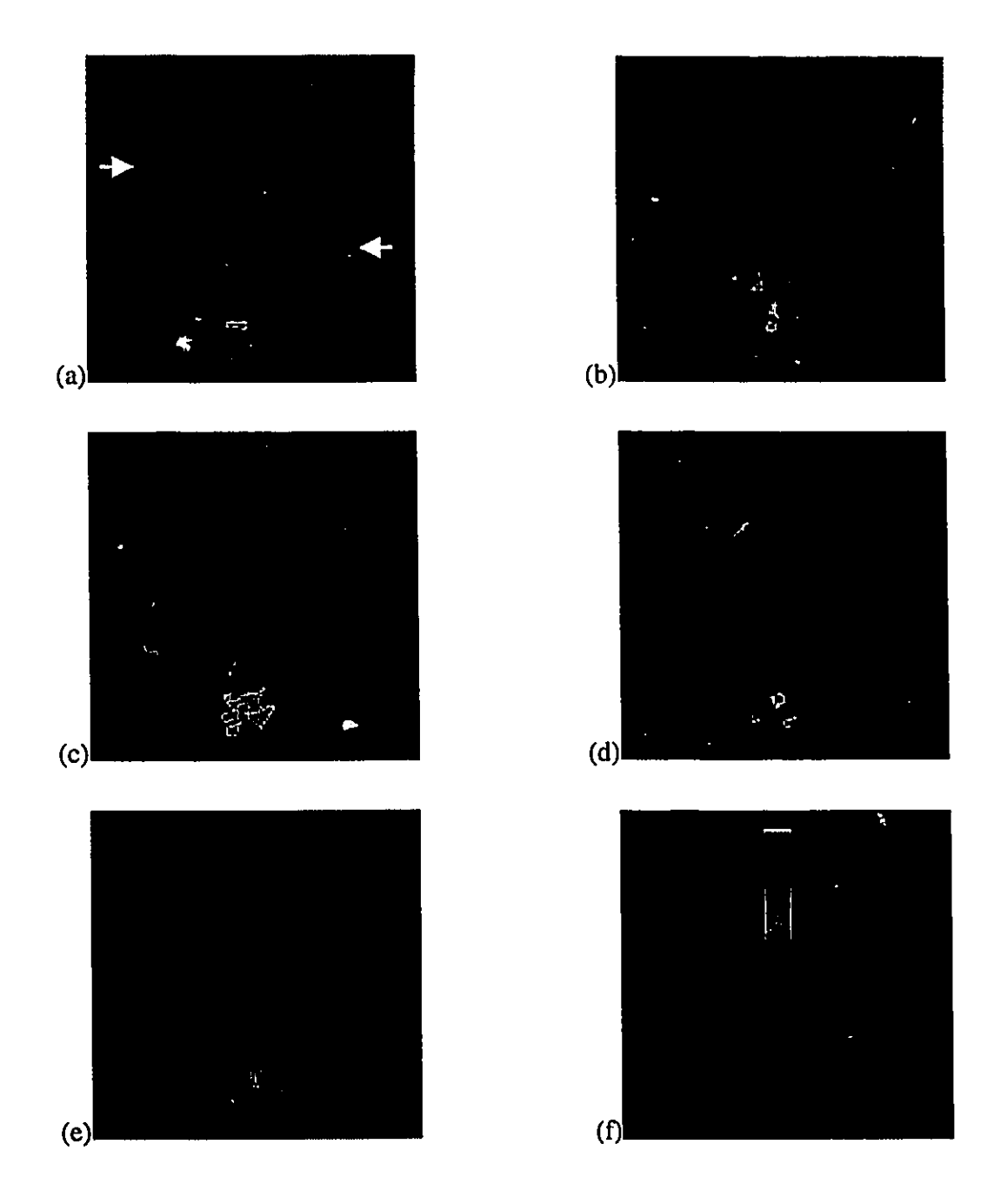


Figure 5.7: (a) to (e) t-maps for five oblique axial slices acquired in 3D ES visual study; (f) color legend for all slices.

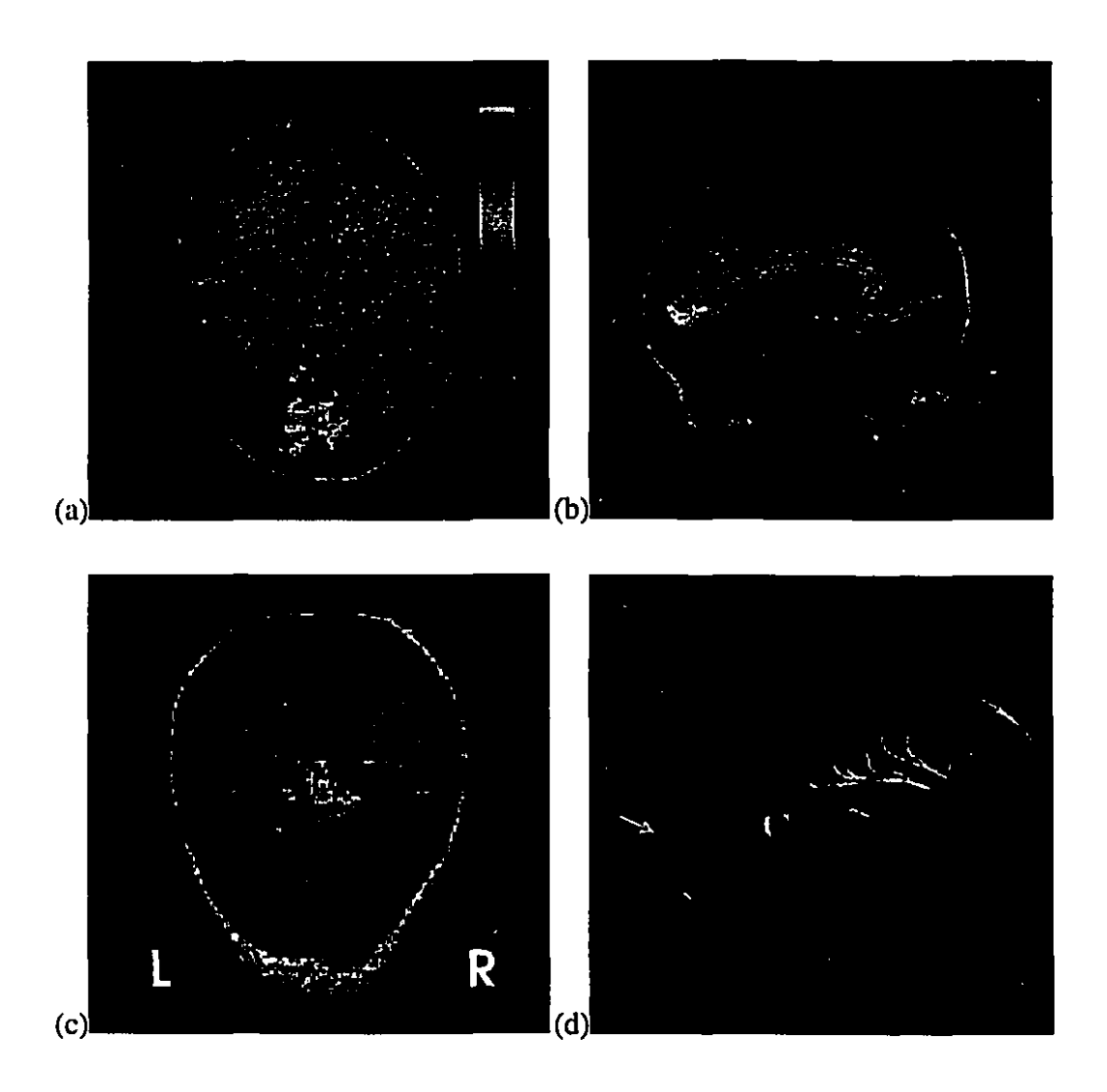


Figure 5.8: Descriptive (threshold: $t \ge 3.0$) SPM's for 3D ES visual study superimposed on corresponding anatomical images: (a) oblique axial slice through calcarine fissure; (b) sagittal section which shows the activation focus following the bend of the calcarine fissure; (c) coronal section showing extent of activated region along calcarine and central fissures; (d) sagittal slice from 3D MR angiogram along central fissure, showing a small midline vessel associated with part of the activated region (gray arrow).

cal surface as it crosses over the sulci. The image was generated using the Display program, which was used to extract a 3D representation of a portion of the cortical surface using an intensity threshold. The surface was then color coded based on the corresponding values of the 3D t-map from the visual stimulation study. The vessels shown were rendered using data from a high resolution MR angiogram and color coded in the same way as the cortical surface. The color coded value along the small vessel can be seen to rise and fall at several points along its length, and no significant activation is observed in the sagittal sinus. On the inferior gyrus of the calcarine fissure, there are two paths of focally intense t values which are suggestive of vessel paths.

5.4 Discussion

The three-dimensional t-maps generated using the ES sequence were consistent with those obtained using a conventional 2D acquisition over the volume of intersection. The 3D activation maps shown here permitted better visualization of the correspondence of activation foci with small blood vessels, however, despite their lower resolution.

The noise levels in the 3D dynamic series were low, due primarily to the very large voxel volume and also to the averaging effect of multiple phase encodes in the slice direction. For this reason the contrast to background noise ratio seen in the 3D t-maps of Figure 5.7 is significantly higher than that of the 2D maps, such as Figure 4.11.



Figure 5.9: Medial wall of the occipital lobe, color-coded to show the distribution of t values over the cortical surface. The activated region can be seen to follow a small vein leading to the sagittal sinus. The vessels are also color-coded to show t value along their paths, which is seen to rise and fall at various points along the smaller vessel. No activation is observed in the sagittal sinus.

Chapter 6

Retrospective Temporal

Resolution Selection

6.1 Introduction

In the fMRI studies described thus far in this thesis, spatial properties such as resolution and volume coverage have been the primary concerns. Detection of persistent regional changes, rather than observation of brief events, was the principal objective and scan time was only a consideration due to its effect on the temporal stability of the fMRI signal.

The ability to observe the changing MRI signal with high temporal resolution, while not necessarily essential for the identification of activated regions, is nonetheless desirable. Subtle features of the signal versus time plots from fMRI studies may offer important insight into the physiological basis of the response. Menon *et al.* have reportedly observed an initial signal decrease in T2* weighted image

series that they attribute to a short-lived drop in capillary oxygen tension immediately following stimulus presentation[51]. The duration of this initial dip is less than a second, so high temporal resolution is necessary to detect it. It may also be of interest to detect slight differences in the time of onset of the response in different regions of the brain.

Higher temporal resolution may also permit more sophisticated criteria to be applied to the problem of detecting activated regions. Postprocessing strategies such as the *t*-test and image subtraction deal with the detection problem as one of locating differences in static signal levels. Temporal resolution *per se* is therefore not an issue when such tests are used. The correlation methods, however, permit comparison of the dynamic properties of the fMRI signal to those of a reference waveform representative of the behaviour expected in activated regions. If there are distinctive features of the response waveform which occur on a short time-scale but serve to reliably identify activated regions, then temporal correlation analysis of high time resolution dynamic data may offer increased sensitivity and specificity over static methods.

In this chapter, a technique is presented which permits the acquisition of dynamic image series with 800 ms effective temporal resolution and the spatial properties of the 2D series acquired using the conventional sequence described in Chapter 4. The method is based on a gating approach similar to that applied in cardiac studies, and can be performed on a conventional clinical scanner without the addition of special hardware. A novel aspect of this technique is that a conventional dynamic image series can also be reconstructed from the same data.

6.2 Methods

In the previous chapter, the echo-shifting technique was used to increase volume coverage while retaining acceptable temporal resolution. Such conventional MRI techniques allow imaging of dynamic processes with a temporal resolution given by the acquisition time per image, and the signal-to-noise ratio is reduced significantly with decreases in scan time. For cyclic processes, synchronization or *gating* techniques, such as CINE[30, 54], can be used to image an average period with improved temporal resolution. This approach is commonly used for imaging the motion of the heart or blood flow during the cardiac cycle.

The need for such methods arose because only a fraction of the data needed to reconstruct a high time resolution image series of the beating heart could be acquired during a single stroke of the heart. If acquisition was synchronized with the cardiac cycle using an ECG and repeated over a number of heartbeats, however, the data acquired could be combined to produce a high time resolution depiction of an average cycle.

6.2.1 CINE Mode Acquisition

In a CINE acquisition, the same phase encode is acquired repeatedly during any given cycle of the process of interest. During successive cycles, the phase encode index is incremented until all row indices of the 2D DFT matrix necessary to form images with the desired field of view and spatial resolution are covered (Fig.6.1). It is then possible to form a complete image from the first phase encode of each cycle, followed by another image formed from the second phase encode of each cycle, and subsequent images from the rest of the phase encodes. This set of im-

ages depicts the periodic process over an average cycle at a time resolution given by the sequence repetition time.

In cardiac applications, variations in the pulsation period occur and it is necessary to interpolate within a given cycle to estimate the required phase encodes. The total time necessary to acquire data in this way depends on the number of phase encodes per image and on the length of the process period. For example, to produce a series of images with 128 phase encodes each over a cardiac cycle of mean duration one second, data must be acquired for 128 seconds.

This approach has also been applied to functional MRI of the brain, where periodic stimulus presentation patterns are commonly used[54]. The BOLD fMRI response occurs over a time scale of several seconds, however, so CINE mode studies lead to much longer acquisition times. To overcome this problem, a trade-off can be made prospectively between total scan time and temporal resolution using k-space segmentation methods[22] which group multiple phase encodings within each period.

6.2.2 Retrospective Temporal Resolution Selection

In both CINE and segmented k-space methods, it is assumed that the process being imaged is truly periodic, and neither of them permit examination of the true temporal evolution of the system that is imaged over the entire acquisition period. We introduce here a novel method of phase encode scheduling which permits the *retrospective* selection of temporal resolution (RTRS). This approach allows reconstruction of high time resolution images in a manner similar to gating using conventional k-space segmentation, while retaining the ability to reconstruct the

conventional dynamic image series which shows the behaviour of the system over the entire data acquisition period. Although the application demonstrated here is fMRI using a periodic stimulus, the method is applicable to imaging of any cyclic process.

The ability to retrospectively select the temporal resolution is achieved by repeatedly acquiring complete images and varying the phase encoding order used during each cycle of the periodic process. In a conventional gated acquisition a single phase encode (PE) index is acquired n times during each period and the PE number is incremented in successive periods. When all N_y PE's are collected, n images of an average cycle are reconstructed (Fig. 6.1).

In the approach presented here complete sets of N_y PE's for one or more images are acquired during the first cycle as illustrated in Figure 6.2. The process is then repeated with the PE order shifted by $N_y/2$. At this point, the PE's can be grouped in the order in which they have been acquired and reconstructed to form a set of truly sequential images (Fig. 6.2(a)) or they can be re-sorted into groups of phase encodes which have been acquired during equivalent intervals in the periodic process. This latter grouping permits reconstruction of the same number of images, but with twice the apparent temporal resolution (Fig. 6.2(b)). Continuing the acquisition and shifting the PE order by progressively smaller fractions permits further increases in temporal resolution (Fig. 6.3).

With a scan time equal to that of a conventional CINE acquisition, the data may be reconstructed to produce images with a temporal resolution anywhere between the scan time per image and that achievable with the conventional gated scan. Note that this is not possible using conventional CINE methods, in which only the high temporal resolution reconstruction is possible.

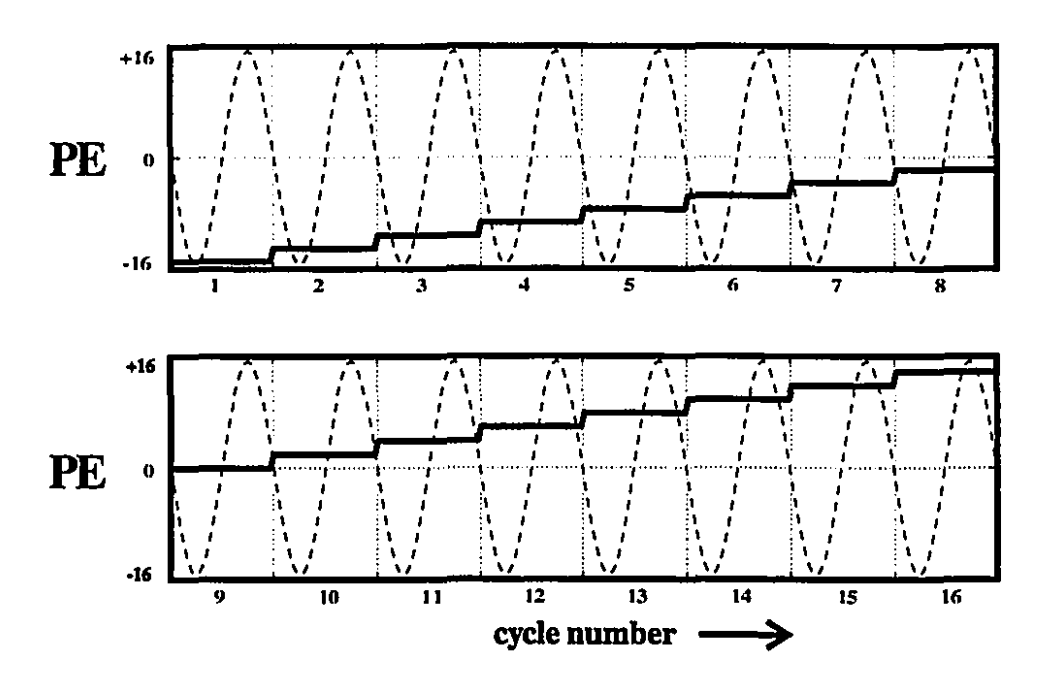


Figure 6.1: CINE mode acquisition: Phase encodes of constant index are repeatedly acquired within each cycle of a periodic process, and the index is incremented over successive cycles. The heavy solid line is a plot of the PE index and the dashed sinusoid represents the periodic process. If n phase encodes are acquired per cycle then after 16 cycles n images, comprised of 16 distinct phase encodes each, can be reconstructed to depict an average period at a time resolution equal to the sequence TR.

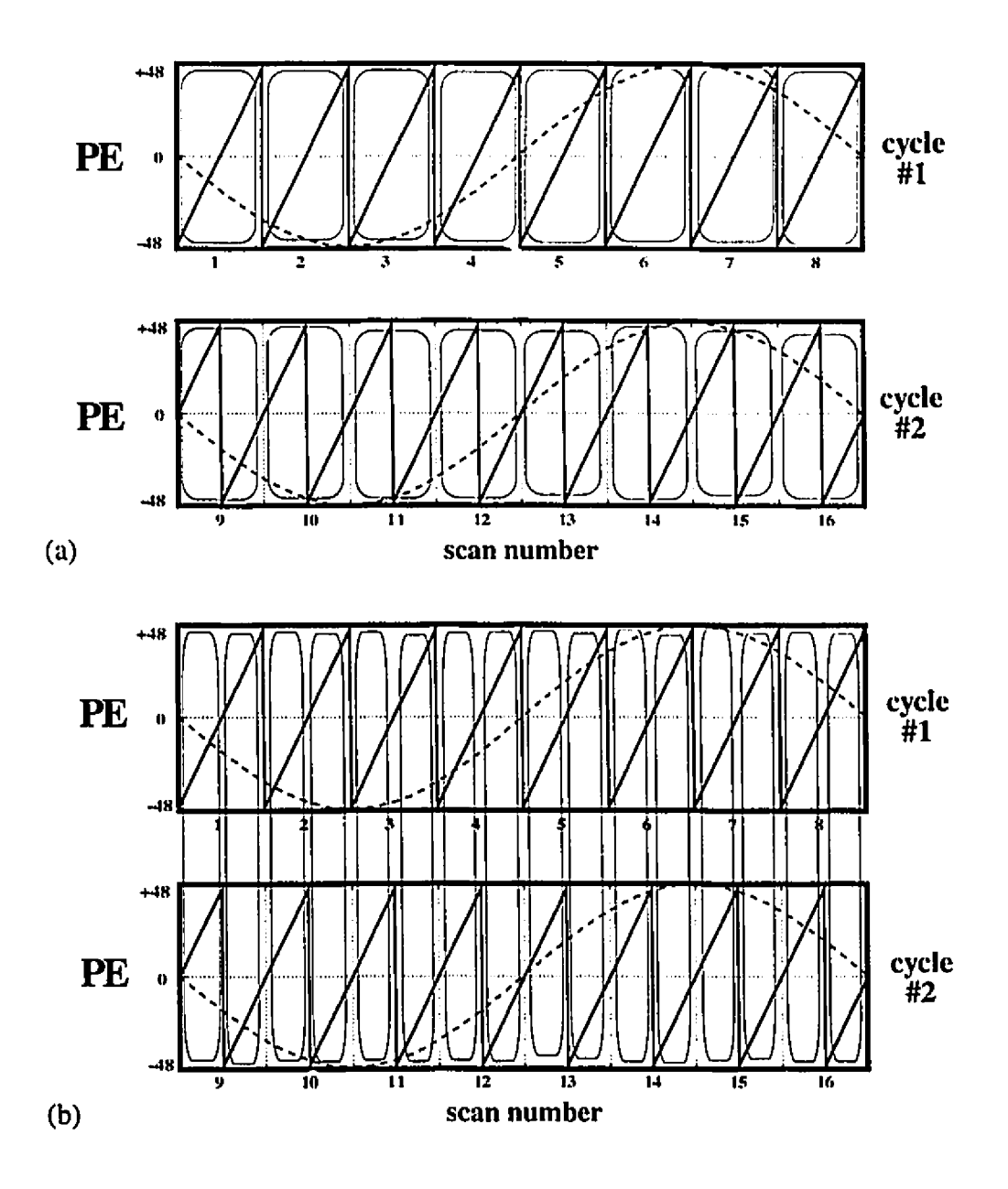


Figure 6.2: Phase encode scheduling for retrospective temporal resolution selection: (a) In each of two cycles shown, eight sets of 96 phase encodes (PE index as a function of time is represented by heavy solid line) are acquired, and assembled into consecutively acquired groups (thin outlines). This results in 16 groupings of 96 different phase encodes each, which can be recenstructed to form 16 images depicting two cycles. (b) Groups of 96 phase encodes are assembled based where they originate in the process cycle, and the 16 reconstructed images represent an averaged depiction of the cycle at twice the temporal resolution of (a).

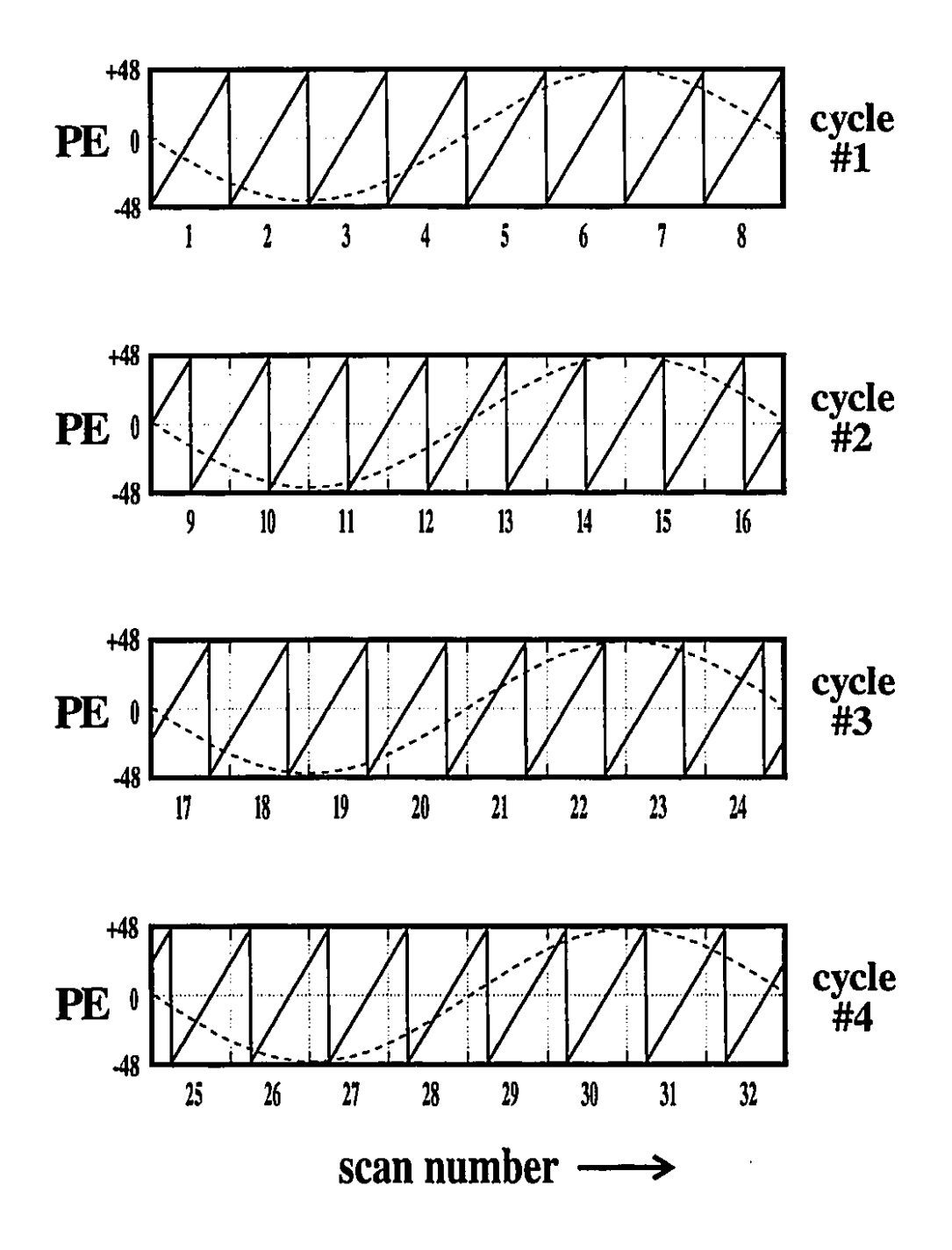


Figure 6.3: Shifting the phase encoding order by progressively smaller fractions permits further increases in pseudo-temporal resolution. In the example shown here, the original temporal resolution can be increased by a factor of four.

In addition to allowing retrospective temporal resolution selection, the phase encode scheduling described above ensures that the maximal temporal resolution possible can be attained for a given imaging time. If, for example, an acquisition is aborted prematurely (e.g. loss of breath hold in an abdominal study), images can be reconstructed from whatever data has been acquired, with the maximum possible temporal resolution. Retrospective temporal resolution selection can also be achieved with a simpler phase encoding schedule in which the order is shifted by a constant amount in each cycle, but this requires that the desired maximum temporal resolution be decided prospectively.

Using the RTRS approach, functional studies of visual stimulation using the Grass Goggles were performed. These studies each consisted of 64 dynamic coronal scans using the phase encode cycling scheme shown in Figure 6.2 and otherwise identical to the 2D sequence described in Chapter 4. During these acquisitions the stimulus was applied in a periodic fashion as described in Chapter 4 (four images on/four images off). Eight such cycles could be performed over the 64 image series, permitting the effective temporal resolution to be increased by a factor of eight.

Offline reconstruction software was written as a Matlab callable C routine. This program was run on an SGI Indy to re-sort the phase encodes and generate the high time resolution dynamic image series, which was then output as a MINC format file.

6.3 Results

Processing the data acquired during the visual studies provided a 64 frame dynamic image series which represented the response over a single 52 second averaged stimulus cycle, with a temporal resolution of 0.8 s/frame. Conventional dynamic series with a temporal resolution of 6.3 seconds were also reconstructed, and t-maps were generated from both dynamic series using SROC analysis.

The image quality of the normally reconstructed dynamic series was not affected in any way by the alternate phase-encoding order used, and the t-maps were focally intense along the calcarine and central fissures. Figure 6.4 shows an image reconstructed from the high time-resolution data and the t-map generated from the conventionally reconstructed dynamic series (note the correspondence with the reformatted coronal view of the 3D t-map in Figure 5.8(c)). The t-map from the high time resolution series was very similar to the one shown here. The pattern of t values includes several bright spots, which probably correspond to small blood vessels travelling along the depths of the calcarine sulci and along the central fissure and through the slice plane.

While the noise levels in the normally reconstructed image series were comparable to those observed in 2D series using conventional phase encode scheduling, the high time resolution series exhibited some artifacts. These can be seen in Figure 6.5, which shows time-intensity curves from several representative voxels in such a series.

The spatial structure of noise levels was also found to differ slightly from that observed in normally reconstructed dynamic series, although not in a detrimental way. Figure 6.6 shows standard deviation images from the high time resolution

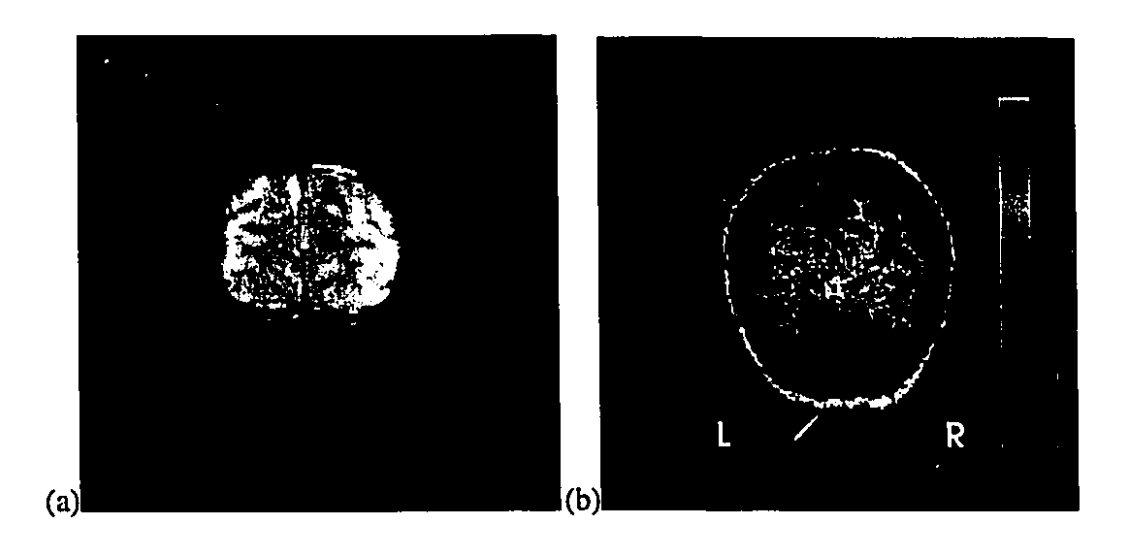


Figure 6.4: (a) Image from high time resolution series; (b) thresholded t-map from normally reconstructed data superimposed on T1 weighted anatomic image of the same region.

data set. The standard deviation map shown previously in Figure 4.7(a) was acquired during the same session with identical parameters using normal phase encode scheduling, and the pulsatility arfifacts observed in both images are manifested in a different way. In the standard deviation map from the high time resolution image, the artifact to either side of the superior sagittal sinus does not consist of distinct replications of the vessel as it does in the normal dynamic series. This is because the signal modulation over the cardiac cycle has a different periodicity in k-space for the re-sorted data. Figure 6.6(b) shows that the mean percentage fluctuation is similar to that achieved in the conventional sequence.

A prominent artifact can be seen in the top time-intensity curve in Figure 6.5, which shows the signal from an activated region at the center of the brain. In this

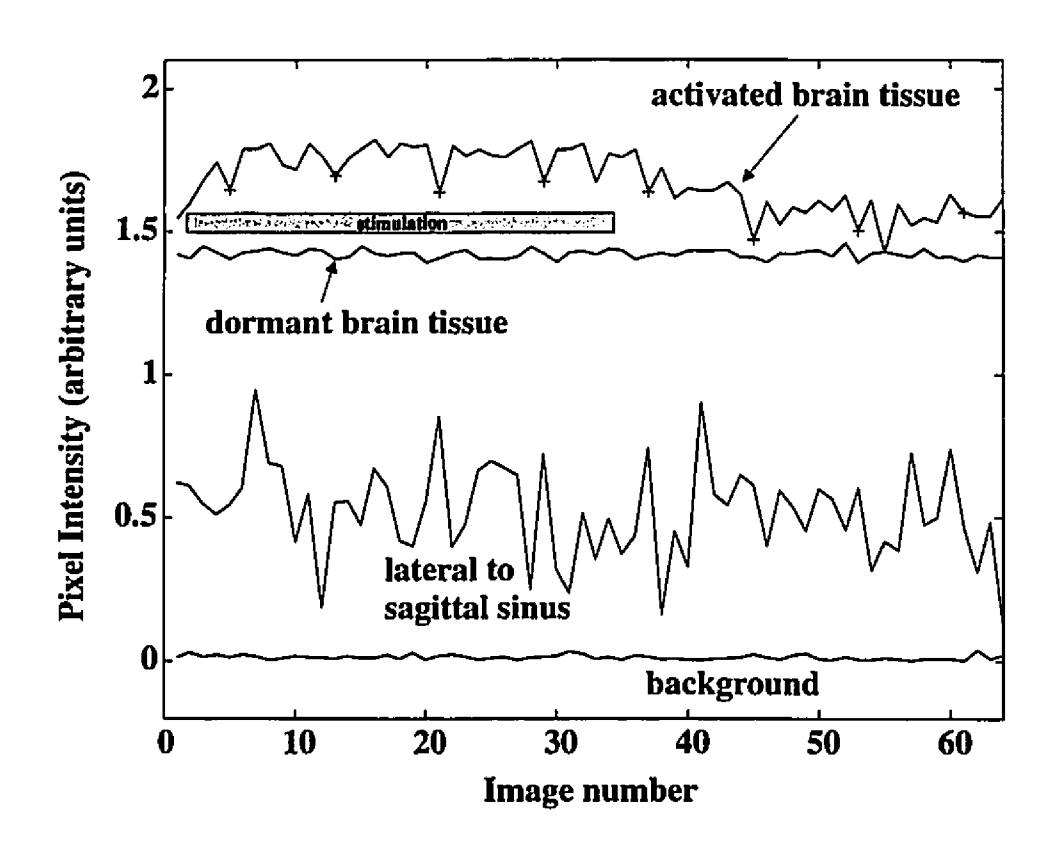


Figure 6.5: Time-intensity plots from four representative voxels in the high time resolution image series: the points marked '+' on the plot from activated tissue indicate noise spikes observed in every eighth frame starting with the fifth frame.

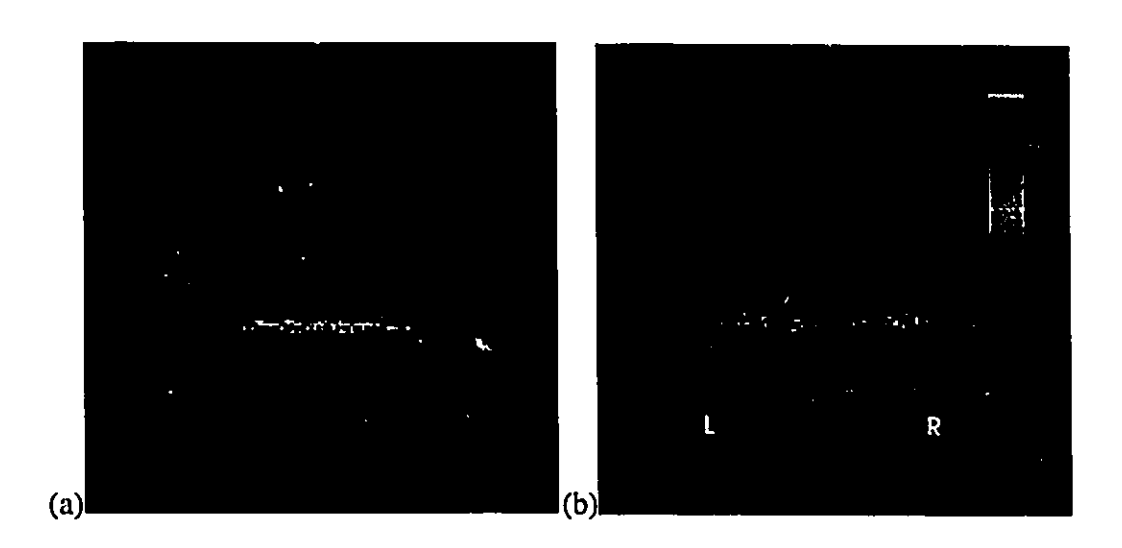


Figure 6.6: Standard deviation image from high time resolution dynamic series: (a) absolute deviation and (b) expressed as percentage of mean voxel intensity.

region of the image, transiently negative spikes were consistently observed at every eighth time point starting with the fifth frame. This was related to the fact that twelve out of the 24 lowest order phase encodes (indices -12 to -1 of -12 to +11) of these images were all acquired during the first cycle of stimulus modulation acquisition while the other half, indices 0 to 11, were obtained during the last cycle over six minutes later. There was a pronounced discontinuity in the modulus of the k-space data between the phase encodes of order 0 and -1, due to drift in the signal over this period.

These discontinuities led to 'cupping' of the intensity in the reconstructed images. This behaviour is due to the fact that an edge or discontinuity in a function of two dimensions increases its high frequency content, resulting in increased values away from the origin in its Fourier transform. Figure 6.7 shows two images

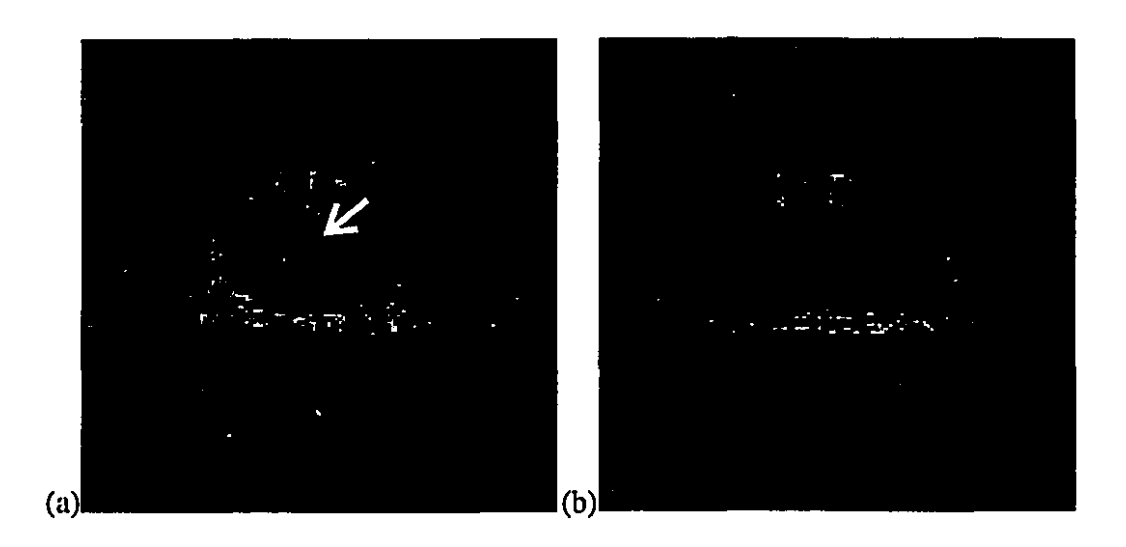


Figure 6.7: Image intensity cupping in high time resolution images; the two images shown here have had the mean of all 64 images subtracted from them: (a) the 21st image in the dynamic series is darker at the center (arrow) due to the discontinuity at the origin in the k-space data; (b) the intensity of the 6th image in the series is uniform over the center.

from the high time resolution dynamic series, one with and the other without this cupping artifact.

To compensate for this effect, a crude intensity uniformity correction was performed. The average of all 64 images was first calculated and then low pass filtered with a 32 pixel FWHM Gaussian kernel. Next, each image in the dynamic series was similarly filtered, and a correction factor for each pixel was calculated by dividing the blurred mean image by the blurred individual image. Application of this correction factor to the unblurred dynamic images resulted in the almost complete elimination of the cupping artifacts, and improved the appearance of the time-intensity curves. Figure 6.8 shows plots of signal intensity from an ROI in an acti-

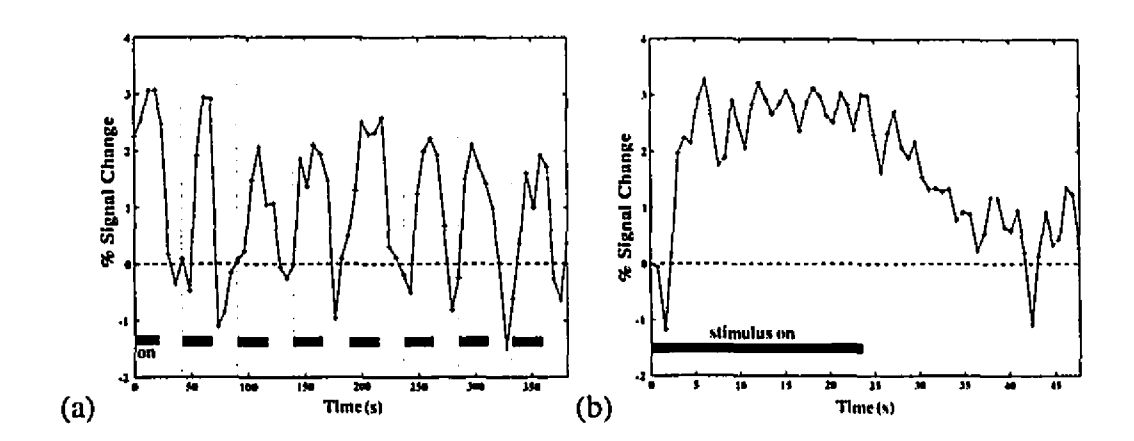


Figure 6.8: Time intensity curves from a 4 x 4 voxel ROI in an activated region from both low (a) and high (b) time resolution reconstructions of data acquired during periodic visual stimulation; the high time resolution series was corrected for image intensity non-uniformity. Black bars indicate periods of stimulus presentation.

vated region from the normally reconstructed dynamic image series, and from the high time resolution reconstruction following correction for cupping. The essence of the RTRS technique is that these two plots were generated from the same raw data.

6.4 Discussion

In this chapter it was demonstrated that a modified phase encoding schedule can be used to permit the retrospective selection of temporal resolution. This allowed activation-induced signal changes to be observed with high temporal resolution as well as inspection of the long-term signal behaviour in the activated region, which in this case included considerable variation of the response over successive cycles. This long-term variation led to discontinuities in the k-space data after re-sorting, and consequently to intensity non-uniformity in the high time resolution image series. Even after intensity uniformity correction, some negative spikes are still visible in the high time resolution plot of Figure 6.8, probably due to this effect. Nonetheless, a signal change of approximately 2.5% is clearly visible in the high time resolution plot, and its time course is well resolved.

The crude intensity uniformity correction could be improved by fitting a low order polynomial surface to the images rather than blurring them by convolution. Filtering by convolution leads to broadening of intensity peaks, lowering their maximum amplitude. Fitting a low order polynomial surface to the mean image and to each dynamic image would be more accurate.

Time domain filtering could be applied to the dynamic image data, but care must be taken to avoid distorting the shape of the response. Furthermore, temporal filtering with a very low cutoff frequency would defeat the purpose of acquiring the data with increased temporal resolution. The data shown in this chapter have not been subject to any filtering, in order to accurately portray the level of intensity fluctuation present in the data.

The problems caused by discontinuities between k-space segments acquired in different cycles could perhaps be reduced by shifting the phase encoding order by a constant number of indices from cycle to cycle, rather than by successively smaller powers of two as done here. The time separating acquisition of some of the adjacent k-space segments would thereby be reduced to the process period. Images in which the zero and lowest positive order phase encodes are acquired in the first cycle would still obtain their lowest negative order phase encodes in the last cycle, however. Also, the ability to reconstruct at increased temporal resolution

following interruption of data acquisition at an arbitrary point in the dynamic scan sequence would be lost.

One potential advantage of the RTRS technique over conventional gating methods is that some sources of long term signal drift, which almost invariably causes artifacts in the high time resolution image series, may be better corrected using the normal dynamic images. One purpose for which this might be useful is the correction of motion artifacts. Gradual shifts in subject position over the length of the dynamic scan can lead to differences in the measured k-space data that are large enough to produce the spike artifacts seen in Figure 6.5. Motion correction on the complex images could be applied to the 'true' dynamic series and then the data could be returned to the spatial frequency domain for subsequent re-sorting and Fourier inversion to generate a high time resolution series corrected for long-term motion.

Chapter 7

Conclusions and Suggestions for Future Research

Techniques have been presented for performing fMRI, with greater temporal resolution and volumetric coverage than conventional 2D spin warp techniques, on systems without EPI hardware. Two approaches have been considered: a 3D echoshifted acquisition and a 2D sequence allowing retrospective selection of temporal resolution. fMRI data acquired using these approaches have been compared with studies performed on the same subject using a conventional 2D sequence.

In the historical review of functional brain mapping, it was noted that the new technique of fMRI has partly addressed the need for a non-invasive approach with higher spatial and temporal resolution than PET. Although the echo-planar techniques used in the earliest studies have remained the method of choice due to the high temporal resolution, the stability of the signal in the presence of motion, and the ease with which multi-slice studies can be performed, the need for special hard-

ware has prevented many sites from performing EPI.

Alternative techniques for fast imaging have therefore been introduced. These include Moonen's echo-shifting technique, and the use of CINE mode acquisitions for observing the response to periodic stimulation. The nominal speeds of these techniques approach that of EPI but they do not benefit from its relative immunity to motion and pulsatility artifact.

An important class of fast imaging techniques that has received little mention in this report is that employing alternate k-space trajectories, such as spiral imaging. In this approach, spiral pathways are used to fill k-space, providing adequate coverage with a small number of excitation pulses (e.g. twelve[55]). These techniques, which do not require special high performance gradients¹, are on the order of ten times faster than conventional spin-warp methods, and have been found to be much less sensitive to physiologically induced signal fluctuations.

The spiral technique was initally chosen as the best candidate for fast 3D functional imaging on our system, and a spiral sequence was in fact implemented in the course of this work. The limited speed of the microprocessor controller of our system's gradient subsystem made the use of interleaved spiral imaging impractical for fMRI, however, illustrating that gradient amplifiers are not the only component of a system which can limit its flexibility.

To allow 3D functional MRI to be performed on our system without spiral imaging or EPI, a 3D ES acquisition was implemented. In tests on healthy volunteers using visual stimulation, this sequence was found to perform as well as a conventional 2D sequence in terms of the contrast-to-noise ratio, but with lower spatial

¹shielded gradients, which significantly reduce eddy current distortion, may be a necessity however.

resolution. The activated regions identified in the 3D statistical maps were consistent with the known anatomical sites associated with vision in humans, and with the corresponding 2D maps obtained in the same subject.

To measure the average response to periodic stimulation on a short time scale while permitting verification of the long term behaviour of the signal, the RTRS method was introduced. A pulse sequence and reconstruction software were implemented and again demonstrated on a healthy volunteer during presentation of a periodic visual stimulus. The time course of the response was clearly resolved with increased temporal resolution, but transient noise spikes were observed in the data. These artifacts were attenuated by applying an intensity uniformity correction, and low pass temporal filtering would probably eliminate them.

In applications such as cardiac and blood flow imaging, which do not have the stringent signal stability requirements of fMRI, the RTRS technique may prove useful. Using the phase encoding schedule employed in this work, premature release of breath-hold does not prevent reconstruction of the data at the maximum possible temporal resolution. As well, the ability to verify an image series which represents the true evolution of the system imaged over time may be useful in checking for gross motion. There may be applications in which it is desired to examine one part of the anatomy at high time resolution over a cyclic process, while simultaneously monitoring the long-term behaviour of a nearby region. The RTRS technique would make this possible.

Although neither the 3D ES technique nor the RTRS method investigated in this work provide the signal stability and speed of single-shot EPI or spiral imaging, both of which allow acquisition of complete images in less than a second, the methods are compatible with incorporation of spiral sampling trajectories and high

performance gradient systems. Through judicious combination of these and other techniques, and by analyzing the trade-offs between temporal and spatial resolution, immunity to physiological noise, and volume coverage, increased flexibility will be attained.

It is important to remember that high temporal resolution may not be in itself essential for the detection of activated regions. Bandettini *et al.* have reported persistent responses to sustained stimulation, for periods of up to 20 minutes[6], in both BOLD and flow sensitive sequences. If means of reducing unwanted physiologically based intensity fluctuations in long duration scans are devised, then high resolution 3D scans over larger volumes may become possible and further increases in flexibility will be afforded.

True 3D data acquisition is desirable mainly because the associated impulse response is more isotropic than that achieved using multi-slice EPI. Currently, whole brain functional imaging using high resolution 3D techniques is not feasible because it is impossible for the subject to remain still over the long scan time required to acquire T2* weighted volumes. It appears that such motion, in addition to causing corrigible misregistration artifacts, leads to more complex intensity non-uniformities from the sporadic modulation of the k-space data which can not easily be corrected.

It is possible that combining echo-shifting and spiral imaging with high-performance gradient systems will reduce the time needed to acquire a high resolution T2* weighted brain volume to the extent that subject motion will become more manageable. Incorporation of spiral sampling and navigator echo correction could further reduce the significance of motion-induced signal fluctuations. Motion and the possibly finite duration of activation-induced signal changes could also be dealt

with by acquiring groups of phase encodes for activated and baseline volumes in an interleaved fashion, and the experience gained with RTRS methods will likely be useful in designing such sequences.

Another property of 3D fMRI which makes it worth investigating is that acquisitions in which a large portion of the head is excited with a low uniform flip angle should exhibit almost no sensitivity to inflow enhancement. The ability to completely eliminate confounding factors like inflow sensitivity is of considerable value in fMRI, where ambiguity can hinder the proper interpretation of experimental observations.

In light of the growing body of evidence that intravascular spins are the dominant source of the BOLD signal, 3D fMRI with high isotropic resolution in conjunction with high resolution MRA may provide the best means of producing interpretable activation maps. Even if the detectable signal changes arise exclusively in blood vessels, tracing them to sufficiently small branches on the vascular tree should bring one into close proximity with the neuronal population that was selectively excited by the experimental paradigm. This approach may also aid in the interpretation of PET activation studies.

Bibliography

- [1] Proc. SMRM, 13th Annual Meeting, San Francisco, 1994.
- [2] Proc. SMR, Third Scientific Meeting and Exhibition, 1995.
- [3] D.L. Arnold. Clinical applications of magnetic resonance spectroscopy in neurological disorders. In Bronskill and Sprawls [16], pages 571–586.
- [4] Mark M. Bahn. A single-step method for estimation of local cerebral blood volume from susceptibility contrast MRI images. *Magnetic Resonance in Medicine*, 33:309–317, 1995.
- [5] J.R. Baker, R.M. Weisskoff, C.E. Stern, D.N. Kennedy, A. Jiang, K.K. Kwong, L.B. Kolodny, T.L. Davis, J.L. Boxerman, B.R. Buchbinder, V.J. Wedeen, J.W. Belliveau, and B.R. Rosen. Statistical assessment of functional MRI signal change. In *Proc. SMRM*, 13th Annual Meeting, San Francisco [1], page 626.
- [6] P.A. Bandettini, T.L. Davis, K.K. Kwong, P.T. Fox, A. Jiang, J.R. Baker, J.W. Belliveau, R.M. Weisskoff, and B.R. Rosen. FMRI and PET demonstrate sustained blood oxygenation and flow enhancement during extended visual

- stimulation durations. In *Proc. SMR*, *Third Scientific Meeting and Exhibition* [2], page 453.
- [7] Peter A. Bandettini, A. Jesmanowicz, Eric C. Wong, and James S. Hyde. Processing strategies for time-course data sets in functional MRI of the human brain. *Magnetic Resonance in Medecine*, 30:161–173, 1993.
- [8] Peter A. Bandettini, Eric C. Wong, A. Jesmanowicz, R. Scott Hinks, and James S. Hyde. Spin-echo and gradient-echo EPI of human brain activation using bold contrast: a comparitive study at 1.5 T. NMR in Biomedicine, 7:12– 20, 1994.
- [9] John W. Belliveau, Bruce R. Rosen, Howard L. Kantor, Richard R. Rzedzian, David N. Kennedy, Robert C. McKinstry, James M. Vevea, Mark S. Cohen, Ian L. Pykett, and Thomas J. Brady. Functional cerebral imaging by susceptibility-contrast NMR. *Magnetic Resonance in Medicine*, 14:538–546, 1990.
- [10] J.W. Belliveau, D.N. Kennedy, R.C. McKinstry, B.R. Buchbinder, R.M. Weisskoff, M.S. Cohen, J.M. Vevea, T.J. Brady, and B.R. Rosen. Functional mapping of the human visual cortex by magnetic resonance imaging. *Nature*, 254:716–718, 1 November 1991.
- [11] F. Bloch. Nuclear induction. *Physics Review*, 69:460–473, 1946.
- [12] N. Bloembergen, E.M. Purcell, and R.V. Pound. Relaxation effects in nuclear magnetic resonance absorption. *Physical Review*, 73:679–712, 1948.

- [13] J. Boxerman, R. Weisskoff, B. Hoppel, L. Hamberg, and B. Rosen. Model. In Proc. SMRM, 12th Annual Meeting, New York, page 389, 1993.
- [14] J. Boxerman, R. Weisskoff, K.K. Kwong, T.L. Davis, and B.R. Rosen. The intravascular contribution to fMRI signal change: Modelling and diffusionweighted in vivo studies. In *Proc. SMRM*, 13th Annual Meeting, San Francisco [1], page 619.
- [15] Jerrold L. Boxerman, Peter A. Bandettini, Kenneth K. Kwong, John R. Baker, Timothy L. Davis, Bruce R. Rosen, and Robert M. Weisskoff. The intravascular contribution to fMRI signal change: Monte carlo modeling and diffusion-weighted studies in vivo. *Magnetic Resonance in Medicine*, 34:4– 10, 1995.
- [16] Michael J. Bronskill and Perry Sprawls, editors. The Physics of MRI: 1992 AAPM Summer School Proceedings. American Institute of Physics, Woodbury, NY, 1993.
- [17] R. Todd Constable, Pawel Skudlarski, Aina Puce, Greg McCarthy, and John C. Gore. ROC analysis for evaluating functional brain MR imaging and post-processing protocols. In *Proc. SMRM*, 13th Annual Meeting, San Francisco [1], page 627.
- [18] Ray Cooper, H.J. Crow, W. Grey Walter, and A.L. Winter. Regional control of cerebral vascular reactivity and oxygen supply in man. *Brain Research*, 3:174–191, 1966.

- [19] H.M. Duvernoy, S. Delon, and J.L. Vannson. Cortical blood vessels of the human brain. *Brain Research Bulletin*, 7:519–579, 1981.
- [20] Jeff H. Duyn, Venhatha S. Mattay, Roy H. Sexton, Geoffrey S. Sobering, Fernando A. Barrios, Guoying Liu, Joseph A. Frank, Daniel R. Weinberger, and Chrit T.W. Moonen. 3-Dimensional functional imaging of human brain using echo-shifted flash MRI. *Magnetic Resonance in Medicine*, 32:150–155, 1994.
- [21] Jeff H. Duyn, Chrit T.W. Moonen, Gert H. van Yperen, Ruud W. de Boer, and Peter R. Loyten. Inflow versus deoxyhemoglobin effects in bold functional MRI using gradient echos at 1.5 T. NMR in Biomedicine, 7:83-88, 1994.
- [22] R.R. Edelman, B. Wallner, A. Singer, D.J. Atkinson, and S. Saini. Segmented turboFLASH: method for breath-hold MR imaging of the liver with flexible contrast. *Radiology*, 177:515–521, 1990.
- [23] Peter T. Fox and Marcus E. Raichle. Focal physiological uncoupling of cerebral blood flow and oxidative metabolism during somatorsensory stimulation in human subjects. *Proc. Natl. Acad. Sci. USA*, 83:1140–1144, February 1986.
- [24] Peter T. Fox, Marcus E. Raichle, Mark A. Mintun, and Carmen Dence. Nonoxidative glucose consumption during focal physiologic neural activity. Science, 241:462–464, 22 July 1988.
- [25] Jens Frahm, Klaus-Dietmar Merboldt, Wolfgang Hänicke, Andreas Kleinschmidt, and Henning Boecker. Brain or vein oxygenation or flow? on

- signal physiology in functional MRI of human brain activation. *NMR in Biomedicine*, 7:45–33, 1994.
- [26] K.J. Friston, P. Jezzard, and R. Turner. Analysis of functional MRI timeseries. *Human Brain Mapping*, 1:153–171, 1994.
- [27] Ron D. Frostig, Edmund E. Lieke, Daniel Y. Ts'o, and Amiram Grinvald. Cortical functional architecture and local coupling between neuronal activity and the microcirculation revealed by in vivo high-resolution optical imaging of intrinsic signals. Proc. Natl. Acad. Sci. USA, 87:6082–6086, August 1990.
- [28] Gary H. Glover. Gradient echo imaging. In Bronskill and Sprawls [16], pages 188–205.
- [29] Gary H. Glover and Adrian T. Lee. Motion artifacts in fMRI: Comparison of 2DFT with PR and spiral scan methods. *Magnetic Resonance in Medicine*, 33:624–635, 1995.
- [30] G.H. Glover and N.J. Pelc. A rapid-gated cine MRI technique. *Magnetic Resonance Annual*, pages 299–333, 1988.
- [31] John C. Gore, Richard P. Kennan, and Jianhui Zhong. MRI contrast agents: Principles and constraints. In Bronskill and Sprawls [16], pages 478–505.
- [32] A. Guyton. *Textbook of Medical Physiology*. W.B. Saunders Co., Philadelphia, 1991.
- [33] E.M. Haacke, A. Hopkins, S. Lai, P. Buckley, L. Friedman, H. Meltzer, P. Hedera, R. Friedland, S. Klein, L. Thompson, D. Detterman, J. Tkach, and

- J.S. Lewin. 2D and 3D high resolution gradient echo functional imaging of the brain: Venous contributions to signal in motor cortex studies. *NMR in Biomedicine*, 7:54–62, 1994.
- [34] E.L. Hahn. Spin echoes. Phys. Review, 80:580-594, 1950.
- [35] Joseph V. Hajnal, Ralph Myers, Angela Oatridge, Jane E. Schwieso, Ian R. Young, and Graeme M. Bydder. Artifacts due to stimulus correlated motion in functional imaging of the brain. *Magnetic Resonance in Medicine*, 31:283–291, 1994.
- [36] J.V. Hajnal, A. Oatridge, G.M. Bydder, and I.R. Young. A sinc based interpolation and coregistration method for precise image matching in functional imaging and other serial MRI studies. In *Proc. SMRM*, 13th Annual Meeting, San Francisco [1], page 527.
- [37] G.N. Hounsfield, J. Ambrose, B.J. Perry, and C. Bridges. Computerized transverse axial scanning (tomography). *British Journal of Radiology*, 46:1016–1051, 1973.
- [38] Xiaoping Hu and Seong-Gi Kim. Reduction of signal fluctuation in functional MRI using navigator echoes. *Magnetic Resonance in Medicine*, 31:495–503, 1994.
- [39] Jay Ingram. The Burning House. Viking, Toronto, 1994.
- [40] Eric R. Kandel, James H. Schwartz, and Thomas M. Jessell. *Principles of Neural Science*. Appleton & Lange, Norwalk, 3 edition, 1991.

- [41] R. Kennan, J. Zhong, and J. Gore. Intravascular susceptibility contrast mechanisms in tissues. *Magn. Reson. Med.*, 31:9–21, 1994.
- [42] Seong-Gi Kim, Kristy Hendrich, Xiaoping Hu, Hellmut Merkle, and Kâmil Uğurbil. Potential pitfalls of functional MRI using conventional gradient-recalled echo techniques. *NMR in Biomedicine*, 7:69–74, 1994.
- [43] Kenneth K. Kwong, John W. Belliveau, David A. Chesler, Inna E. Goldberg, Robert M. Weisskoff, Brigitte P. Poncelet, David N. Kennedy, Bernice E. Hoppel, Mark S. Cohen, Robert Turner, Hong-Ming Cheng, Thomas J. Brady, and Bruce R. Rosen. Dynamic magnetic resonance imaging of human brain activity during primary sensory stimulation. *Proc. Natl. Acad. Sci. USA*, 89:5675–5679, June 1992.
- [44] S. Lai, A.L. Hopkins, E.M. Haacke, D. Li, B.A. Wasserman, P. Buckley, L. Friedman, H. Meltzer, P. Hedera, and R. Friedland. Identification of vascular structures as a major source of signal contrast in high resolution 2D and 3D functional activation imaging of the motor cortex at 1.5 T: Preliminary results. *Magnetic Resonance in Medicine*, 30:387–392, 1993.
- [45] P.C. Lauterbur. Image formation by induced local interactions: Examples employing nuclear magnetic resonance. *Nature*, 242:190–191, 1973.
- [46] James L. Lear. Principles of single and multiple radionuclide autoradiography. In Phelps et al. [64], chapter 5, pages 197–235.
 - [47] K.L. Leenders, D. Perani, A.A. Lammertsma, J.D. Heather, P. Buckingham, M.J.R. Healy, J.M. Gibbs, R.J.S. Wise, J. Hatazawa, S. Herold, R.P. Beaney,

- D.J. Brooks, T. Spinks, C. Rhodes, R.S.J. Frackowiak, and T. Jones. Cerebral blood flow, blood volume and oxygen utilization: Normal values and effect of age. *Brain*, 113:27–47, 1990.
- [48] Guoying Liu, Geoffrey Sobering, Alan W. Olson, Peter van Gelderen, and Chrit T.W. Moonen. Fast echo-shifted gradient-recalled MRI: Combining a short repetition time with variable T₂* weighting. *Magnetic Resonance in Medicine*, 30:68–75, 1993.
- [49] David MacDonald. Display: Program for Display and Segmentation of Surfaces and Volumes.
- [50] S. Meiboom and D. Gill. Modified spin-echo method for measuring nuclear relaxation times. *Review of Scientific Instruments*, 29(8):688-691, 1958.
- [51] Ravi S. Menon, Seiji Ogawa, Xiaoping Hu, John P. Strupp, Peter Anderson, and Kâmil Uğurbil. Bold based functional MRI at 4 Tesla includes a capillary bed contribution: Echo-planar imaging correlates with previous optical imaging using intrinsic signals. *Magnetic Resonance in Medicine*, 33:453–459, 1995.
- [52] Ravi S. Menon, Seiji Ogawa, David W. Tank, and Kâmil Uğurbil. 4 Tesla gradient recalled echo characteristics of photic stimulation-induced signal changes in the human primary visual cortex. *Magnetic Resonance in Medicine*, 30:380–386, 1993.
- [53] R.S. Menon, X. Hu, G. Adriany, P. Andersen, S. Ogawa, and K. Ugurbil. Comparison of spin-echo EPI, asymmetric spin-echo EPI and conventional

- EPI applied to functional neuroimaging: The effect of flow crushing gradients on the bold signal. In *Proc. SMRM*, 13th Annual Meeting, San Francisco [1], page 622.
- [54] K.D. Merboldt, G. Krüger, W. Hänicke, and J. Frahm. FLASH MRI of human brain activation using a CINE technique. An approach towards high temporal and spatial resolution. In *Proc. SMRM*, 13th Annual Meeting, San Francisco [1], page 432.
- [55] Craig H. Meyer, Bob S. Hu, Dwight G. Nishimura, and Albert Macovski. Fast spiral coronary artery imaging. Magnetic Resonance in Medicine, 28:202–213, 1992.
- [56] Chrit T.W. Moonen, Guoying Liu, Peter van Gelderen, and Geoffrey Sobering. A fast gradient-recalled MRI technique with increased sensitivity to dynamic susceptibility effects. *Magnetic Resonance in Medicine*, 26:184–189, 1992.
- [57] Peter Neelin. MINC User Guide.
- [58] Dwight G. Nishimura. Introduction to Magnetic Resonance Imaging. Stanford University, 1992.
- [59] S. Ogawa, T.M. Lee, A.R. Kay, and D.W. Tank. Brain magnetic resonance imaging with contrast dependent on blood oxygenation. *Proc. Natl. Acad.* Sci. USA, 87:9868–9872, December 1990.
- [60] S. Ogawa, R.S. Menon, D.W. Tank, S.-G. Kim, H. Merkle, J.M. Ellerman, and K. Ugurbil. Functional brain mapping by blood oxygenation level-

- dependent contrast magnetic resonance imaging. *Biophys. J.*, 64:803–812, March 1993.
- [61] S. Ogawa, D.W. Tank, R. Menon, J.M. Ellermann, S.-G. Kim, H. Merkle, and K. Ugurbil. Intrinsic signal changes accompanying sensory stimulation: functional brain mapping with magnetic resonance imaging. *Proc. Natl. Acad. Sci. USA*, 89:5951–5955, 1992.
- [62] P.M. Pattany, R. Marino, and J.M. McNally. Velocity and acceleration correction in 2DFT MR imaging. *Magnetic Resonance Imaging*, 4:154–155, 1986.
- [63] Wilder Penfield. Remarks on incomplete hypothesis for the control of cerebral circulation. *Journal of Neurosurgery*, 35:124–127, 1971.
- [64] Michael E. Phelps, John C. Mazziotta, and Heinrich R. Schelbert, editors.

 Positron Emission Tomography and Autoradiography: Principles and Applications for the Brain and Heart. Raven Press, New York, 1986.
- [65] G. Bruce Pike, Bob S. Hu, Gary H. Glover, and Dieter R. Enzmann. Magnetization transfer time-of-flight magnetic resonance angiography. *Magnetic Resonance in Medicine*, 25:372–379, 1992.
- [66] E. James Potchen, E. Mark Haacke, James E. Siebert, and Alexander Gottschalk. Magnetic Resonance Angiography: Concepts and Applications. Mosby, St. Louis, 1993.

- [67] William H. Press, Saul A. Teukolsky, William T. Vetterling, and Brian P. Flannery. *Numerical Recipes in C: The Art of Scientific Computing*. Cambridge University Press, New York, 2 edition, 1992.
- [68] Marcus E. Raichle. Visualizing the mind. *Scientific American*, pages 58–64, April 1994.
- [69] Bruce R. Rosen, John W. Belliveau, James M. Vevea, and Thomas J. Brady. Perfusion imaging with NMR contrast agents. *Magnetic Resonance in Medicine*, 14:249–265, 1990.
- [70] M.I. Sereno, A.M. Dale, J.B. Reppas, K.K. Kwong, J.W. Belliveau, T.J. Brady, B.R. Rosen, and R.B.H. Tootell. Borders of multiple visual areas in humans revealed by functional magnetic resonance imaging. *Science*, 268:889–893, May 1995.
- [71] Louis Sokoloff. Cerebral circulation, energy metabolism, and protein synthesis: General characteristics and principles of measurement. In Phelps et al. [64], chapter 1, pages 1–71.
- [72] L.S. Stables, R.P. Kennan, and J.C. Gore. Controlling size selectivity in functional echo-planar imaging. In *Proc. SMR*, *Third Scientific Meeting and Exhibition* [2], page 243.
- [73] Keith R. Thulborn, John C. Waterton, Paul M. Matthews, and George K. Radda. Oxygenation dependence of the transverse relaxation time of water protons in whole blood at high field. *Biochimica et Biophysica Acta*, 714:265–270, 1982.

- [74] P. van der Meulen, J.P. Groen, A.M.C. Tinus, and G. Bruntink. Fast field echo imaging: an overview and contrast calculations. *Magnetic Resonance Imaging*, 6:355–368, 1988.
- [75] Jan Willem C. van der Veen, Jan A. den Hollander, and Gerald M. Pohost. Human brain activation: perfusion or bold effects? In *Proc. SMRM*, 13th Annual Meeting, San Francisco [1], page 623.
- [76] Mary P. Wiedeman. An Introduction to microcirculation. Academic Press, New York, 1981.
- [77] K.J. Worsley, A.C. Evans, S. Marrett, and P. Neelin. A three dimensional statistical analysis for rCBF activation studies in human brain. *Journal of Cerebral Blood Flow and Metabolism*, 12:900–918, 1992.
- [78] Graham A. Wright, Bob S. Hu, and Albert Macovski. Estimating oxygen saturation of blood in vivo with MR imaging at 1.5 T. *Journal of Magnetic Resonance Imaging*, 1:275–283, 1991.
- [79] Yasuji Yoshida and Fusahiro Ikuta. Three-dimensional architecture of cerebral microvessels with a scanning electron microscope: A cerebrovascular casting method for fetal and adult rats. *Journal of Cerebral Blood Flow and Metabolism*, 4:290–296, 1984.
- [80] Y. Zur, M.L. Wood, and L.J. Neuringer. Spoiling of transverse magnetization in steady-state sequences. *Magnetic Resonance in Medicine*, 21:251–263, 1991.